Visualizing real time vasomotion *in vivo* using Optical Coherence Tomography

Suhir Abuhajar

2012

Lancaster University-Physics Department-Nonlinear Biomedical Physics

Submitted in fulfilment of the requirements for the degree of Doctor of Philosophy in Physics

ProQuest LLC.
789 East Eisenhower Parkway
P.O. Box 1346
Ann Arbor, MI 48106 – 1346

Contents

Declaration

I declare that this thesis is my own original work, under the guidance of Professor. Aneta Stefanovska, and Dr Oleg Kolosov and it has not been submitted in substantially the same form for the award of a higher degree at any other university. Nor does it contain, to the best part of my knowledge, any material published or written by another person, except as acknowledged in the text.

Abstract

As blood vessel imaging techniques facilitate the fundamental understanding in vascular performance diagnosis and biomedical research improvement, we aimed to visualize and understand the blood vessels dynamics under human skin and their underlying mechanisms in real time. In this study, a noninvasive imaging system was selected to provide an investigation of the real time oscillation of blood vessels *in vivo*, using Spectral Radar Optical Coherence Tomography (SROCT). This main goal was achieved by evaluating the precision and confidence in recorded data by using a phantom made of Intralipid (IL) to mimic the physical properties of the skin. Then, we successfully managed to visualize for the first time the vasomotion under human skin using MatLab Image Processing Toolbox. After that, we explored mathematically the cyclic variations of the vascular area obtained from the images for a cohort of six participants. The Fourier and wavelet transforms were applied to identify the characteristic frequencies related to the oscillations in vascular cross sectional area. Finally, we investigated dynamical aspects of vasomotion, in response to temperature change, by using a Melcor Thermoelectric Temperature Controller (MTTC) to produce local heating in conjunction with Spectral Radar Optical Coherence Tomography (SROCT).

Acknowledgment

I would like to express my gratitude to all those who gave me the possibility to complete this thesis. I would like to express my sincere gratitude to my advisors Professor Aneta Stefanovska and Dr Oleg Kolosov, for the valuable advice, motivation, enthusiasm, and immense knowledge throughout my studies. Thanks go to Dr Bob Jones for improving the English in my dissertation and for all his useful comments and suggestions. Thanks to Phil Clemson and Gemma Lancaster for the final corrections as well. I am truly indebted and thankful to Professor Peter McClintock for his encouragement and guidance.

A huge thank you to the Libyan government for giving me an opportunity to study abroad and to provide me with financial support.

It is a pleasure to thank laboratory assistance at Physics Department who made this research possible by providing all kind of assistance and help, especially to Peter Livesley and Stephen Holt. Thanks to Matt Butcher from Thorlabs company for his useful instructions during the first stages of setting up the Optical Coherence Tomography.

I am obliged to many of my colleagues in the Nonlinear Biomedical Physics Group; although, I did not work with most of them directly, but just for making me enjoy the place of work and for giving me the opportunity to know people from different world: Anthony Hinds, Tom Hansard, David Kenwright, Spase Petkoski, Rodrigue Tindjong, Lawrence Sheppard, Norman Turner, Andrea Duggento, Alison Hale, and Dmytro Iatsenko. I am in particular grateful to Alan Bernjak for providing the code for calculation of wavelet transform developed over many years

by the members of the group, to Adam Bradbury for useful discussions about its implementation and to Tomislav Stankovski for his help in creating movies using MatLab Images Proceeding toolbox.

This dissertation would not have been possible unless several volunteers contributed to the study by freely giving their time to be measured. They all deserve my great thanks and gratitude.

A deepest thank you goes out to my dearest ones, my beloved husband, and my lovely kids (Nagmeddin, Noor, Naba) for love, support, patience and understanding during these years.

Finally I owe sincere and earnest thankfulness to my parents for their gift of life, love and unwavering support, without which none of this work would have been possible.

Suhir Abuhajar

List of Figures

List of Tables

Chapter 1

Introduction

1.1 Motivation

Studying biomedical applications of advanced technologies has attracted active research in recent decades. Imaging techniques facilitate the fundamental understanding of disease by medical professionals and allow ongoing developments and improvements in biomedical research. In particular, imaging blood vessels under skin and visualization of their functional changes has potential to become a very powerful tool for vascular performance diagnosing and biomedical research. Therefore, the main long term goal of this work was to visualize and to study *in vivo* the oscillations of the diameter of the smallest vessels in real time under human skin.

The initial objective of this work was selecting of a non-invasive imaging method that can provide suitable resolution images with a suitable depth to achieve the main motivation of this work. For this particular goal, Optical Coherence Tomography (OCT) is an instrument that was selected and worked on during this research program. After that, the aim was to evaluate the precision and confidence intervals within which the recording can be made by OCT. This essential objective was made by measurements on a phantom which mimics the proper-

ties of the skin. The next goal was to detect the vessel in the image obtained by OCT and create a sequence of its contours. This included creating a video of blood vessel motion and identification of the changing vessel cross-sectional area as a function of time. In addition, we specifically propose to investigate the vasomotion under human skin by plotting the changing area of the vessel as a function of time and then analyze mathematically the time series of the data collection by using Fourier transform and wavelet transform function. Finally, the last objective of this work was to study the influence of external heat applied locally to the human skin and identify changes in vascular diameter using OCT. The achievement of this goal is very important for advancing biomedical research, the selection of the most appropriate treatment, early detection of some diseases related to the vascular function and thus improving the clinical outcome.

1.2 Structure of the thesis

This thesis will explore the implications of the real time oscillation of blood vessels under human skin in-vivo by using Optical Coherence Tomography (OCT) imaging. We will start by considering the physiology of human skin and presenting an overview of the human skin functions and structures, then we will highlight a brief information on the vasomotion under skin. Furthermore, we will study some of the skin optical properties in order to understand the effect of light used in an imaging procedure to the human skin where this light was applied. At the end of the first chapter, we will present some of the current imaging techniques of blood vessels and make a brief comparison between several of them to figure out the advantage of Optical Coherence Tomography (OCT) which led us to pick it among the others.

I will then go on in the next chapter to introduce OCT and outline its main characteristic and some of its applications, and then move on to the principles of

operation of the system. Moreover, I will rough out the different versions of OCT and make a brief comparison of these versions. Then, I will describe the experimental set-up of the Spectral Radar Optical Coherence Tomography (SROCT) which has been used in our research. Finally, by the end of this chapter, I will summarize generally the theory of OCT and then move on to focus on the theory of SROCT and then summarize the Optical Detecting Sensitivity of OCT which is very important for analyzing the collected data.

In the third chapter, I will introduce the phantom which mimics human skin and explain the experimental results which were obtained from the phantom to evaluate the precision of the instrument and the way of measurement. First, I will start by making a description of our phantom components and the experimental set-up. Then I will move on to show some of my results by phantom as following:

1. Several phantom images with different layers which simulate vessels.
2. Evaluating the accuracy of the selected system by presenting and discussing results of measurements on several subjects.
3. Studying changes of the intensity with depth.
4. Finding out the depth correction factor of the intensity for defined images.
5. Detecting a contour around artificial vessel and then calculating the area of the contour.
6. Investigation of the instrumental noise level in long time series.
7. Reconstructing the three-dimensional images of the phantom.

In the final section of this chapter, I will summarize the conclusions based on all the results from imaging human skin vessels *in vivo* as well as using the phantom.

In chapter 4, I will start by introducing briefly the experimental set-up for measurements on human skin. Then, I will move on to apply previously elaborated

experimental steps with the phantom on measurement of human skin and the results will be presented in this chapter as coming:

1. Several human skin images will be presented to show the vessels of different size recorded at different depths non-invasively and *in vivo*.
2. Studying the changing intensity with depth for human skin images
3. Calculating the correction factor of intensity and comparing the results with those obtained from the phantom.
4. Plotting several images in a sequence to visualize the changing of the vessels with time.
5. Displaying several plotted contours of vessels taken over time to illustrate oscillation of cross section area.
6. Analyzing the vasomotion under human skin by studying the changing area of the contour with time.
7. Examining the time series obtained from the imaged cross sectional area of selected vessels to investigate the frequency of vasomotion using Fourier and wavelet transforms.
8. Detecting the instrumental noise level from the real vessel oscillations by using Fourier and wavelet transform.
9. Reforming the three-dimensional images of human skin to investigate the blood vessels layers under skin.

In the final section, I will conclude this chapter by outlining all the results that were obtained from human skin.

In chapter 5, the effect of heating on blood vessels oscillation will be presented. By applying an external heating system on human skin for a period of time , I

will examine how the dynamics of blood vessels changes following local skin heating. Subsequently, I will carefully analyze the data collected relying on previously researched steps in this point to figure out the effective action of the vessel oscillation and the remodeling of frequencies components by using wavelet analysis. Then, I will close this chapter by providing conclusions and remarks about this external effect on human vasomotion.

In the last chapter, the main obtained results and achievements of this work will be summarized and the overall conclusions will be drawn. In addition, several possible improvements and suggestions will be discussed for any further work in this field.

1.3 Physiology of the skin

The cardiovascular system is one of the most important systems in the body. It serves to provide rapid transport of nutrients around the body and rapid removal of waste products. It is made from heart, lungs and blood vessels. Blood vessels play a vital role in cardiovascular system by networking all the organs and tissues in the human body. The total length of the blood vessels in the circulatory system is about 97,000 kilometers for a child and could reach 161,000 kilometers long for an adult. This length would circle the earth four times if the blood vessels of an adult were lined up end to end [1]. Moreover, the typical diameter of these vessels varies between 5 and 10 μm for the smallest capillaries [2] and 2 to 3 cm for the biggest arteries [3]. These blood vessels have the ability to expand and contract to help control the flow of blood. There are several types of blood vessels which are [4],[5]:

- **The arteries** are elastic muscular tubes that carry the blood with nutrients from the left ventricle of the heart to all organs and human tissues. They diverge to smaller and smaller vessels as they move away from the heart.

They are named arterioles, until they eventually terminate in capillaries.

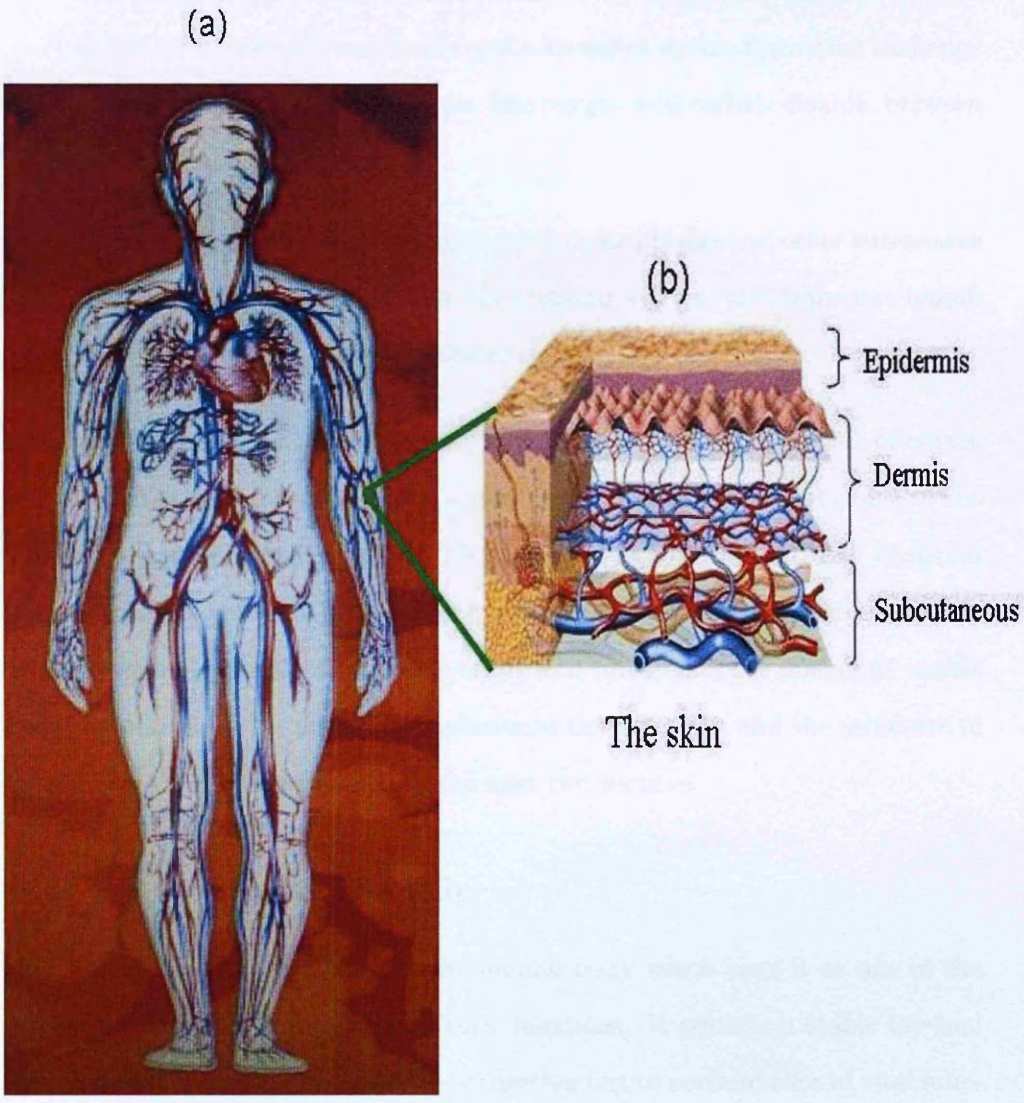

Figure 1.1: (a) A schematic diagram of human circulatory system [6], (b) the diagram of the blood vessel distribution under human skin [7]

- **The veins** merge and converge into successively larger blood vessels as they move towards the heart and the venules are the smallest veins which connect with the capillaries to carry exchanged blood and return it to the heart.

- **The capillaries** are the smallest and most important working unit in the blood vessels that connect the arterioles to the venules. There are about 40,000 to 100,000 kilometers of capillaries which enable the actual exchange of nutrients and other substances, like oxygen and carbon dioxide, between the blood and the tissues.

- **The lymphatic vessels** act as a reservoir for plasma and other substances including cells that leaked from the vascular system, and transport lymph fluid back from the tissues to the circulatory system.

Mainly, there are about 3 meters of blood vessels, around 11 kilometers of nerves and about 1300 nerve ending in one square centimeter of the largest organ of the human body which is the skin [8]. These vessels supply the skin that wraps all the human body with nutrients and oxygen to help it regularly do all its functions to maintain good health. In order to study and investigate the images of vessels under human skin, one must first understand the functions and the structure of the skin which will be explained in the next two sections.

1.3.1 Functions of the skin

Skin has an essential function for the human body which puts it as one of the top organs as to the importance of their functions. It permits a stable internal environment, not just holding the body together but to perform a lot of vital functions. The following are some of the important functions that skin can perform [9],[10]:

1. **Communication and sensation:** Skin plays a vital role of communication between our body and outside environment. As skin contains a variety of nerve endings, it provides a great deal of information by the sense of touch which helps knowing more about outside environment through recognizing heat, cold, pressure, pain, tissue injury, and emotional sensations. In addition, it helps to feel vibration, and any

intense sensation of itching. Under physical state, skin gives aesthetic appearance, sexual attraction, and low level of bacterial decomposition. Finally, by emotional state, it provides facial expressions, goose bumps and color.

2. **Protection:** Skin protects internal organs from environmental dangers. By immunological function, skin protects the body against microbial attack or any kind of infections. Moreover, it saves the body against allergic reaction. Skin is a defence part for human body from mechanical damage, bacteria, fungi and virus; also, protecting from excessive radiation.

3. **Temperature regulation:** As the core body temperature needs to be maintained for normal physiological activities, skin is the main controller to regulate the thermodynamics of the human system by giving off heat in hot weather or conserving heat in cold weather. Even under extreme conditions of high temperature and exercise, skin keeps body temperature normal.

4. **Maintaining fluid balance:** The skin provides a relatively dry and semi-impermeable barrier to fluid loss by controlling evaporation. In addition, it permeates an excess water by absorbing it from adherent keratinocytes and sebum. Also, skin excretes to maintain fluid balance by disposing of waste products and salt in sweat.

5. **Metabolic function:** Skin acts as a means of synthesis of vitamin D by action of Ultraviolet (UV) radiation on certain parts of the skin. Furthermore, it gives structure to proteins, glycan, lipids, signalling molecules. Moreover, it provides a storage of several substances such as: electrolytes, water, vitamins, carbohydrates, and protein. In addition, skin plays an important role for wound healing by secreting fibronectin and other components required for restoration.

6. **Water resistance:** Skin mainly acts as a resistant barrier impermeable to water so the important nutrients are not washed out of the body.

7. **Excretion:** Skin excretes waste products and excess salt from the body by insensible sweating; also, more pronounced water loss through sweating occurs as temperature regulation function.

8. **Medicine transportation:** Skin is one of the most important sites of medicine transportation among many human body organs. Medicine can be administered through the skin by ointments or by means of adhesive patch or by iontophoresis.

1.3.2 Structure of human skin

The skin is a complex tissue system which covers all human body and comprises about one sixth of total body weight with approximate area between 1.5 - 2 square meters [11]. It is built up from several thin sheets of layers, stacked cells in which there are nerves, blood vessels, hair follicles, glands, and sensory receptors. The skin is supplied with nutrients and oxygen via the blood vessel system to help regulate all skin functions and support blood pressure regulation. There are three vital skin layers of human body and each of them has one or more essential functions [12], [13]:

Epidermis is the first outer layers of human skin which is nearly free from the blood vessels and is formed from several sheets where cells are formed through mitosis at the innermost layers. The main skin cells that make up the epidermis are called the keratinocytes, and these cells produce a tough protein called keratin which forms nails and hairs; Also, it makes skin waterproof. Generally, the epidermis is nourished by the diffusion from blood capillaries that extend to the upper layers of the dermis. The thickness of this layer varies from one part of the body to another at the same person; also, it is different from one human to another dependent on

age, the type of human job and where this human lives in the world and the range of this thickness is between 0.12 mm to around 0.17 mm over most surfaces of the body, but may reach a thickness of 0.8 mm on the palms of the hands and up to 1.4 mm on the soles of the feet. This layer of the skin has the main function to serve as a barrier to protect the body from environmental dangers and provides mechanical resistance.

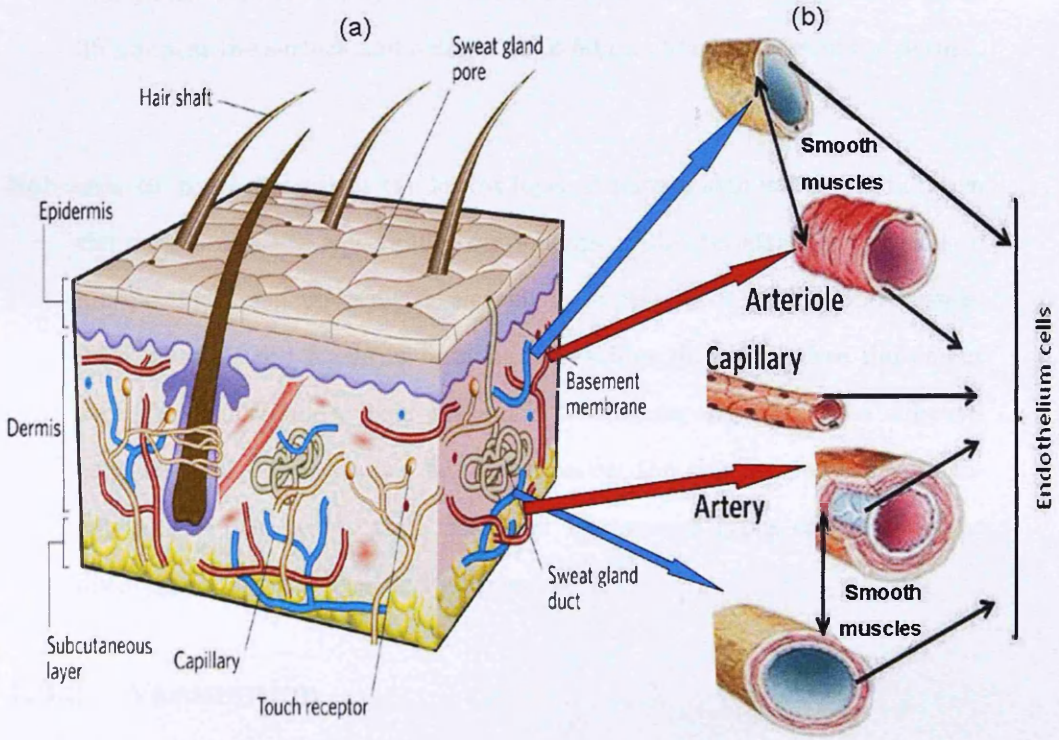

Figure 1.2: (a) The diagram of human skin structure [14] and (b) the structure of the blood vessels [15]

Dermis is the second layer of the skin which is tightly connected to the epidermis by a basement membrane and it is a thick layer which varies from 0.1 mm to 1 mm. It contains the hair follicles, sweat glands, sebaceous glands, apocrine glands, lymphatic vessels and blood vessels which provide nourishment and waste removal to dermis and to epidermis as well. The upper part of

the dermis is the papillary layer, which contains the micro-vessels supplying the epidermis. In addition, the sheets of dermis give the skin its strength, and maintain its elasticity also they supply nutrients to the different layers of the skin. It harbors many nerve endings that provide a sensation to the body. In fact, normal people's epidermis and dermis usually do not exceed $1-2$ mm in depth together and their depths vary depending on each specific position in the body. The diameter of blood vessels is between 10 to 35 μm near the surface and reaches 40 to 50μm at the bottom of the dermis.

Subcutis or hypodermis is the lowest layer of human skin which lies between the dermis and the soft tissue components. Subcutis attaches the skin to muscle and bone underneath as well as supplying it with blood vessels. This layer is very essential because it provides the skin a free movement over the underlying muscle without a tension on the skin. The subcutis contains half of the body's fat which serves the skin as padding and insulation for the body; also, this layer has several types of cells such as fibroblasts, macrophages and adipocytes.

1.3.3 Vasomotion

Vasomotion is spontaneous rhythmic variation in vessel diameter responsible for microcirculatory blood flow oscillation into an organ [16], [17]. It consists of cyclic diameter variations of muscular arteries or arterioles that are not a consequence of heart beat, respiration, or neuronal input, but result from substances oscillation in the vessel [18]. This oscillation consists of rhythmic oscillations in micro-vessel diameter and is responsible for local changes in contraction and relaxation of smooth muscle cells which are present in muscular vessel walls [19]. The functional and structural characteristics of the blood vessels change with successive branching. However, there is one structural component in common in the entire cardiovascular system. This is a smooth single-celled layer of en-

dothelial cells or endothelium, which lines the inner surface of the vessels [21]. All other vessels have additional layers of connective tissue and smooth muscle except capillaries does not consist these layers. The figure (1.3) presents the structure and the functions of the two main components in the entire blood vessels which have an essential role for controlling the vasomotion. These two elements are the endothelial cells and vascular smooth muscle [22]:

- **endothelial cells or endothelium:** The endothelium is the thin layer of cells that are in close contact with each other and lie in the inner walls of blood vessels, which form the interface between the blood and the vessel wall. The vascular endothelium constitutes approximately 1% of body mass and has surface area of approximately 5000 m^2. A single layer of endothelial cells (ECs) consisting of 1 to 6 $\times$ 10^{13} cells, covers an area of approximately 1 - 7 m^2 [23]. These cells play a vital role in the mechanics of blood flow, the regulation of coagulation, and vascular smooth muscle cell growth, and they also serve as a barrier to the vascular diffusion of liquids and solutes. They are unique multi-functional cells with critical basal and inducible metabolic and synthetic functions. The endothelial cell reacts with physical and chemical stimuli within the circulation and regulates hemostasis, vasomotion tone, and immune and inflammatory responses [24]. It forms an interface between circulating blood or lymph in the lumen and the rest of the vessel wall. Also, it assists the calcium (Ca^{+2}) release from intracellular stores synchronized by a calcium-dependent chloride current to account for vasomotion in arterioles. Furthermore, it produces an important nitric oxide (NO) factor which causes a relaxation of vascular smooth muscle. This factor was originally named endothelium-derived relaxing factor (EDRF) and it is released continuously by endothelium in the arterioles and contributes to arteriolar vasodilation in the basal state. Also, it releases other vasodilatory factors such as prostacyclin (PGI2) and vasoconstrictors such as endothelin-1 (ET-1) [25].

- **Vascular smooth muscle:** Vascular smooth muscle is the particular kind of smooth muscle which are found within and compose the majority of the wall of large blood vessels. Vascular smooth muscle plays a vital role of a mechanism that is responsible for the redistribution of the blood within the body to areas where it is needed by contracting or relaxing. By this performance, they provide adequate oxygenation to tissues and remove waste. Moreover, they alter the luminal diameter, which enables blood vessels to maintain an appropriate blood pressure and provide adequate oxygenation to tissues.

  Vascular smooth muscle cells are the stromal cells of the vascular wall, which are arranged as circular layers around the larger vessels and in a single layer around arterioles. They provide active tension in the vessel wall and regulate the diameter of the vessels. In many vessels, they act as pacemakers and excite neighboring cells, thus providing background tension and the myogenic basal tone. In addition, they are continually exposed to mechanical signals and biochemical components generated in the blood compartment. Moreover, they are involved in all the physiological functions and the pathological changes taking place in the vascular wall. In fact, the property of this muscle is similar to that of the heart, but the contractile characteristics and the mechanisms that cause contraction of vascular smooth muscle are very different from those for cardiac muscle. Vascular smooth cells undergo slow, sustained, tonic contractions, whereas cardiac muscle contractions are rapid and of relatively short duration (a few hundred milliseconds). Contraction in vascular smooth cells can be initiated by mechanical, electrical, or chemical stimuli. Passive stretching of vascular smooth muscle can cause contraction that originates from the smooth muscle itself and is therefore termed a myogenic response. Electrical depolarization of the vascular muscle cell membrane also elicits contraction,

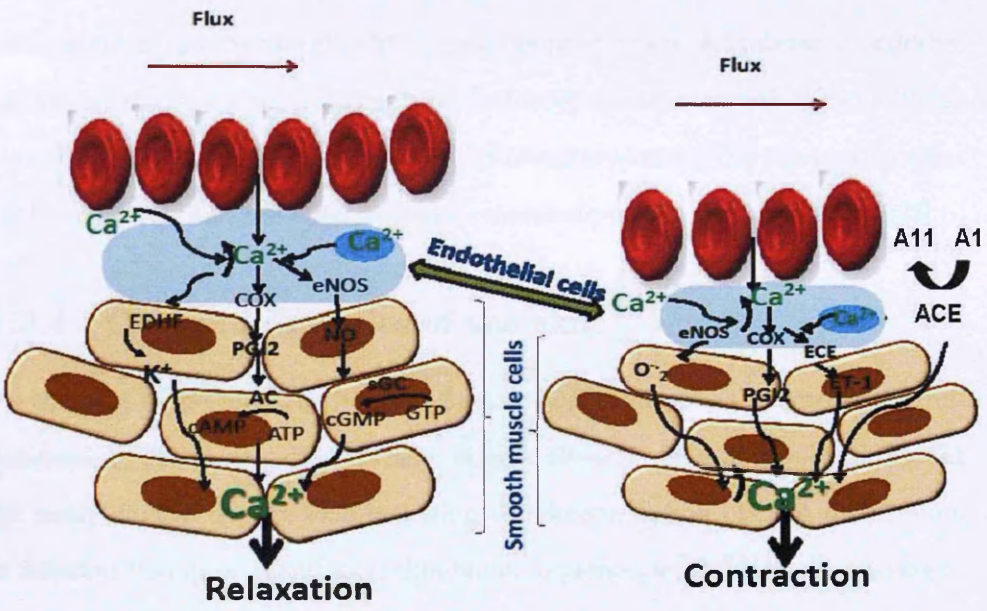

Figure 1.3: Release of relaxing and contracting factors from endothelial cells and their effects on vascular smooth muscles. The essential endothelial-derived substances are: AC = adenylyl cyclase; ACE = angiotensin converting enzyme; ATP = adenosine triphosphate; A1 = angiotensin I; A11 =angiotensin II; cAMP = cyclic adenosine monophosphate; cGMP = cyclic guanosine monophosphate; COX =cyclo-oxygenase; ECE = endothelin converting enzyme; EDHE = endothelium-derived hyperpolarising factor; eNOS = endothelial nitric oxide synthase; ET-1 = endothelin-1; GTP = guanosine triphosphate; NO= nitric oxide;O = superoxide anions; PGI2 = prostacyclin; sGC = soluble guanylyl cyclase

most likely by opening voltage dependent calcium channels and causing an increase in the intracellular concentration of calcium. Finally, a number of chemical stimuli such as norepinephrine, angiotensin II, vasopressin, can cause contraction of vascular smooth muscle cells. Each of these substances bind to specific receptors on the vascular smooth muscle cell or to receptors on the endothelium, which then leads to contraction [26].

As shown in the figure (1.3), various blood borne substances that come in contact with vascular endothelial cells (EC) cause the production and release of endothelial factors that elicit contraction or relaxation of vascular smooth muscle. These endothelial factors modulate the effects of norepinephrine (NE) released by sympathetic nerves, and the effects of tissue metabolites and humoral factors [27].

1.3.4 Optical properties of the skin

As the skin is the interface between human body and optical environment, understanding the propagation of light in skin tissue is fundamentally important for many clinical applications including the determination of light distribution in different therapies; monitoring skin blood oxygenation, melanin concentration, and water concentration; and improving noninvasive optical measurements of tissue. The randomly inhomogeneous distribution of blood, collagen and various chromophores and pigments in skin produce variations of the average optical properties of the skin layers. The inherent optical properties of the skin layers are determined as the manner in which the skin reflects and transmits light of different colors, or wavelengths [28]. Each of these layers has different inherent optical properties, primarily due to differences in the concentration of melanin, blood, collagen and keratin between them [29]. The inherent optical properties of a particular layer can be represented by a set of non-dimensional numbers: the optical depth, the single scattering albedo and the normalized volume scattering function which all depend on wavelength [30]. Therefore, the skin can be described as an optically inhomogeneous material which interacts with light producing a reflection, scattering and absorption that may affect the nature of these interactions [31].

- **Reflection of skin**

  The reflection property of human skin depends on the structure of its components. The reflective behavior of the skin layers is represented usually as a function of the wavelength of the source at each layer. As the upper-

most level skin is covered with dead cells, the surface of the skin can be approximated to a surface with no regular reflection. The regular refractive index of other layers is approximated from a mixture of the reflective index of water and protein. As the protein has a reflective index value over the wavelength range between 600 nm to 2000 nm, The reflection index can be calculated from this equation [32]:

$$n_{skin} = 0.7(A - B\lambda + C\lambda^2 - D\lambda^3 + E\lambda^4 - F\lambda^5) + 0.3 \times 1.5, \qquad (1.1)$$

where 1.5 is the refractive index value of the protein, λ is the wavelength in nanometers, values A to F were obtained by fitting value of reflective index for water to a 5^{th} order polynomial as follow, A=1.58, B=8.45×10^{-4} nm^{-1}, C=1.10×10^{-6} nm^{-2},
D=7.19×10^{-10} nm^{-3}, E=2.32×10^{-13} nm^{-4}, F=2.98×10^{-17} nm^{-5}.

- **Absorbers in skin**

  Skin has three primary absorbers of the light contents which are blood, melanin, and keratin. Since the blood vessels and capillaries are found only below the epidermis, the blood absorption of the light is very low near the surface of the skin. Furthermore, the melanin concentration affects the skin reflectance strongly at all wavelengths and its absorbance depends on the relative difference between the optical properties of melanin and its surroundings. Moreover, keratin has significant absorption and scattering properties to the light depending on the range of the wavelength of the source. Generally, the main absorption of photons by blood is at wavelengths smaller than 600 nm; otherwise, it is very low and this wavelength reliance of the absorption is the main cause of the red color of blood. Over all, there is large variability of the regular epidermal absorbers, both with respects to amount and distribution. This variability also happens because of dynamic feedback mechanisms, such as: thickening of the keratin-rich

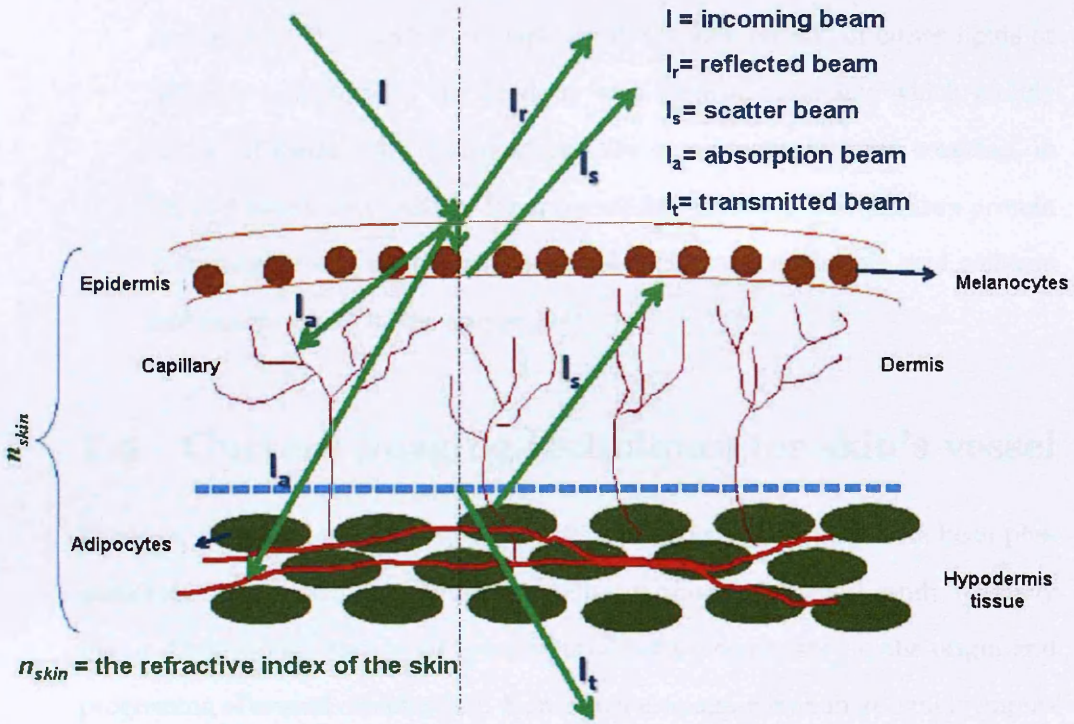

Figure 1.4: A sketch of human skin and the optical properties of the skin layers, where I, I_r,I_a, I_s and I_t are an incoming , a reflected, an absorbtion , a scattering and a transmitted beams into the skin.

stratum corneum, and increase of blood content below the epidermis. [33].

- **Scatterer in skin**

  Skin without blood and melanin appears diffusely white due to the inhomogeneous distribution of micro and nano-scopic particles and fibers with variable refractive index in the skin. A photon entering the skin will be scattered around by these particles as the ball by the pins in a pinball machine and can, therefore, be reflected from the skin in any direction with

almost equal probability. This multiple scattering gives the skin its diffuse appearance. The scattering particles in the skin consist of either lipids or proteins embedded in the fluids in and between skin cells which mainly consist of water. The lipid scatterers are found in the stratum corneum, in the cell membranes, and in the intracellular particles. The primary protein scatterers in skin are keratins and melanins in the epidermis, and collagen and elastin fibers in the dermis [34].

1.4 Current imaging techniques for skin's vessel

In recent decades, technological advances in imaging of the body have been phenomenal. Microcirculatory imaging facilitates the fundamental study of many major diseases and may provide a potential early perspective on the origin and progression of several diseases [35]. Non-invasive imaging is an increasingly important modality in vascular performance diagnosing, being a valuable and powerful tool for medical personnel and research development. However, existing techniques generally require invasive procedures or exogenous contrast agents, which perturb the intrinsic physiology of the microcirculation. Therefore, we report here on several general techniques of imaging which are available for imaging the vessels and then compare generally between them to select the technique suitable to achieve the main motivation in this research. There are several general techniques of imaging that can be mentioned; however, we will focus only on the techniques which are used for imaging vessels.

- **X-rays**

  X-ray photographic imaging is a technique of major importance in medical diagnosis. Any investigation by this technique relies on assessing approximately radiographs from different angles or by screening the subject as the X-ray moves around them [36]. This technique is used to visualize the vessels on human skin and to generate an image of the cardiovascular system,

including the arteries and veins and to determine if there is any damage or blockage of the vessel by injecting an iodinated contrast material into the blood vessels and then focusing on X-rays imaging within this area. However, X-ray imaging has limitations because it does not provide any clue to depth from a single image; or to the shape, site, and size. In addition, it provides resolution around sub millimeters which makes the imaging of micrometer sized vessels not clear enough to identify them. Furthermore, it has a health risk as it increases the risk of developmental problems and cancer in those exposed [37].

- **Computed Tomography (CT Scan)**

  Computed tomography (CT Scan) is one of the greatest advances in imaging techniques which help in detecting any human problem without resorting to exploratory surgery. CT is worked by surrounding the body with multiple detectors to record the strength of the exiting X-rays. This technique allows precise localization of lesions such as blood clots or tumors and other abnormalities in almost any part of the body at sub-millimeters depth resolution and for few seconds. Three dimensional reconstructed images can be created to demonstrate specific organs by using complicated software. The advanced technique of CT has more recently become useful for cardiac imaging, identification of coronary artery calcification and providing greatly improved anatomical definition of organs and blood vessels [38]. However, it has nearly the same disadvantages as X-rays imaging for our aim.

- **Magnetic resonance imaging (MRI scan)**

  MRI provides a hazard-free, non-invasive way of generating images by applying harmless radio waves to the patient after placing within a magnetic coil. The protons which are excited form the nuclei of hydrogen and give off measurable electric energy which with the aid of computation create an image [39]. MRI is the most expensive technique, which gives outstanding definition especially in the brain and the skeletal system, as well as most

other organs, tissues and blood vessels, and provides several millimeters resolution in depth and takes several minutes to obtain the image. Moreover, MRI does not use ionizing radiation and in certain cases can provide information as a functional imaging on any part; but the imaged body should be injected with some substances [40]. Also, as in CT, three-dimensional reconstructed images can be created to demonstrate specific organs. However, it is an expensive research tool; is not easy to use and requires experienced operators; at the present time it has limited prognostic value at least in terms of the microcirculation.

- **Ultrasound scans (Ultrasonography)**

  Many pioneers worldwide contributed to this new technology, the growth of its medical applications, and its involvement with manufacturers, leading to its present sophistication. Ultrasound scanning is quick, relatively inexpensive, and non-ionizing, with no known biological hazard when used within the diagnostic range of frequency. Therefore, it is a prime diagnostic method in obstetrics, monitoring pregnancy, imaging fetal development, and the newborn brain. Photoacoustic Imaging is one of the applications of Ultrasound scanning, which delivers non-ionizing light into biological tissues and can provide a sub-millimeter high resolution in real time images with suitable depth [41]. However, this sub-millimeter resolution makes it difficult to visualize small vessels near the human skin surface which we propose to investigate in this research.

- **Optical techniques**

  In functional imaging, optical imaging is highly desirable because of the strong correlation between optical absorption and hemoglobin concentration and/or oxygenation [42]. The choice of optical method with a near infra red (IR) broadband source is ideal for most biological samples due to the low scattering losses associated with IR radiation. Confocal microscopy and two-photon microscopy, are noninvasive but possess a limited

depth sectioning capability due to the strong optical scattering in biological tissues, which makes them have a difficulty in detecting microvessels without exogenous fluorescent agents, which, are still facing challenges in clinical applications [43], [44]. In addition, Orthogonal Polarization Spectral (OPS) imaging is another optical technique which permits noninvasive microvascular imaging without the use of fluorescent dyes, paving its way to the bedside. However, OPS provides no depth information and lacks the measurement consistency required for longitudinal studies [45]. Optical Coherence Tomography (OCT) is another optical imaging technique which provides suitable resolution images in real time for small vessels that lies under human skin, which leads the main motivation of this research to be achieved.

In particular, Optical Coherence Tomography (OCT) is a non-invasive imaging which has become a prominent biomedical tissue-imaging technique which is used for ophthalmic applications and other tissue imaging requiring micrometer resolution and millimeter penetration depth [46]. It is relatively free from operator bias and uses a non-contact device which can be used for continuous measurements. It generates two and three dimensional images which will help in identifying the small vessel layers under skin. However, clinical intervention trials are presently lacking, which are required to confirm its prognostic value; also, as large amounts of data are collected, the computational times can be quite long. In general, the images obtained by OCT depend on the type of sample as well as the design of the system. Therefore, there are several approaches to OCT imaging systems and the selection of a particular system relies on the specific application requirements. For multilayered biological tissue (skin, brain, gastro-intestinal tract, etc.), the 900 to 1400 nm range is appropriate, since longer wavelengths typically provide better penetration depth [47].

Established clinical imaging modalities such as computed tomography (CT), magnetic resonance imaging (MRI) lack the resolution needed for microvascular imaging [48]. Even with iodine contrast, X-ray imaging cannot image single capillaries. Thus, only Optical Coherence Tomography (OCT) allows quantification of vessel count, diameter, length, density, permeability, and microcirculatory function. The fundamental difference between OCT and X-ray and MRI is that OCT can provide non-invasive, non-ionizing diagnostic imaging which is important for our motivation in this thesis. Moreover, Photoacoustic imaging has 2-3 orders of magnitude weaker scattering than optical waves in biological tissues. These properties help Photoacoustic imaging provide more possible depth penetration than OCT does. However, visualizing the oscillation of vessels in real time is not possible due to the slowness of recording the data. In addition, the resolution of the image is within sub-millimeters and is hardly capable of detecting very small vessels and capillaries under human skin [49].

	OCT	X-Ray	CT	MRI	Ultrasound
Resolution	micron	sub mm	sub mm	mm	sub mm
Speed	Real time	Real time	Seconds	Minutes	sub seconds
Cost	Low	Low	Medium	High	Low
Ionizing	No	Yes	Yes	No	No
The view	3D	2D	3D	3D	3D

Table 1.1: A Comparison of modality parameters for several imaging techniques [50]

As the table (1.1) highlighted a comparison of the parameters for several selected imaging techniques in modality, we can notice that Optical Coherence Tomography is the most suitable technique to accommodate our special imaging requirements by providing a non-invasive measurement for small vessel in vivo in

order to achieve the aim of this research for visualizing the blood vessel oscillation under human skin in real time. The specific advantages of OCT compared to alternative optical techniques are depth resolution which is independent of the sample beam aperture. Another advantage of OCT is the coherence gate which can substantially improve the probing depth in scattering. In addition, there are several advantages of OCT over non optical imaging modalities which are a high depth and transverse resolution, freedom of contact and non invasive operation, and function-dependent image contrast. Spectral Radar OCT is one of the OCT techniques which can be applied to a wide range of biological and industrial imaging applications. Cross-sectional and 3D images of samples ranging from the human in vivo to laminated packaging films or mechanical parts can be obtained in real time, making this system ideal for many clinical and industrial applications. The Standard (930nm) spectral radar system yields a typical imaging depth of $\sim$1.6mm and an axial resolution of 6.2μm [51]. Overall, this multi-purpose system provides a balanced optimization of both resolution and measurement depth to visualize the vessels under human skin and to investigate their oscillation.

In simple terms, as non-invasive imaging techniques become the norm for studying many major diseases, some of these current techniques have been generally presented to select the most suitable technique to achieve the motivation of this thesis. The comparison between several imaging techniques was widely made, and it has led to the conclusion that SROCT is the most suitable non-invasive system for visualizing vasomotion under human skin in real time, which guides this work to achieve the main goal of this research.

Chapter 2

Optical Coherence Tomography (OCT)

2.1 Introduction

Optical coherence tomography (OCT) is a fundamentally new type of non-invasive optical imaging modality in biomedical optics and medicine which employs non-ionizing optical radiation. OCT, a low-coherence interferometry technique, is well developed for a high resolution ranging and characterization of optoelectronic components. It performers a cross section tomographic imaging of the internal microstructure in material and biological tissue by measuring backscattered light [52]. It typically employs near-infrared light which can achieve image resolutions between 1- 15 μm, and can achieve several millimeter penetration in depth by attenuation from optical scattering [53]. By now OCT has found its place as a widely accepted imaging technique, especially in ophthalmology, other biomedical applications and art conservation that require micrometer resolution and millimeter penetration depth [54]. It is a powerful imaging technology in medicine because it performs 'Optical Biopsy', in real time and in vivo visualization of tissue microstructure, without the need to remove and process specimens [55].

These new techniques of OCT achieve dramatic advances in imaging speed which enable three dimensional imaging by adding low coherence interferometry lateral scanning to allow depth resolved acquisition from the volume of the biological material. In addition, tissue microstructure can now be visualized and rendered using methods similar to some other techniques, but with micron scale resolution [56].

2.2 Main characteristic of OCT

There are several characteristics of OCT which make it one of most important imaging techniques available these days for medical and research improvement [57]:

1. A non-invasive imaging technique which provides information in real time for *in vivo* samples.

2. The interferometric technique provides high dynamic range and sensitivity more than 100 dB.

3. The high depth resolution is one of the main driving forces behind OCT development.

4. As multiple scattered events lose the phase information, and a strict phase relationship is required between the interfering waves, the maximum penetration depth in OCT is the depth from which single scattered photons still originate which is between 1.5 mm to 2 mm in skin depending on the wavelengths of the source.

5. As the main constituents of the tissue, water, pigments, etc. exhibit low absorption for the infrared light, OCT uses wavelengths within the band 600 nm to 2000 nm [58].

6. The weak signal in the object arm, backscattered or transmitted through the tissue, is amplified by the strong signal in the reference arm due to the

involvement of multiplication of the two optical waves at Photo-detection [59].

7. The transverse resolution of all OCT systems is determined by diffraction since they are built on a confocal microscope.

8. Adding lateral scanning to a low-coherence interferometer, allows depth resolved acquisition of three-dimensional (3D) information from the volume of biological material

All these characteristics of OCT put it as one of the best available imaging techniques that may be used in both directions which are the medical application and researchers study.

2.3 Application of OCT

Optical Coherence Tomography has applications in several general clinical situations. The applications of OCT extend to several clinical and biological fields, e.g., ophthalmology, dermatology, gastroenterology, cardiology, dentistry, and neurology. The rapid advancement of OCT technology has led to the development of ultrahigh-resolution imaging and high-speed real-time imaging. Furthermore, functional imaging has been developed for investigating polarization properties and blood flow and as a means of spectroscopic imaging [60].
OCT has the potential of achieving high-depth penetration, which is determined by the coherence length of the source. This is the length over which a process or a wave maintains strict phase relations; an ideal laser source, for instance, emits light with more than a few kilometers coherence length.
OCT has been used in a wide variety of applications in many different fields [61]:

- Ophthalmology: The first application of low-coherence interferometry in the biomedical optics field was for the measurement of eye length. These days, OCT helps for diagnosing retinal disease and abnormalities of the eye.

- Dermatology: OCT is one of the essential tools for early detection of skin cancer, diagnosing cancer disease and other problems.
- Cardiovascular: OCT helps for early detection of diseases by imaging the blood vessels and other cardiovascular areas.
- Biopsy and functional OCT: Optical biopsy promises to assess tissue and cell function and morphology in situation such as:
  - High-resolution OCT in gastroenterology
  - Endoscopic OCT in intra-arterial imaging
  - Polarization Sensitive OCT in dentistry
  - Spectroscopic OCT in gastroenterology
  - Doppler OCT in haemostatic therapy
- Non-medical OCT: Low coherence interferometry has been used in optical production nanotechnology, tissue engineering biomaterial and other technical fields, for example:
  - Industrial metrology as position sensor for thickness measurement of thin films.
  - For high density data storage on multi-layer optical discs.
  - Nondestructive evaluation to estimate residual porosity, fibre architecture and structure integrity.
  - Nondestructive evaluation of paints and coatings.

2.4 Principles of operation

The main core of Optical Coherence Tomography imaging system is the interference which happens between the reference beam or the light source of the system and the other beam which is reflected by the target. In a typical OCT, a Michelson interferometer can be considered as illuminated by an optical source (OS).

Light from the OS is divided into two beams by using a plate beam-splitter (BS) and which may be replaced sometimes by a fibre beam- splitter to be termed a directional coupler (DC). This has all the properties of a bulk beam-splitter plus the advantage that the input and the output ports can easily be altered by moving the fibre ends. This is exploited in delivering light to the tissue and collecting the back-reflected light via an optical fibre. The two beams, reference and object, are recombined by the beam splitter BS or by the directional coupler onto a photodetector as the figure below displays [61]. The interference amplitude of the beam depends on the degree of polarization and the degree of similarity of the orientation of the electric fields in the two optical beams.

The intensity of photostatted two partially coherent beams can be expressed as:

$$i_{ph} = \alpha \frac{P_0}{2}[O + R + 2\sqrt{OR}\Pi \cos(\frac{2\pi}{\lambda}d)] \tag{2.1}$$

where α is the photodetector responsivity, O the target reflectivity, R the reference mirror reflectivity, λ the central wavelength of the optical source, P_0 the power incident on the object, and d is the distance between the reference mirror and BS. The first two terms represent time non-varying components and determine noise, usually O, R. The third term describes the interference intensity; this is periodic and dependent on d, λ and Π the degree of polarization. Each time the reference mirror is moved by an extra $\lambda/2$ determines a round trip of the optical path difference (OPD) of l.

As OPD between the two optical paths in the two arms determines the coherence length of the light source, the coherence length of OCT can be stated as:

$$l_c = \frac{4\ln 2}{\pi}\frac{\lambda^2}{\Delta\lambda} \tag{2.2}$$

In general, the principles of OCT operation vary from one system to another and depend on the kind of approaches and on the aim of its use.

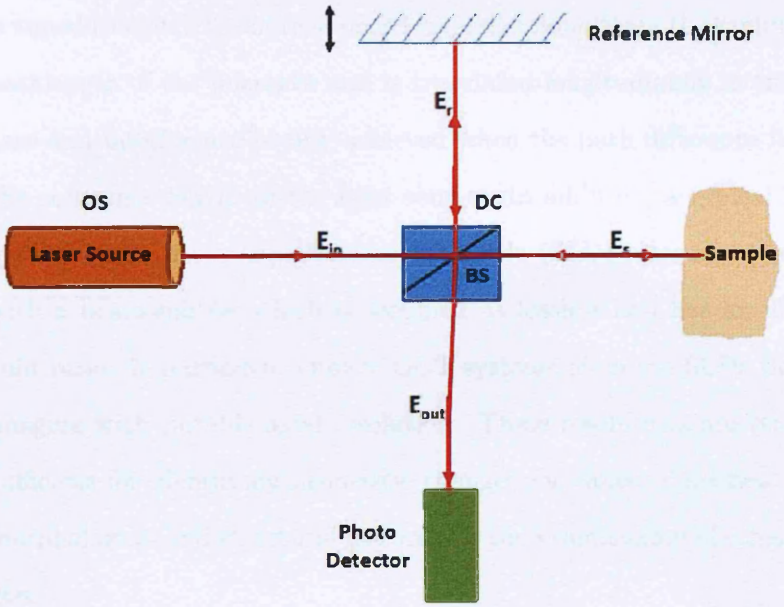

Figure 2.1: The basic components of Optical Coherence system [adopted from [61]]. E_{in} is the optical field in the input, E_{out} is the optical field in the output, E_r is the optical field in the reference, E_s is the optical field in the sample, OS refers to optical source, BS refers to beam splitter, and DC is direct coupler.

2.4.1 Different OCT versions

There have been three basic approaches of OCT which are different from each other in terms of the components and the operations [62]. In this section, the general information about every method will be described and then the sensitivity of every technique will be widely studied to draw a conclusion about the suitable method for our work.

1. **Time domain OCT**: The most popular form of OCT is TD-OCT which operates as explained in the figure (2.1) by varying the OPD in the in-

terferometer to output a reflectivity profile in depth. A reference mirror is scanned to match the optical path from reflection within the sample and the pathlength of the reference arm is translated longitudinally in time in this case and interference is only achieved when the path difference lies within the coherence length of the light source. In addition, a typical TD-OCT system might use a superluminescent diode (SLD) laser source operating with a beam-splitter which is assumed as lossless and has an ideal 50:50 split ratio. In particular, clinical OCT systems often use SLDs that enable imaging with suitable axial resolution. These resolutions are typically insufficient for identifying neoplastic changes for cancer detection, or tissue morphological and structural features for the visualization of other pathologies.

2. **Spectral Radar or Fourier domain OCT**: This kind of OCT has the advantage that no moving parts are required to obtain axial scans. The reference path is fixed. A stationary mirror and spectrometer are used instead of the reference mirror and the photo detector as shown in figure (2.2). Spectral Radar or Fourier domain OCT relies on the demodulation of the optical spectrum output of an interferometer; therefore, the detected intensity spectrum is Fourier transformed into time domain to reconstruct the optical depth resolved of the sample structure. In a real system, the output intensity spectrum is a set of the discrete data points corresponding to an intensity measurement from each detector in the array. The scan rate can be limited by the rate at which data can be transferred from the detector to a computer for processing. The system is able to obtain a direct measurement of the scattering amplitude along a vertical axis, and cross section images for a sample, which can be combined to reconstruct a 3D image. Typical scan depths of highly scattering biological samples range from 1 mm to several millimeters, depending on the scattering properties of

the sample. FD-OCT is more sensitive and faster than earlier OCT systems, which improves the data acquisition speed and image quality. Most of the recent studies have confirmed that FDOCT or SROCT can provide a signal to noise ratio more than 20 dB better than the TD-OCT. Moreover, it provides subsurface cross-sectional fast images with micron-level resolution [63].

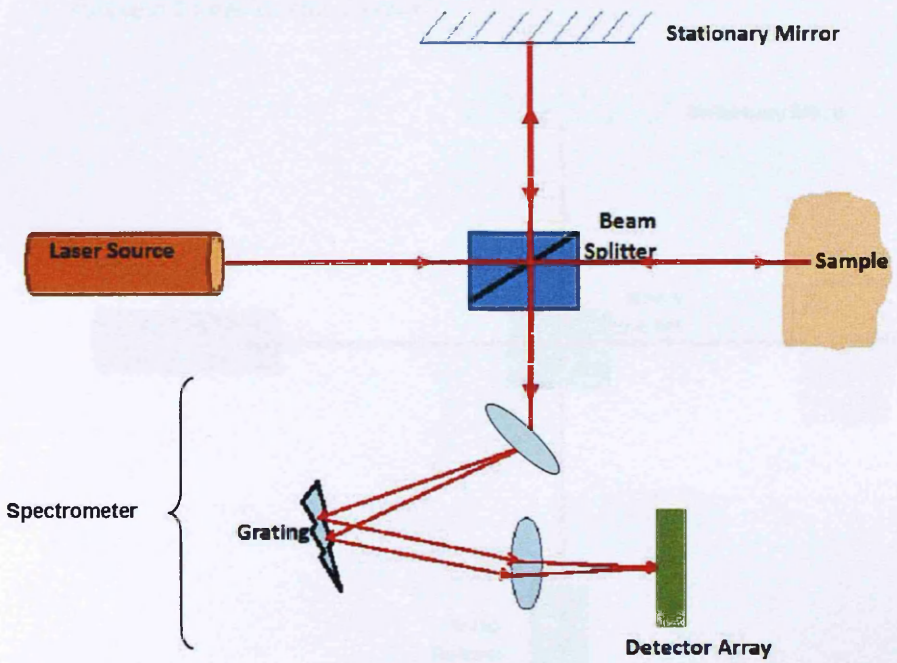

Figure 2.2: Schematic of Spectral Radar Optical Coherence Tomography shows the main principles of the operation [adopted from [63]]

3. **Swept source OCT**: SSOCT employs a wideband source in contrast to both the previous approaches to OCT which use a laser source for operating; however, the spectral intensity of the monochromatic light may be too low for imaging high scattering media if only single conventional SLD is used. Swept Source OCT is performed by using a signal detector which could be achieved by sweeping the source spectrum and then detecting the intensity

due to the component frequencies as figure (2.3) displays. This system can present 2D cross section imaging, volume images, and flow imaging [64]. In specific, SSOCT suffers from the same disadvantage as SROCT, as the modulation of frequency of the interferogram is proportional to the absolute value of the OPD. In addition, the achievable signal to noise ratio is similar to that obtained by SROCT system; however, the axial resolution is less in this case compared to the previous approach which makes SROCT more suitable to use in this research.

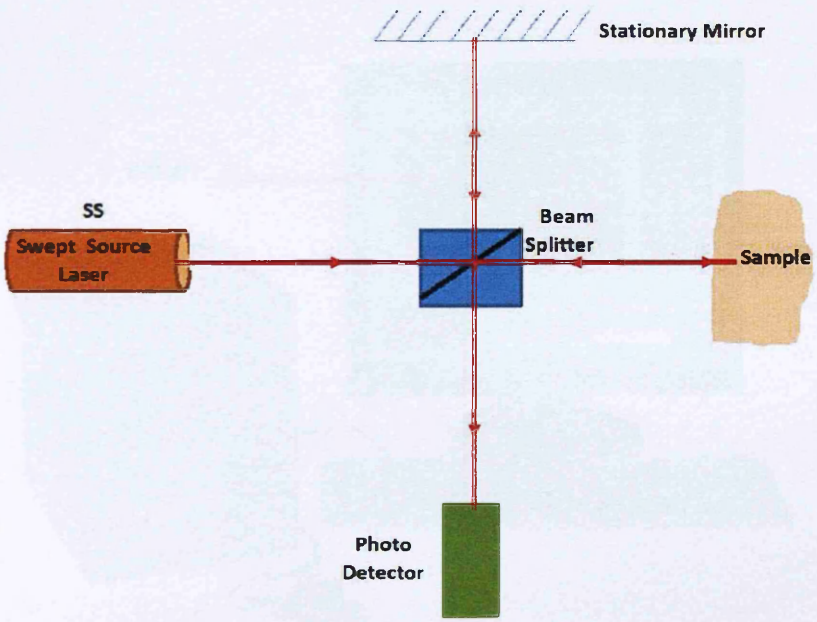

Figure 2.3: Schematic of Swept Source Optical Coherence Tomography shows the main principles of the operation [adopted from [64]]

2.5 SROCT Experimental set-up

This system was used during our research due to its ability for obtaining a direct measurement of the scattering amplitude along a vertical axis within a bulk sample. In addition, it can be used for a wide range of real-time monitoring

applications, from biological and clinical applications, to manufacturing and material science. Also, it provides a real-time high resolution surface and sub-surface imaging of human skin, making this system ideal for many dermal and sub-dermal applications which will guide us to achieve our aim of this research by visualizing the blood vessel oscillations under human skin in real time.

Spectral Radar OCT imaging system as is shown in figure (2.4) [65], it comes standard with three main parts: a base unit, a handheld probe and PC.

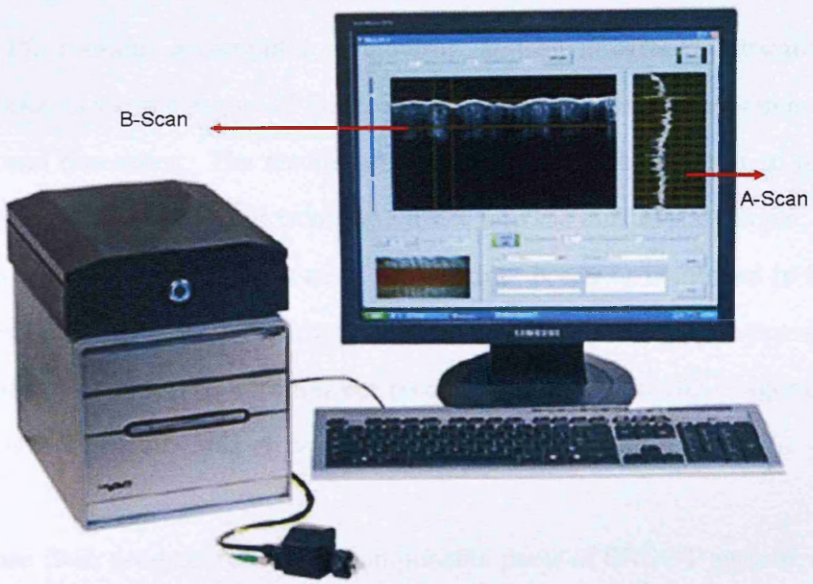

Figure 2.4: Spectral Radar Optical Coherence Tomography (SROCT), Thorlabs, USA [65].

1- The base unit is the main unit of the SROCT; it contains the broad super luminescent diode (SLD) light source with center wavelength 930 $\pm$ 5 nm, and spectral band width 100 $\pm$ 5 nm which provides a balanced optimization of both the resolution and measurement depth. It yields an axial resolution of 6.8 μm and a typical imaging depth 1.6 mm, but the actual depth is dependent on individual

sample characteristic. Light from (SLD) is directed to the handheld probe scan, and then the backscattered and reflected light from the sample are collected back to the spectrometer with 0.14 nm through the probe. Other components in the base unit are high speed linear image sensor, analog, the digital time circuitry and drive electronics for the scanner.

2- The handheld probe designed to keep the beam perpendicular to minimize image distortion over a working range. It contains an internal interferometer integrated directly to the probe. It is supplied by optical fibre with direct light from (SLD) source into the handheld probe, and the scattered light travels back along the same fibre to the spectrometer.

3- The PC contains a computer, a monitor, and an integrated software suite which contains a complete set of functions for controlling data measurement, collecting, and processing. The results can be displayed on the monitor to provide the complete scattering profile from the surface into the bulk of the sample, which is commonly referred to as an A-scan. In addition, it can be combined to form a cross-sectional image, which is commonly referred to as a B-scan, to present the 2D images at rates, up to 8 frames per second. Moreover, the 3D images can be reconstructed by combining cross-sectional images (B-scans) in sequence.

The figure (2.5) presents the major components parts of SROCT system, and it can be seen that the output of a broadband Super Luminescent Diode (SLD) light source is guided into a handheld Michelson interferometer probe, which splits the light into two separate optical paths. The reference arm path is terminated with a mirror, while the other path contains an imaging lens that focuses the light onto the sample. This same imaging lens is also used to collect light that is backscattered or reflected from the sample. The light returning from the end of both paths is recombined and directed into a spectrometer, which spatially separates the light to form the interference pattern that is then analyzed to yield the spectral OCT image [65].

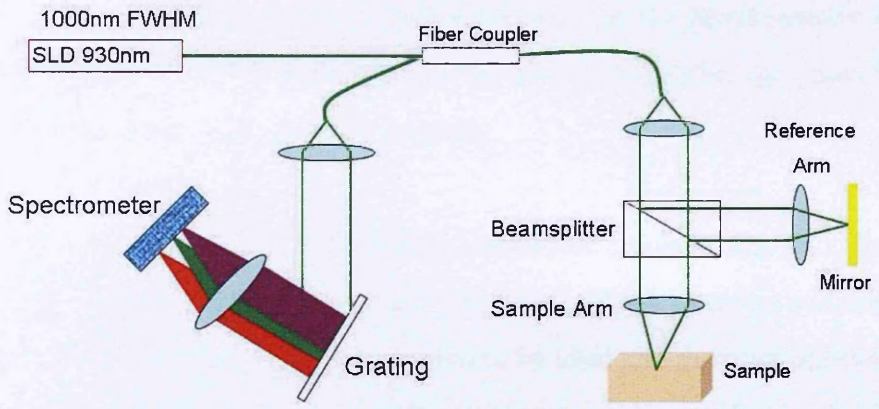

Figure 2.5: SROCT diagram showing the major components parts of the System [adopted from [65]]

2.6 Theory of SROCT

Since the Spectral Radar Optical Coherence Tomography is the instrument that was used for this research, the theoretical principles of SR-OCT should be studied to understand the results of the experiment. As understanding the theory of processing images obtained under human skin by using one of OCT techniques is not easy, we will start generally on the theory of OCT, then we will go specifically to SROCT.

OCT employs interferometric methods to detect laser light scattered from an inhomogeneous sample and recombined with laser source to obtain a sample's image. To explain OCT mathematically it is useful to express the electric field $E(\omega, t)$ as a complex expansion [66]:

$$E(\omega, t) = S(\omega)exp[-i(\omega t + kz)]. \tag{2.3}$$

This is a plane polarized solution to the wave equation, with source field amplitude spectrum $S(\omega)$, frequency ω and time variation t. The second term in the exponential, in terms of wave number k and distance z, simply accounts for

phase accumulated throughout the interferometer. As the interferometer measures the relative output phase between the two optical paths, the phase term can be dropped from the input electric field.

The field in each part of the OCT system is described as follow; E_{in}, E_{out}, E_r and E_s, corresponding to the optical fields in the input, output, reference and sample. Moreover, the reference mirror is supposed to be ideal and the beam splitter has a reference T_r and sample arm intensity transmittance has a reference T_s. Both references are related as $T_r + T_s = 1$.

Therefore, the components of optical field from the figure (2.1) are:

$$E_{in}(\omega, t) = S(\omega)e^{-i\omega t} \tag{2.4}$$

$$E_r(\omega, t, \Delta z) = \sqrt{T_r T_s}E_{in}(\omega, t)e^{-i\phi(\Delta z)} \tag{2.5}$$

$$E_s(\omega, t) = \sqrt{T_r T_s}E_{in}(\omega, t)H(\omega) \tag{2.6}$$

$$E_{out}(\omega, t, \Delta z) = E_r(\omega, t, \Delta z) + E_s(\omega, t, \Delta z), \tag{2.7}$$

where $\Delta z = \Delta t c/n_{air}$, and $\phi(\Delta z)$ is the phase accumulated in translating the reference mirror by geometric distance, which can be described as:

$$\phi(\Delta z) = \frac{2\omega n_{air}\Delta z}{c}. \tag{2.8}$$

n_{air} is the refractive index of air, Δt is the optical path difference, and c is speed of light.

The intensity is proportional to a time average over the electric field multiplied by its complex conjugate:

$$I(\omega, \Delta z) =< E_{out}E^*_{out} >\}, \tag{2.9}$$

from this point, $I(\omega, \Delta z)$ can be expressed as:

$$I(\omega, \Delta z) =< E_s E_s^* > + < E_r E_r^* > +2\Re\{< E_s E_r^* >\}. \quad (2.10)$$

The first two parts can be indicated as self interference, while on the contrary the last term is the real part $\Re\{\}$ of the complex cross interference.
By substituting equation (2.5), (2.6), (2.7) and (2.8) into equation(2.10), the intensity can be written as:

$$I(\omega, \Delta z) = T_r T_s S(\omega)|H(\omega)|^2 + T_r T_s S(\omega) + 2T_r T_s \Re\{S(\omega)H(\omega)e^{-i\phi(\Delta z)}\}, \quad (2.11)$$

where the sample response function $H(\omega)$ presents the reflection from all structures distributed in the z direction, and is described as

$$H(\omega) = \int_{-\infty}^{\infty} r(\omega, z) exp\left(\frac{-2in(\omega, z)\omega z}{c}\right) dz, \quad (2.12)$$

where $r(\omega, z)$ is the backscattering coefficient from the sample structural features, and $n(\omega, z)$ is the depth varying group refractive index as frequency dependent.

In the SROCT or FD-OCT the reference mirror is static $\Delta z = 0$ and the beam splitter is $50 : 50$, applying all that to equation (2.11) [67] we obtain:

$$I_0(\omega) = \frac{1}{4} S(\omega)\{H(\omega) + 1\}^2. \quad (2.13)$$

The Fourier transform of $I(\omega)$ into the time domain interference pattern $I(t)$ is applied to obtain the depth resolved structural data:

$$I(t) = FTI(\omega). \quad (2.14)$$

The detected spectral width $\Delta\Omega$ of Fourier transform result is determined in time $\Delta\tau$ by:

$$\Delta\Omega = \frac{2\pi}{\Delta\tau}, \tag{2.15}$$

and the detected spectral width can be approximated by this relation,

$$\Delta\Omega = 2\pi c\frac{\Delta\lambda}{\lambda^2}, \tag{2.16}$$

from this point, $\Delta\tau$ will be presented as follows:

$$\Delta\tau = \frac{\lambda^2}{c\Delta\lambda}. \tag{2.17}$$

In addition the depth of the field can be determined by multiplying the velocity of the light inside the medium and $\Delta\tau$

$$Z = \frac{c}{n_{ave}}\Delta\tau, \tag{2.18}$$

where n_{ave} is an assumed average sample refractive index. Therefore the maximum depth Z_{max} as a function of N the number of time domain points is

$$Z_{max} = \frac{Z(N/2)}{2}, \tag{2.19}$$

where N is divided by 2 to take into account the double pass of the light through the sample.

By subsisting equation (2.18) into equation (2.19),

$$Z_{max} = \frac{1}{4n_{ave}}\frac{\lambda_0^2}{\Delta\lambda}N. \tag{2.20}$$

The axial resolution of OCT is given by $R_{OCT} = l_c/2$ where l_c is the coherence length of the system

$$l_c = \frac{4\ln 2}{\pi}\frac{\lambda_0^2}{\Delta\lambda}. \tag{2.21}$$

Then the axial resolution of the OCT is

$$R_{OCT} \simeq 0.44\frac{\lambda_0^2}{\Delta\lambda}. \tag{2.22}$$

2.6.1 The Sensitivity of OCT

One of the advantages of OCT among all biophotonic sensing techniques is developed and non-expensive methodologies for signal optimization available to approach the detection limit of reflected photons. The sensitivity of OCT, also called optical dynamic range, can be defined as the ratio of the signal power generated by a reflection mirror P to the noise of the system [68].

Therefore the power signal to noise ratio SNR_P is

$$SNR_P = (\frac{signal}{noise})^2 = \frac{i_s^2}{i_n^2}. \tag{2.23}$$

The signal photocurrent at the detector i_s is equal to the total source power P in case of a perfectly reflecting sample and an ideal 50:50 beam-splitter and it can be written as

$$i_s = \frac{\eta q_e}{\hbar\omega_0}P, \tag{2.24}$$

where P is the integral of the source power spectral density $S(\omega)$, η is the detector quantum efficiency, q_e the electronic charge, $\hbar$ is Planck's constant divided by 2π

and ω_0 is the source center angular frequency.

The total noise current i_n can be determined as a sum of squares of the three significant sources of noise from the optical detecting in OCT which is shot noise i_{sh}, optical intensity noise i_{rin} and thermal noise i_{th}.

$$i_n^2 = i_{sh}^2 + i_{rin}^2 + i_{th}^2 \tag{2.25}$$

Shot noise i_{sh} occurs due to the random arrival time of electrons that create the photocurrent i_{dc} and can be expressed as

$$i_{sh} = \sqrt{2q_e i_{dc} B}, \tag{2.26}$$

where B is the detection band width, and i_{dc} is the dc photodetector current, which can be written in the case of an ideal 50 : 50 beam-splitter as

$$i_{dc} = \frac{\eta q_e}{\hbar\omega_0}\frac{P}{2}. \tag{2.27}$$

Optical intensity noise i_{rin} describes the beating between the constituent frequencies of the source spectrum and is given as

$$i_{rin} = i_{dc}\sqrt{\frac{B}{2\pi\Delta\omega}}. \tag{2.28}$$

Thermal noise i_{th} is generated by using an effective resistance R_{eff} by the photocurrent in the receiver electronics as

$$i_{th} = \sqrt{\frac{4kTB}{R_{eff}}}, \tag{2.29}$$

where T is the absolute temperature in Kelvin and k is Boltzman's constant.
In case of highly scattering biological samples, OCT can be arranged to achieve shot noise limited optical detection. Therefore, the RIN and the thermal noise in equation (2.26) become negligible (i_n=i_{sh}).
By substituting equation (2.25), (2.27) and (2.28) into equation (2.24), the shot noise limited power SNR of OCT is

$$SNR_P = \frac{\eta P}{\hbar\omega_0 B}. \tag{2.30}$$

B is the measurement bandwidth and is equal to $\frac{1}{2\tau}$, where τ is a function of the acquisition time for a single photodetector measurement.
In the case of Fourier domain OCT, the mean frequency domain noise current i_n transforms to the time domain current $\tilde{i}_n$ as

$$\tilde{i}_n^2 = 2\frac{i_n^2}{M}, \tag{2.31}$$

where M is the number of the detector that used to detect the light. Therefor, the FD-OCT power sensitivity can be written as

$$SNR_{FDOCT} = M\frac{\eta\tau}{\hbar\omega_0}P. \tag{2.32}$$

A high SNR ratio means a high image quality and more distinguishable image. To find out what is the best approach from OCT that provides a high quality images, we can compare the SNR of both SROCT and SSOCT systems which depends on Fourier Domain-OCT, with TD-OCT from equation (2.31), and equation (2.33):

$$SNR_{SROCT} = SNR_{SSOCT} = SNR_{TDOCT}\frac{M}{2}. \tag{2.33}$$

The factor of M/2 is the improvement of sensitivity in both SROCT and SSOCT

over the TD-OCT.

In summary, there are three main methods of OCT which are slightly different in the principles of operation due to the difference in the components inside the system. However, the most appropriate technique for this project motivation is SROCT as it is more sensitive than any other OCT systems, which are based on time-domain optical coherence tomography (TD-OCT). This increase in sensitivity significantly improves the data acquisition speed and image quality. The current spectral radar FD-OCT system enables a maximum speed of 8 frames per second, and an axial scan rate of $\sim$5 KHz, which makes it a feasible solution for real-time imaging in clinical, surgical, industrial, and material science applications.

Chapter 3

The Phantom

3.1 Introduction

The development of all diagnostic imaging systems and most physical therapeutic interventions has required the use of tissue-simulating objects to mimic the properties of human tissues. These are known as phantoms which are important tools for performance testing during system design, optimization of signal to noise ratio in existing systems and performing routine quality control of medical imaging systems without the necessity of in vivo scanning [69].

3.2 Construction of phantoms

Generally in medical optical imaging, a substance called Intralipid is widely used to simulate the optical absorption and scattering characteristics of the tissue because the refractive index value of the solution is nearly the same as most biological tissues [70]. Therefore, Intralipid solution was used in this research as main components of the phantom. It is private prescription item that can be found in a Pharmacy and should be stored in fridge. At each time of the measurement, the phantom should be prepared carefully by following these steps:

1. 0.3 g of a gelatine (Dr. Oteker, (UK) Ltd, Leeds, UK) was cut into small pieces.

2. The bottle of Intralipid was shaken before that as a chemist instructed, then a syringe was used to place about 1.5 ml of Intralipid solution on the small pieces of gelatine.

3. The substances left to soak for about 10 minutes in a small bowl.

4. The bowl was placed over a pan of gently simmering water for 2 minutes to melt the gelatine.

5. 30 ml of intralipid solution was pouring into the mixture.

6. The mixture was put into a rectangular plastic container with size of 7.5 cm $\times$ 5.4 cm $\times$ 1.5 cm.

7. The container left opening to air and placed into fridge to firm for about 1 hour.

8. The container was moved from the fridge before 30 minutes of the measurements to reach a room temperature.

9. The container was placed on a static table and the camera was fixed over it by stable holder to minimize any movements in phantom.

10. Different subjects were used to mimic the blood vessels during my measurements such as: fishing lines and bubbles.

11. In case of fishing lines, I immersed them into the box before putting the mixture into fridge.

12. Producing the bubbles was by pushing air using the syringe into the mixture after 30 minute from putting it into fridge and then returned back to the fridge immediately.

13. In certain studies, the mixture was left without any immersed subjects.

14. In a few measurements of a short study, the phantom was created without gelatine.

15. At the end of each day of the measurements, the phantom was discarded.

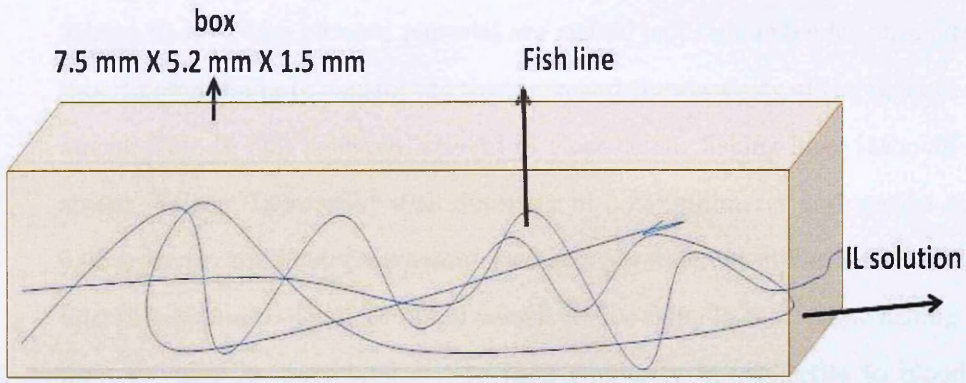

Figure 3.1: A Schematic of phantom represents several fishing lines immersed into Intralipid (IL) in a plastic box

As we can see from the figure (3.1) the main two components of Phantom that was created in our lab to mimic the human skin tissue and blood vessels under skin are Intralipid (IL) and fishing-lines.

- **Intralipid (IL) 20 %** is a fat emulsion, which is made of 20 % soya bean oil, 2.25 % glycerol, 1.25 %Egg Yolk Phospholipids, and water, designed primarily as a feed for "liquids only" hospitalized patients [71]. It was used because of its similarity to the viscosity of the blood and also it is a suitable tissue phantom material, because of its highly scattering and low absorption features. Moreover it is a relatively inexpensive material and readily available. Also its scattering coefficient can be easily adjusted by diluting this solution with water. Most of the experiments provided information that increasing concentration of the Intralipid solutions does not influence importantly the absorption coefficient, but has a large effect on the scattering coefficient [72]. In my experiments, I add the gelatin to firm the sample which is about 100% Pork Gelatine.

- **Several of fishing-lines** are made from a mixture of group materials polyethylene, nylon, dyneema and dacron and are known as monofilament fishing-lines. These blended material are melted and then extruded through tiny different holes to control the thickness and the elasticity of the monofilament [73]. In this research, several of clear colour fishing-lines (Monofilament, Falcon, Indonesia) with diameter of 0.23 millimeter and weight of 0.02 gram per millimeter were immersed at a few different millimeters depth into IL solution to simulate blood vessels under skin. In fact, these fishing-lines are used in mimicking due to their similarity in properties to blood vessels of absorbing light from the source. As we will notice, the skin image appears to have some black dots and lines due to the highly absorbing properties by the blood inside the vessels. Similarly, the images of fishing-lines in the phantom looks like black dots or black lines depending on the cross section of the camera system on the sample and resulting from the absorption properties of fishing-lines to the infrared light in the system.

Overall, to test the significance of our measurements before using them on human skin, the phantom has been created to mimic the human skin tissue and the blood vessels, using IL and fishing-lines. This helps to understand the precision and the reliability for all future measurements that will be made by SROCT on any selected sample.

3.3 Experimental set-up

In this section, I will focus on studying the images of the phantom by SROCT to evaluate the precision of the instrument and the way of analyzing the data. All tests were performed on the phantoms at the laboratory of the Physics department. Several phantoms were measured into the study by using the following steps:

1. The created phantom was placed on static table.

2. The camera was moved over the phantom, and the images was visualized on the monitor screen of SROCT system at the same time.

3. The area of the study was selected carefully depending on the required prof.

4. The camera was fixed over the phantom by a stable holder.

5. In the case of investigating the single image, the data was recorded for 10 seconds, which is about 80 frame images.

6. In the case of studying the information into the images over the time, the data was recorded for more than 10 minutes.

7. In certain studies, the phantom was placed on the human arm instead of the static table to mimic the actual body movement.

8. All recorded data were saved into a memory disk of SROCT system for future study.

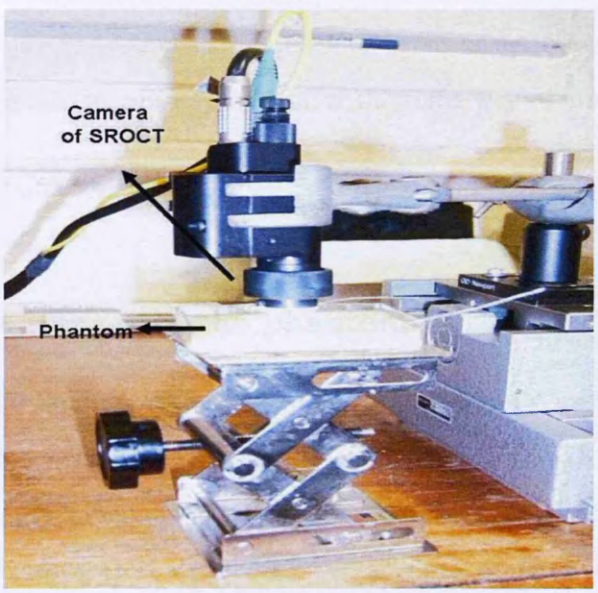

Figure 3.2: Phantom placed on the static table and imaged by a stable camera holder

3.4 Data Recording and results

In this section, several of data recording and related results in the form of figures and tables during all the experiments on the phantom will be discussed. In the first part, different phantom images will be displayed and then we concentrate on evaluating the accuracy of any measurement that will be acquired during this research by using different subjects. After that, the intensity of images by single pixel and the tracing of any changing of their values due to the depth will be studied. Then the correction factor from analyzing images will be found out to make sure any comparison of points at different depth in the same image is accurate. Next, the contour function by MatLab program is identified in order to plot it on simulated vessels in the phantom. Then, several images in sequence will be recorded from the stable phantom for several seconds in order to investigate the SROCT noise level. In the final section of this part, several three dimensional images for the phantom will be presented to provide a clear picture of all layers in phantom. Overall, the results that have been obtained from the phantom will be explained in every section in this part to bring an exactness and certainty of image information by SROCT and show the right way of analyzing the data collected for any chosen subject.

3.4.1 First images of the phantom

Here we describe the imaging results from the phantom by using SROCT. The figure (3.3) shows several appropriate resolution images ($\sim$ 6.8 μm) for several phantoms with approximate size (500 $\times$ 512) in pixels. These images are displayed in this section by using MatLab images processing program as has been explained in Appendix A-1.

It can be seen from the figure, that the first image shows the empty phantom which was made from the Intralipid solution and Gelatine in order to simulate

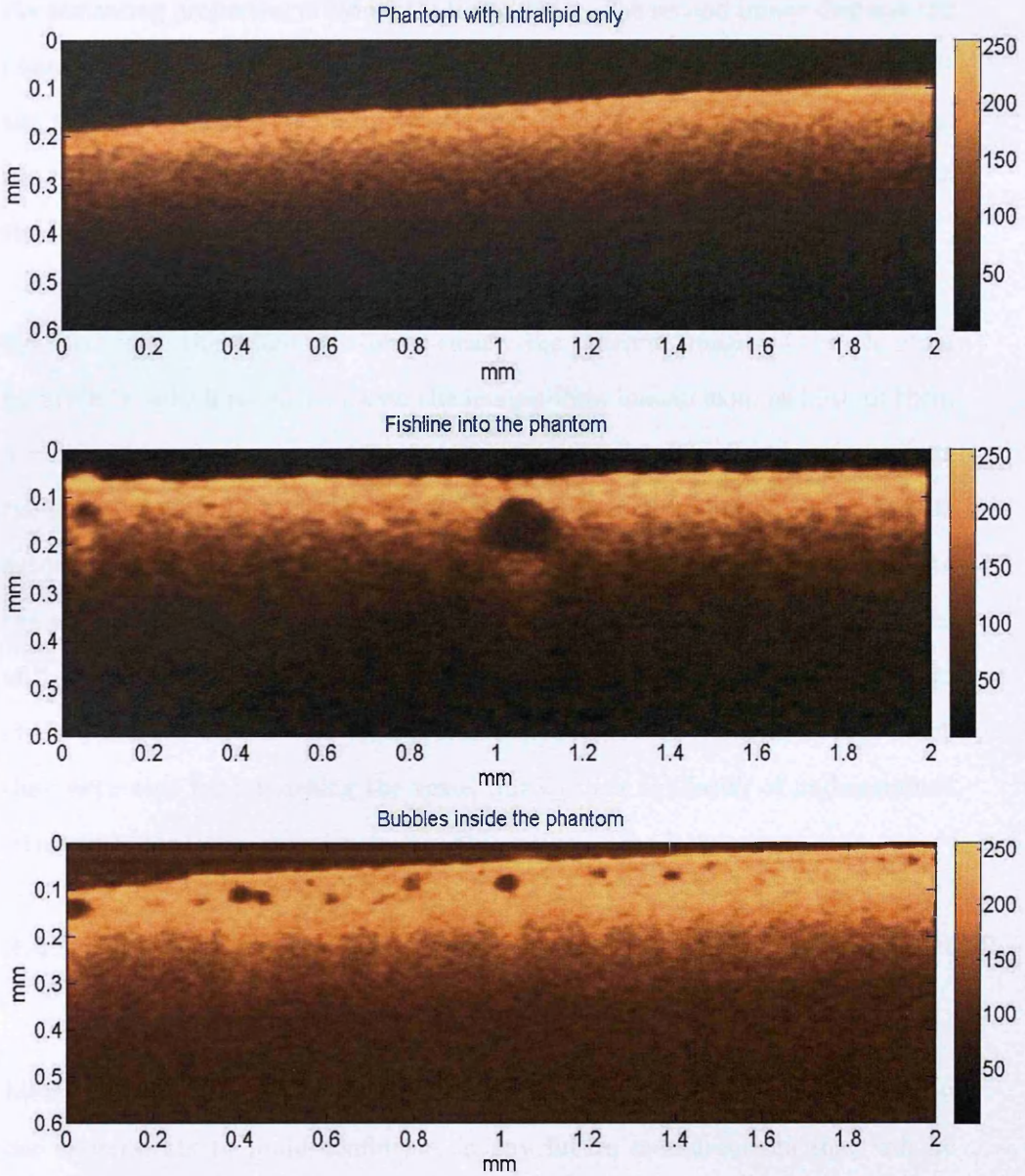

Figure 3.3: Different SROCT images of phantom with column intensity bars of the image pixels: the first one shows the phantom with full of Intralipid solution only, the second one presents the phantom with immersed fishing-line into Intralipid solution, and the last one shows the phantom with several bubbles inside Intralipid solution.

the scattering properties of skin for infrared light. The second image displays the phantom after immersing the fishing-line into the Intralipid solution to mimic the absorption characteristics of vessels under human skin. Finally, the last figure presents the image of the phantom with several bubbles inside it to simulate the features of unstable small vessels or capillaries.

On the whole, these figures express clearly the different images of the phantom by SROCT, which roughly imitate the images from human skin, as both of them have similar scattering properties for the infrared light. The first image presents the phantom with the mixture of IL and gelatine without immersed any additional subject inside. The second Image shows the images of immersed fishing-lines in the phantom, which appear as the black colours due to the absorption properties of fishing-lines to the system's light source. The final image displays the image of the phantom with several air bubbles, which appear as black dots, and which they were used for mimicking the vessel due to their similarity of undetermined structures, positions, movements and absorption to the light.

3.4.2 Protocols for the assessment of the accuracy of SROCT measurements

Identifying the accuracy of the SROCT measurement is a very essential step in our experiments to build confidence in any future measurements that will be made on phantom and then on human skin. The first step of all was to evaluate the precision of the SROCT by measuring a dimension of some known subjects and then calculating the percentage error of the results to assess the perfection of the measurement by the system used.

3.4.2.1 Using a polystyrene tube

In this part, a polystyrene tube (Adetch PFE Tube, England Adtech Polymer Engineering Ltd, Stroud, UK), was used. This tube has a dimension of 0.250 $\pm$

1 mm and 0.770 ± 1 mm of an internal and external diameters. The images of tube by SROCT were investigated at different cases and the dimensions of its internal and external diameter were measured in each case using a MatLab image processing toolbox to investigate the suitability of the system and the method of measurement Appendix A-2.

The polystyrene tube was imaged with Intralipid (IL) solution without gelatine at different casease. In the first case, the accuracy of the experiment was examined by imaging vertically a tube in air. Next, the same tube was imaged after immersed into the Intralipid solution (IL). Then, the same experiment was produced again in both previous cases, but at this time after filling a tube with IL solution. In each case, the dimensions were measured using the MatLab images Processing toolbox. Then, the results were compared with the real dimensions taken into account the refractive index of different mediums of each layer to provide an accurate dimension result. The values of refractive index for used subjects are 1 for air, 1.55 for the tube (polystyrene) [74] and 1.4 for IL [75]. In general, the refractive index of medium n_{medium}

$$(n_{medium})$$
$$(n_{medium}) = \frac{The\ measured\ dimension}{The\ real\ dimension}$$

- **Measuring the tube in air**: The empty tube in air was imaged 3 times by using SROCT. First, the tube was placed on the table. Next, the camera of the system was moved on the tube to find the best position for a vertical cross section image. Then, the image was recorded for 1 second, which created 8 frames of images. After that, the tube was moved twice and then imaged again at each time using the same steps.

  After finishing the experiment, the dimensions of the tube were calculated by using MatLab program for each time. It can be seen from the figure (3.4 (b)), Moreover, the red line refers to the real value of the internal diameter of the tube.

(a) (b)

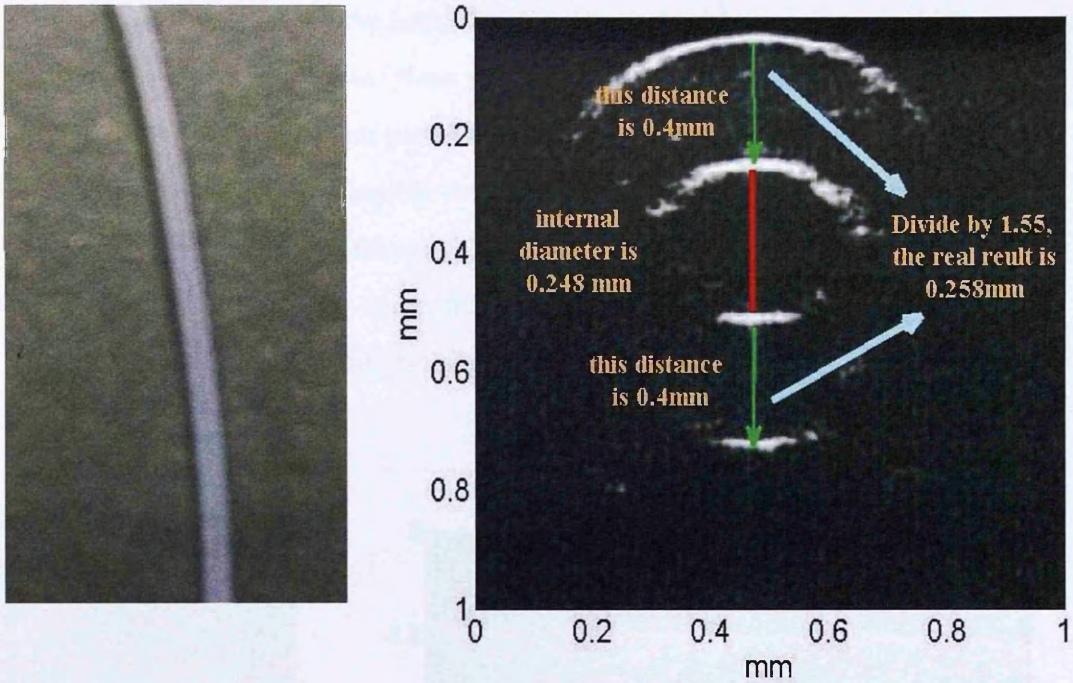

Figure 3.4: Measuring the tube in air: (a) the tube in air, (b) the image by SROCT of the tube in air with labeled values of measured dimensions (the green arrows represent the shell and the red line represents the internal diameter of the tube)

Experiment number	Measurement value (mm) of the internal diameter - the shell	The error %
1	0.248 - 0.258	0.8% - 0.77%
2	0.248 - 0.259	0.8% - 0.38%
3	0.249 - 0.258	0.4% - 0.77%

Table 3.1: The three measurements of the internal diameter and the shell of the same tube with the percentage error comparing to the real values

These three measurement were presented in the table (3.1) to compare the measurements value with the real values and to show the accuracy of the reproducibility of the measurements by SROCT. It can be concluded that there is a minimal error of the measurement which is generally up to 0.8%.

- **Measuring the tube in Intralipid**: The empty tube in Intralipid was imaged 3 times as well by using SROCT. First, the tube was immersed into Intralipid at a plastic box. Next, the camera of the system was moved on the solution to select the best position for a cross section image. Then, 8 images were created by recording the data for 1 second. After that, the same tube was imaged twice at different points using the same previous experimental steps. After that, one image from each experiment was selected and the dimensions was measured by using MatLab program.

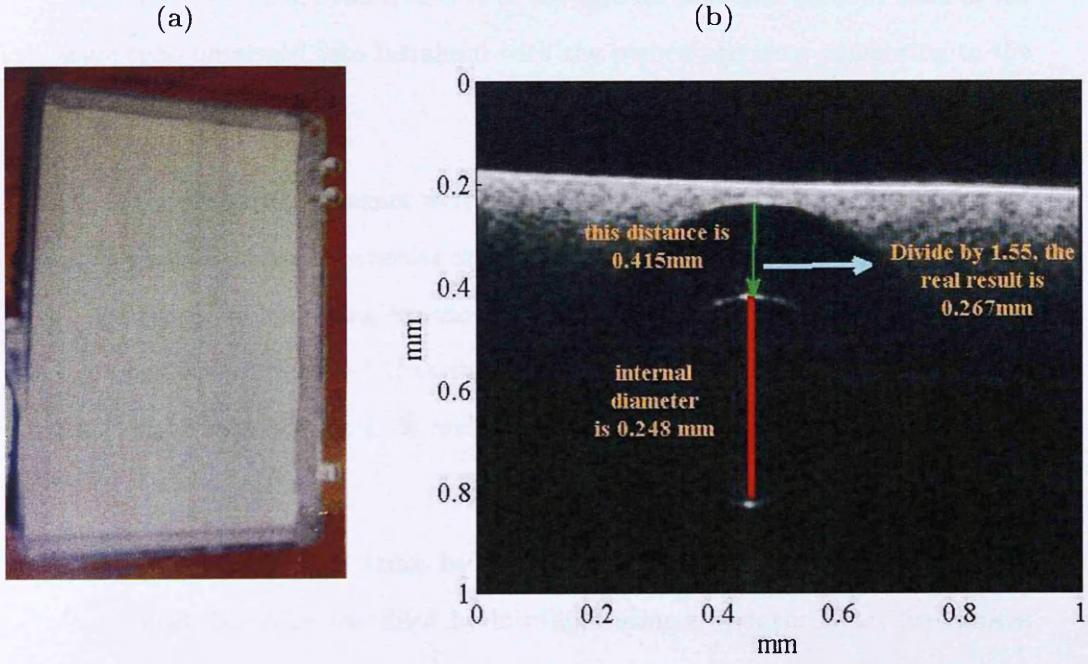

Figure 3.5: Measuring the tube in Intralipid solution: (a) the immersed tube into Intralipid solution, (b) the image by SROCT of the tube into Intralipid solution with labeled values of measured dimensions (the green arrow represent the shell and the red line represents the internal diameter of the tube)

From the figure (3.5), it can be seen that it is difficult to catch sight of the external diameter in depth after immersion into IL due to the high scattering of the light in the solution, which makes the lower side of the tube undetectable. The green line refer to the shell of the tube and its value

before applying the refractive index and the red line refers to the internal diameter in air.

Experiment number	Measurement value (mm) of the internal diameter - the shell	The error %
1	0.248 - 0.267	0.8% - 2.7%
2	0.249 - 0.265	0.4% - 1.9%
3	0.248 - 0.266	0.8% - 2.3%

Table 3.2: The three measurements of the internal diameter and the shell of the same tube immersed into Intralipid with the percentage error comparing to the real values

The three measurement were displayed in the table (3.2) to show the accuracy of the measurements and its reproducibility SROCT. In this circumstance, by matching up the results with the real magnitude of the tube layers, we identified that there is a slightly different value of the length which is between $\pm 1.9\%$ and $\pm 2.7\%$ from the real value.

- **Measuring filled tube by Intralipid in air**: In this case of the experiment, the tube was filled by Intralipid using a syringe. Next, the camera of the system was moved on the tube to find the best cross section image. Then, SROCT was used 3 times to image the tube at different points as previous experiments. Each time, the data was recorded for 1 minute. Last, the dimensions was measured for each time by using MatLab program.

As can be seen from the figure (3.6 (b)), it is barely possible to visualize the image for the complete tube and it is hard to measure the internal diameter of the tube because of the increasing scattering properties by IL in depth. Therefore, we just measured in this case the upper shell of the tube and

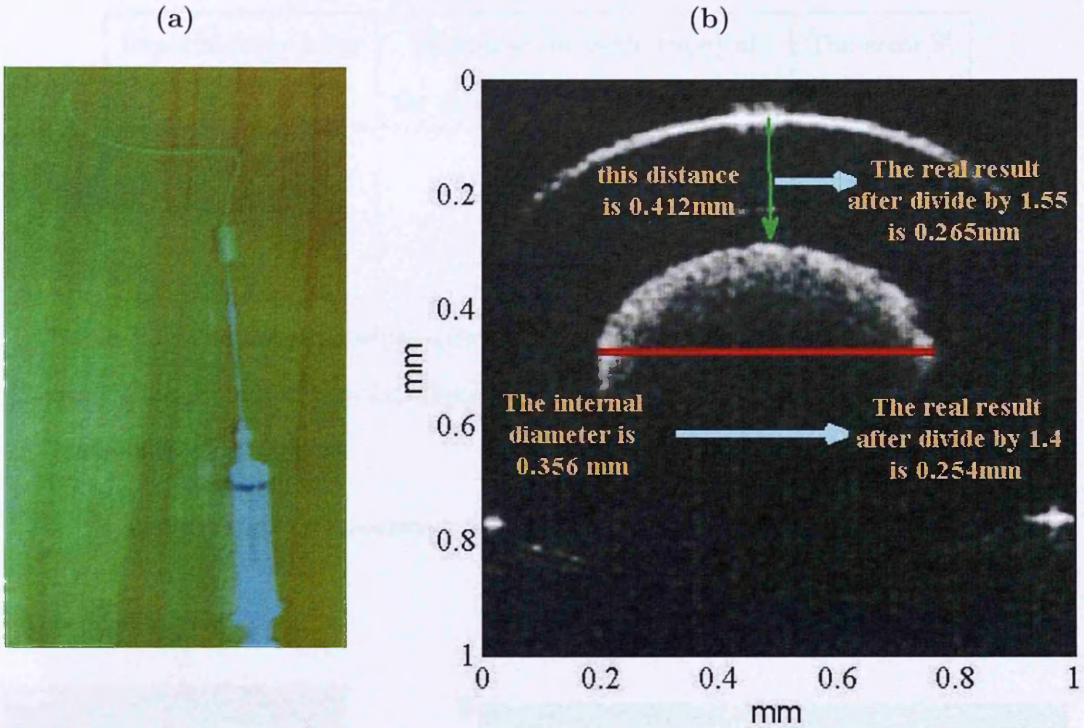

Figure 3.6: Measuring filled tube by Intralipid in air: (a) the filling tube by Intralipid in air, (b) the image by SROCT of filling tube by Intralipid in air with labeled values of measured dimensions (the green arrow represent the shell and the red line represents the internal diameter of the tube)

the width of the internal tube. The green line refer to the shell of the tube and its value before applying the refractive index. The red line refer to the internal diameter value before and after applying the refractive index value.

By matching up the results with the real magnitude of the tube layers in the table (3.3), we can notice from presented number that, there is a negligible error of the measurement as well, which is reached up to $\pm 1.9\%$.

- **Measuring filled tube by Intralipid in Intralipid**: In the last case of this part, we imaged filled tube with IL and then immersed it into the same medium as the figure (3.7 (a)) shows. Then, all previous steps of experi-

Experiment number	Measurement value (mm) of the internal diameter - the shell	The error %
1	0.254 - 0.265	0.9% - 1.9%
2	0.251 - 0.265	0.4% - 1.9%
3	0.249 - 0.264	0.4% - 1.7%

Table 3.3: The three measurements of the internal diameter and the shell of the same tube immersed into Intralipid with the percentage error comparing to the real values

mental setup and measurements were repeated in this case as well.

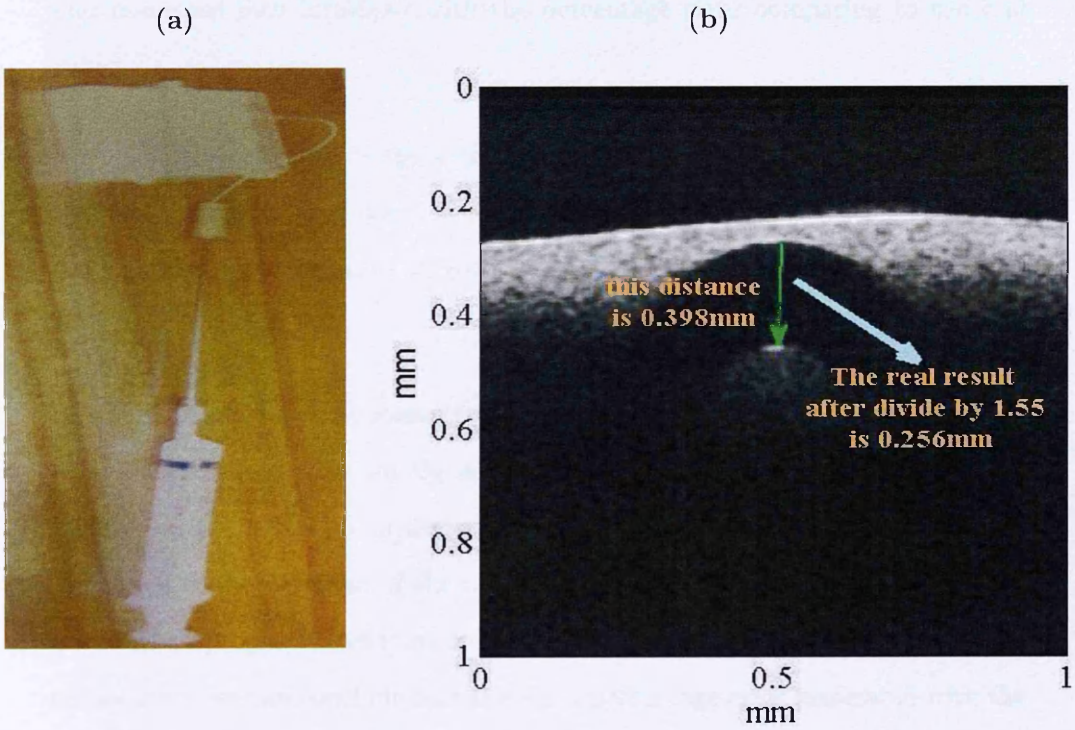

Figure 3.7: Measuring filled tube by Intralipid in Intralipid: (a) the filling tube by Intralipid in Intralipid, (b) the image by SROCT of filling tube by Intralipid in Intralipid with labeled values of measured dimensions (the green arrow represents the shell of the tube)

From the figure (3.7), it can be seen that the tube is harder to detect as the

depth increases due to the scattering of the light by IL from the surface of the tube. Therefore, we just measured the length of the upper shell of the tube which is marked by the green line into the figure.

Experiment number	Measurement value (mm) of the shell	The error %
1	0.256	1.5%
2	0.256	1.5%
3	0.255	1.9%

Table 3.4: The three measurements of the shell of the same filled tube by Intralipid and immersed into Intralipid with the percentage error comparing to the real values

The three results of the measurements were presented in the table (3.4) and it can be concluded from this case that the measurements provide a percentage error up to $\pm 1.9\%$.

In simple terms, all these steps of measurements are important in order to have a substantial evidence about the accuracy of the measurements that will be formulated in the future by utilizing SROCT, and to simultaneously get a strong indication of the precision of the technique and for analyzing the data by using the MatLab program. Referring to the previous figures and tables in this section on accuracy, we can conclude that there is a percentage error associated with the measurement by using SROCT and the MatLab analyzing program, which varies from $\pm 0.4\%$to$\pm 2.7\%$ depending on the case of the measurement. This conclusion brings a suitable exactness for measurements in any further experiments that may be planned by using this system.

3.4.2.2 Using Aluminum steps in the different media

The next step for checking the accuracy of the measurement was to create a model of aluminum steps. This calibration sample was made in Physics department workshop with varying values in depth and width to evaluate vertically and horizontally the measurement in micrometer scale. The figure (3.8) presents the real values of the steps as measured by digital caliper before experiment. The values by this caliper have a rated accuracy of 1 in 20 μm.

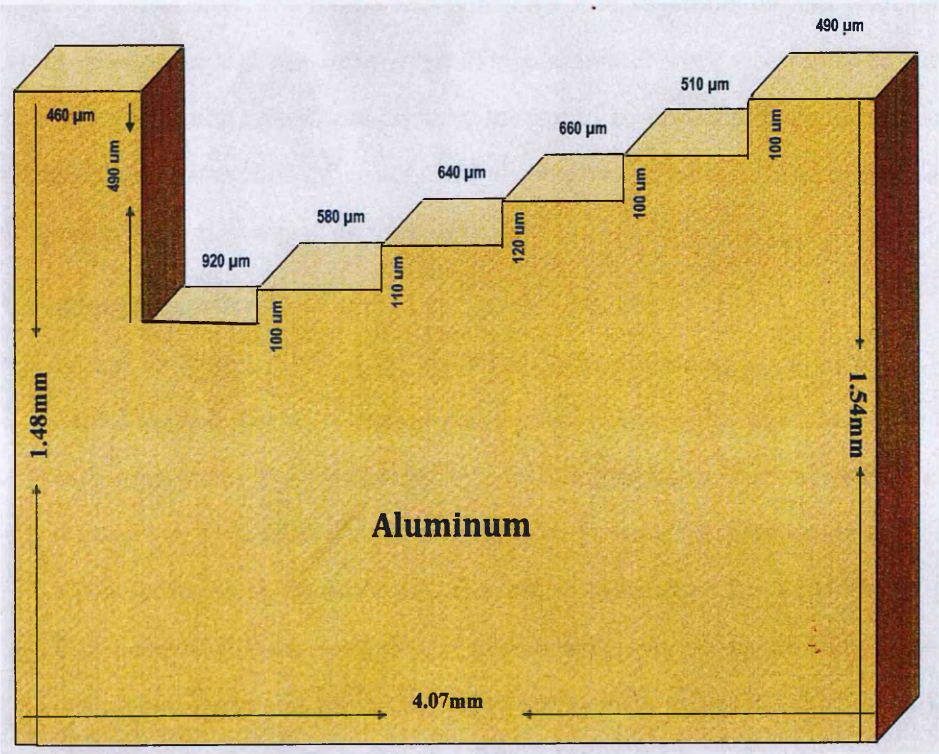

Figure 3.8: A Schematic of Aluminum steps with micrometer dimensions in width and depth for each step.

At this part of work, we aimed to be in no doubt on the accuracy of the measurement, by repeating the experiment with changing every time the medium into which the steps were immersed, to examine carefully the percentage error

for each dimension under dissimilar conditions and different optical properties of the medium.

All tests were performed on the Aluminum steps at the laboratory of the Physics Department by following the general experimental steps. First, the Aluminum steps was placed on the stable table. Second, the camera was moved over the table to find the steps and after that turned around the steps to find the cross section of the image. Next, the images was recorded for 1 second, which produces 8 frames of images. After that, the model was immersed into vegetable oil and then into Intralipid solution and the same steps of experimental work was repeated each time. Finally, the obtained images were measured to investigate the dimension of created images by SROCT using MatLab program. The results of these cases will be discussed at the next three parts.

- **Aluminium steps in air**

  Figure (3.9) shows the image by SROCT for aluminum steps in air. The light blue and the light orange colors display the width and the depth of each step as has been measured by MatLab program . The values of these dimensions were presented in the table (3.5) with the percentage error of the measurements comparing to the real values started from right to left.
  It is noticeable from the highlighted dimensions in the figure and the percentage errors in the table that there are slightly different values between the measurements in this case and the real magnitude of the tested subject. These minimal fluctuations of the measurements deviate up to ($\pm 0.6\%$) from the real value in case of width, and about ($\pm 1.6\%$)in depth, which provide the excellent results for measuring any selected subject in air by using both the SROCT imaging system and MatLab computer program.

- **Aluminium steps in oil**

  According to figure (3.10), the dimensions of the steps in oil look bigger

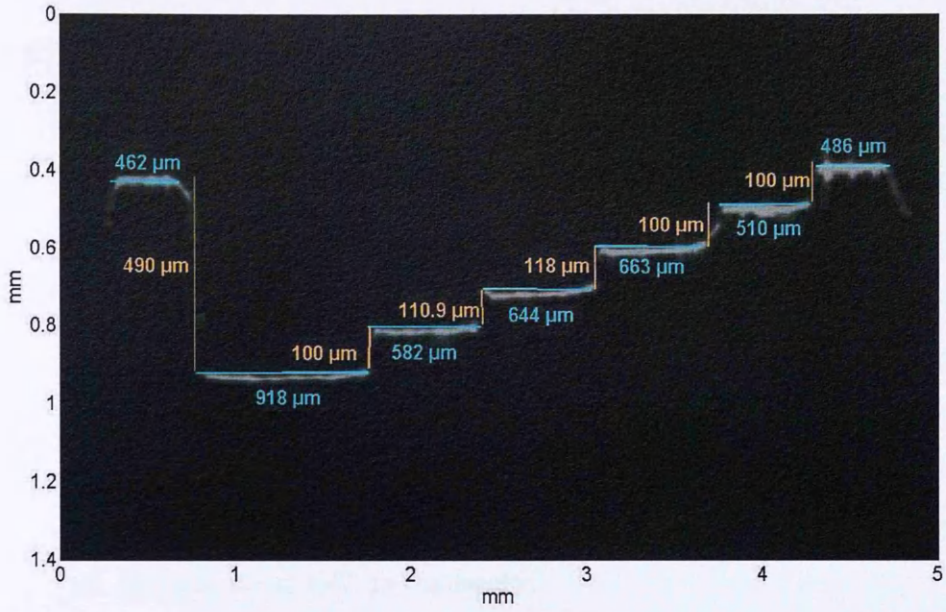

Figure 3.9: The image of Aluminum steps in air by SROCT with labeled values of measured dimensions (the light blue line represent the width and the light orange line represent the hight).

	Real dimensions (μm)	Measured dimensions (μm)	Error %
width 1	460	462	0.4 %
width 2	920	918	0.2 %
width 3	580	582	0.3 %
width 4	640	644	0.6 %
width 5	660	663	0.4 %
width 6	510	510	0 %
width 7	490	486	0.8 %
height 1	490	490	0 %
height 2	100	100	0 %
height 3	110	110.9	0.8 %
height 4	120	118	1.6 %
height 5	100	100	0 %
height 6	100	100	0 %

Table 3.5: The comparing of the real dimensions of Aluminum steps in air with measured one

than when they were in air due to the refraction of the light by the oil. This fact makes harder to display all the steps in the same image at the same time. Therefore, we selected the side that presents the deepest step to study the precision of the measurement in terms of depth. In this case, the light blue and light orange colors in this figures represent the width and the height respectively of the steps as measured by using our previous procedure. At the same point, the green numbers on the figure give the actual results for the depth after applying the refraction index value of the oil, which is about 1.47, to the results.

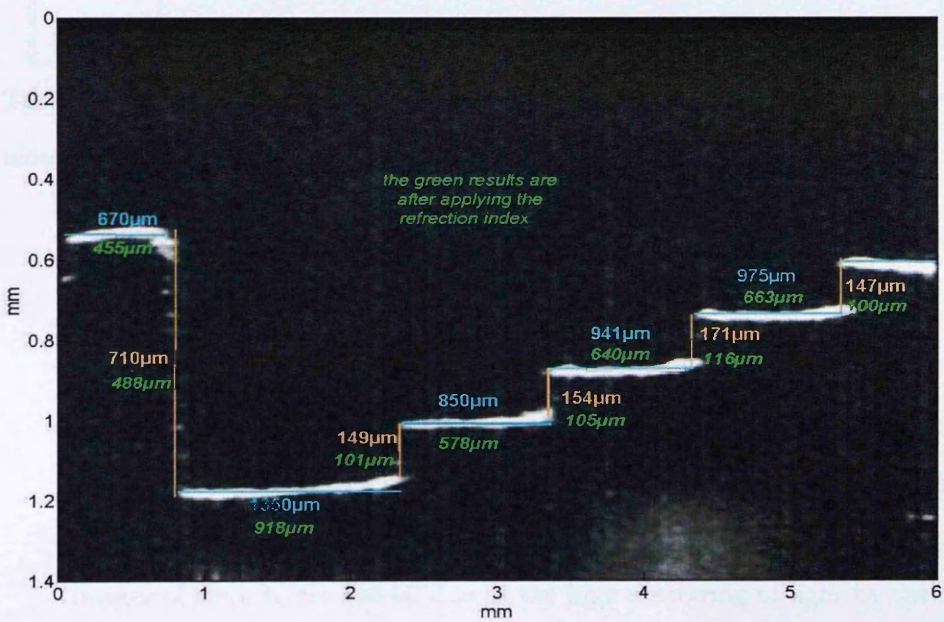

Figure 3.10: The image of Aluminum steps in oil by SROCT with labeled values of measured dimensions (the light blue lines represent the width, the light orange lines represent the hight and the green writing shows the calculated values of each dimension).

The table (3.6) presents comparing of the measured dimensions of Aluminum steps in the oil with the actual ones started from right to left. It can clearly be concluded that nearly the same values of the dimensions have

	Real dimensions (μm)	Measured dimensions (μm)	Error %
width 1	460	455	0.4 %
width 2	920	918	0.2 %
width 3	580	578	0.3 %
width 4	640	640	0.6 %
width 5	660	663	0.4 %
height 1	490	488	0.4 %
height 2	100	101	1 %
height 3	110	105	4.5 %
height 4	120	116	1.6 %
height 5	100	100	0 %

Table 3.6: The comparing of the real dimensions of Aluminum steps in oil with measured one.

been obtained in this case as well, with a deviation up to $\pm$ 4 μm ($\pm$ 0.6%) in width and $\pm$ 5 μm ($\pm$ 4.5 %) in depth.

- **Aluminium steps in IL**

  At the last figure in this section (3.11), we can visualize the image of the steps immersed into the Intralipid solution, which is less obvious than the images of steps in air and oil due to the high scattering of light by the IL. As in the preceding figure, the figure displays the dimensions in light blue for width and light orange for height as obtained by using our routine. Similarly, the green numbers give the true values of the dimensions calculated from the width and height of the steps corrected for the refractive index value of the Intralipid solution and which is about 1.4. All theses measured values were presented in the table (3.7) to show clearly all percentage error of the measurements.

By evaluating the results in this section, we found that the measurement of aluminium steps immersed into IL provides a very acceptable error result, which is between ± 0.8% in width and ± 4.5% in hight compared with the accurate dimension.

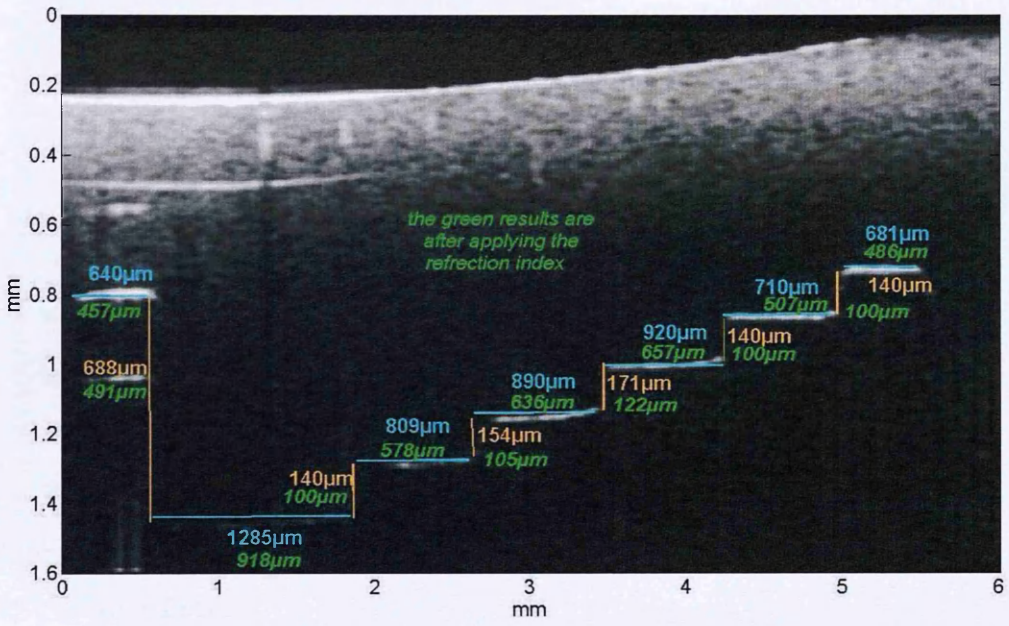

Figure 3.11: The image of Aluminum steps in Intralipid by SROCT with labeled values of measured dimensions (the light blue lines represent the width, the light orange lines represent the hight and the green writing shows the calculated values of each dimension).

In simple terms, this section of the results with aluminium steps shows clearly and substantially that there is only small percentage error in the measurement that may be made by using the selected technique. This experimental procedure indicate that the SROCT system and the MatLab images processing toolbox program provide a high percentage accuracy which give a certainty of confidence on all future measurement by using this routine.

	Real dimensions (μm)	Measured dimensions (μm)	Error %
width 1	460	457	0.6 %
width 2	920	918	0.2 %
width 3	580	578	0.3 %
width 4	640	636	0.6 %
width 5	660	657	0.4 %
width 6	510	507	0.5
width 7	490	486	0.8 %
height 1	490	491	0.2
height 2	100	100	0
height 3	110	105	4.5 %
height 4	120	122	1.6 %
height 5	100	100	0 %
height 6	100	100	0 %

Table 3.7: The comparing of the real dimensions of Aluminum steps in Intralipid with measured one

3.4.3 Reduction of intensity with depth

In this section we study the changing intensity of the images with every single pixel in mm depth to test out the accuracy of any future comparison that may be required between any different selected depths in the same image. To manage the completion of this aim, five phantoms, which were created from Intralipid solution and gelatin only, was imaged for 1 second using the same previous experimental steps in section (3.3), page 46. After that, the created images were studied by plotting the pixel values for each horizontal line in the image using a similar window width. These values of pixels represent the intensity at any point and they can be identified easily by MatLab image processing toolbox as described in Appendix A-3. In this experiment, the depth that has been used in SROCT window was 1.6 mm. Therefore, each pixels number can be converted easily to

millimeters depth as the obtained images are with fixed number of pixels, which are 500 × 512 (width × depth). In this matter, each 32 number of pixels represent 0.1 mm in depth, and each 25 number of pixels are standing for 0.1 mm in width.

The figure (3.12) presents an intensity as a function of depth within a small width window at the middle of the image from one of created phantoms. It is clear from the figure that there is always a gradual reduction in intensity with depth due to the scattering of the light by the phantom. This scattering reduces the ability of providing information by the depth and makes it hard to see any thing deeper than 0.4 mm from the surface. Moreover, it can be seen that there is a slight fluctuation in intensity for the same image at same depth due to the different time of the scattering from different points at the same depth.

It can be seen from the table (3.8) that there is a clear fluctuation of the range of the intensity at the same depth from all five imaged phantoms. In addition, there is an obvious reduction of these values as the depth increases from the surface.

Moreover, the intensity of the image for one of the phantoms was investigated at different selected windows and the results was presented in the table (3.9). It is clear from the table that there is always a reduction in intensity and a fluctuation of its value for all studied windows at the same phantom.

Overall, the intensity of image of five different phantoms was studied at the same position within the window. Moreover, the intensity of one of theses phantom images was investigated at different positions into the image window. The results from both cases indicated that there is a slightly fluctuation of the intensity values at the same depth and always a clear reduction of the intensity of the images measured by SROCT, due to the scattering of the light by the subject.

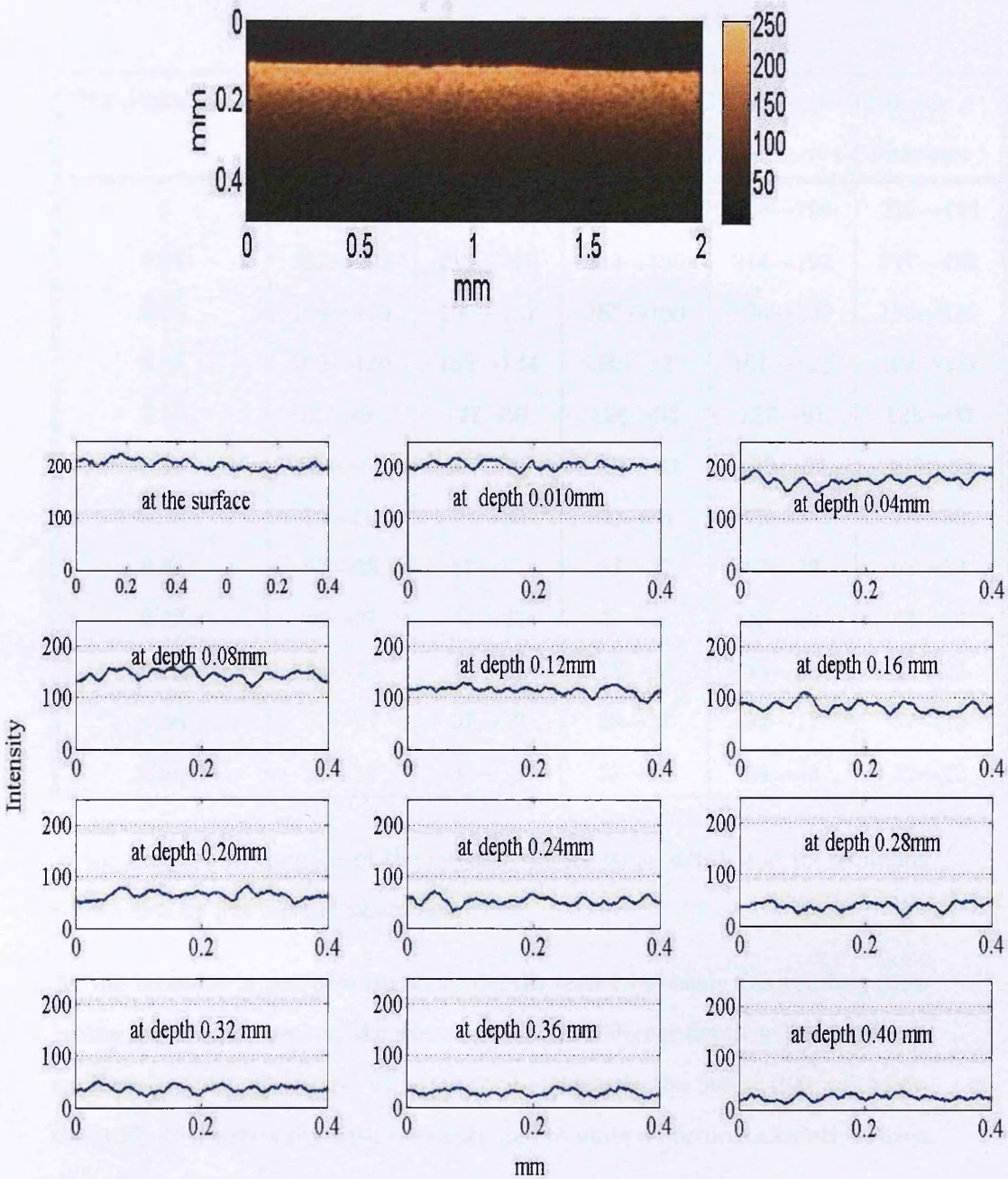

Figure 3.12: (a) SROCT image of the phantom with Intralipid and gelatin only, (b) Changing the intensity with depth along small width of the same phantom image

The depth (mm)	The range of the intensity values of 5 different phantoms				
	Phantom 1	Phantom 2	Phantom 3	Phantom 4	Phantom 5
0	223→195	220→196	219→197	220→199	223→198
0.01	217→190	210→190	212→195	214→192	217→192
0.04	190→159	190→157	187→160	190→159	190→159
0.08	160→120	162→124	160→120	161→123	162→122
0.12	127→91	127→91	126→93	127→91	125→93
0.16	109→67	107→69	107→69	109→67	107→69
0.20	79→50	79→50	80→53	79→53	78→53
0.24	67→33	67→33	63→37	67→33	67→33
0.28	48→21	47→25	48→24	48→23	48→24
0.32	45→25	45→22	45→23	43→22	45→22
0.36	37→17	37→19	38→17	34→17	37→19
0.40	34→13	34→13	32→12	34→13	32→12

Table 3.8: The fluctuation of the intensity at the same depth and its reduction with depth by five created phantoms

As the intensity is not uniform at all depths tested by using this routine, comparing any single points at the same image with different depth will not provide an actual result. Therefore, we attempted to identify the factor that will allow the study of the intensity with the depth and to unite all future calculations even with different depth and make any comparison between different depths more reliable.

3.4.4 Calculating a correction factor

Here, we made an effort to calculate the correction factor for phantom images by evaluating this changing of the intensity by depth at the same phantom and

The depth (mm)	The range of the intensity values at selected window (mm) the same phantom image				
	0→0.4	0.4→0.8	0.8→1.2	1.2→1.6	1.6→2
0	223→195	222→195	223→195	221→197	223→198
0.01	217→190	216→192	212→196	217→190	217→192
0.04	190→159	160→189	190→157	190→157	190→159
0.08	160→120	162→120	162→124	161→120	161→123
0.12	127→91	125→91	127→91	126→92	127→91
0.16	109→67	109→68	108→69	107→70	109→67
0.20	79→50	79→51	79→50	78→52	79→53
0.24	67→33	67→34	67→33	67→33	67→33
0.28	48→21	48→20	47→22	48→20	48→23
0.32	50→25	50→24	49→23	48→24	50→24
0.36	37→17	37→16	37→19	38→17	36→17
0.40	34→13	34→14	34→13	32→12	34→13

Table 3.9: The fluctuation of the intensity at the same depth and its reduction with depth at five different window

at nine different phantoms. The same previous experimental steps of studying the intensity by depth were made for the nine different phantoms. All phantoms were without immersing any subjects to not interrupt the pixel intensity values during the study.

The first investigation of this point was studying carefully the intensity values at different positions in width of the same phantom . First, one column from image pixels information was selected at different positions in width of the same image. Each pixel in the image represent the intensity value of that point in the image. Next, starting from the surface of the phantom, all pixel values were identified in

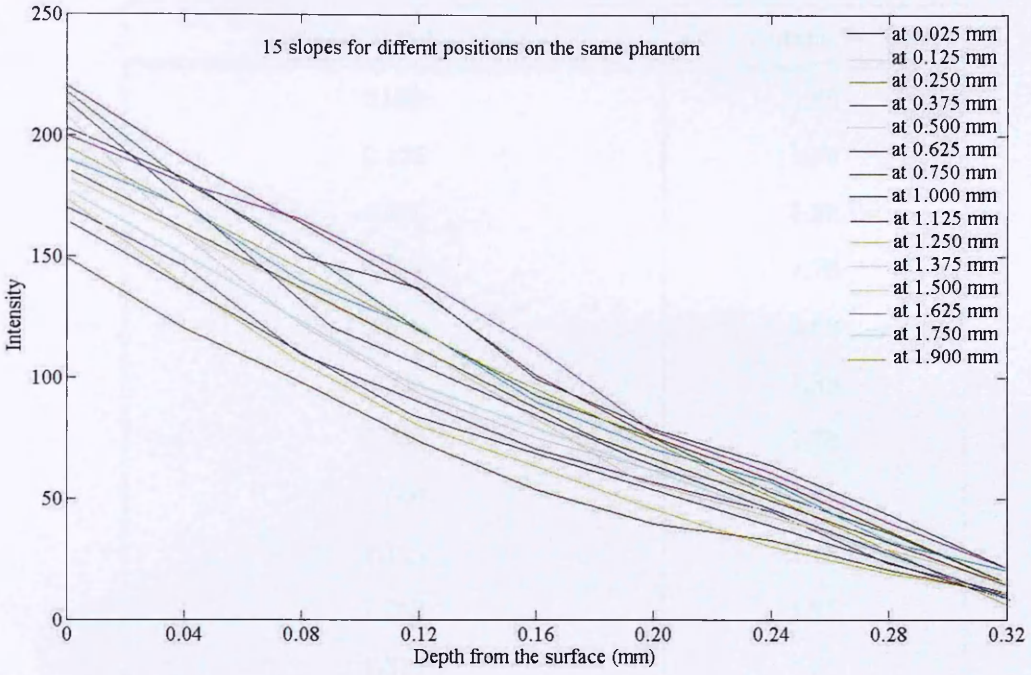

Figure 3.13: The reduction of the intensity by depth for the same phantom at different positions in width

that selected column. Then, by plotting the intensity values as a function of the depth in millimeters for different phantoms, a figure (3.13) is defined as described in Appendix A-4.

As an illustration showed in the figure (3.13) and the table (3.10), the slope varies from one position in width to another. The range of these slopes fluctuated between 1.6 and 2.0 intensity per single pixel. The variability of all theses values was calculated in the table and presented as a standard deviation (std). The value of standard deviation (std) was 0.11 intensity per pixel in this case and the mean value was 1.76 intensity per pixel.

The next investigation in this point was studying the intensity values of nine different phantoms at the same width position. First, one column of pixels at

position in width (mm)	slope (intensity pixel)
0.025	1.65
0.125	1.76
0.250	1.88
0.375	1.70
0.500	1.60
0.625	1.88
0.750	1.78
1.000	1.62
1.125	1.78
1.250	1.75
1.375	1.91
1.500	1.75
1.625	1.98
1.750	2.00
1.900	1.69
The mean (intensity \ pixel)	1.76
The standard deviation (intensity \ pixel)	0.11

Table 3.10: The calculated slopes at different positions and with the same width window of the same phantom with presented values of the mean and standard deviation of the slopes

the 9 obtained images was selected at the same position in width. Next, all pixel values were identified in that selected columns. Then, the same previous analysis by using MatLab program were made.

From the figure (3.14) and the table (3.11), it can be seen that the slope varies from one phantom to another. The range of these slopes fluctuated between 1.69 and 2.1 intensity per single pixel. The standard deviation (std) in this case was

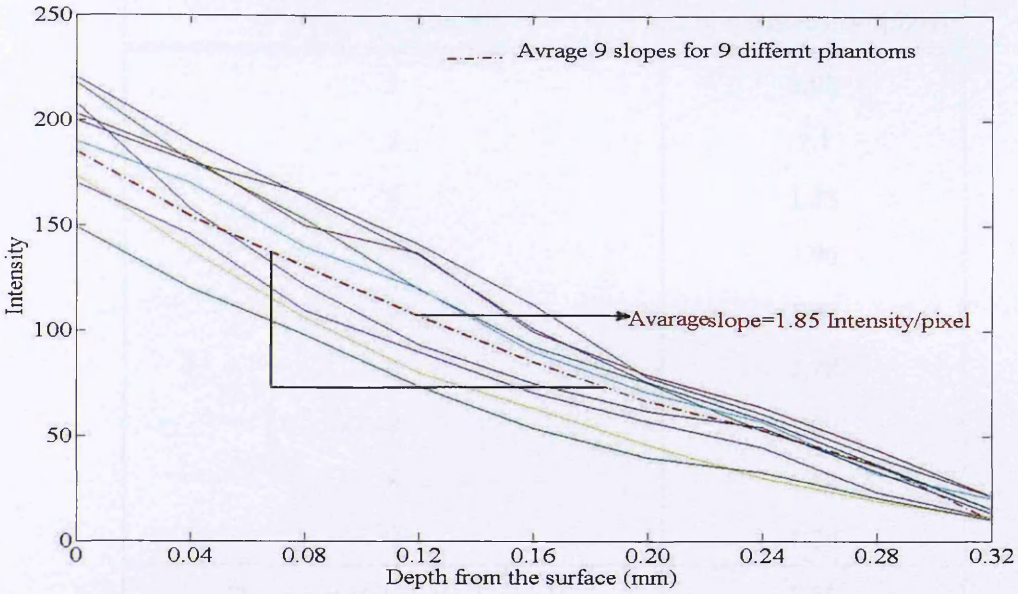

Figure 3.14: The reduction of the intensity by depth for several phantoms

0.12 intensity per pixel and the mean value 1.85 intensity per pixel.

From all the form of these results in this part, it can be conclude that the variation in value of the slopes can not allow an accurate value of the correction factor to be generally confirmed as standard in all future measurement. Therefore, we attempted to calculate the slope as each experiment as a first step in future work. Next step will be always finding out the correction factor for the intensity for the selected subject. Then, the correction factor will be applied to all the pixels in the image before any calculation.

The correction factor can be easily calculated to the image from following defined equation.

$$I_C(n) = I_n + (n-1) \times slope^{-1}, \tag{3.1}$$

where $I_C(n)$ is the intensity value after applying a correction factor, I_n is the intensity value before applying the correction factor, n is the depth of the pixel

phantom number	slope (intensity pixel)
1	1.95
2	2.1
3	1.88
4	1.90
5	1.75
6	1.78
7	1.69
8	1.82
9	1.79
The mean (intensity \ pixel)	1.85
The standard deviation (intensity \ pixel)	0.12

Table 3.11: The calculated slopes at the same width window position for 9 different phantoms with presented values of the mean and standard deviation of the slopes

starting from the surface of the phantom where n=1 with the maximum number of the pixel in depth is reached. As the maximum number of n is 512 by the SROCT images and this number represents 1.6 mm in depth, the unit of the slope is the intensity per number of pixel or the intensity per millimeter depending on the values of n that are selected in counts. To achieve this calculation, the MatLab function has been applied to all defined results as has been explained in Appendix A-5.

In simple terms, changing the intensity of pixels with depth was studied carefully of the same phantom at different width positions and of different 9 phantoms at the same width position to normalize the intensity at the same image even with different depth. The slopes of these changes were presented in terms of figures and tables. In particular, there were varies values of slopes of all cases.

For that reason, a correction factor for the phantom images was defined at each measurement case before applying any future calculations.

3.4.5 Contour

A contour function is very essential to fulfil the aim of this research because applying this function shows the shape of the blood vessel. In addition, it is clearly to follow the changes of the blood vessel in time, by plotting all frames as a montage image or by creating a movie to visualize the movement of created contour. In this research, a contour plot of image data was applied by using the MatLab image processing toolbox.

To manage the studying of this aim, one phantom was created by immersed fishing-line into Intralipid solution and gelatin as has been described in section (3.2), page 43. Next, the phantom was imaged for 1 second following the same experimental steps in section (3.3), page 46. The image data was processed by the MatLab Images program toolbox as follow: First, the created images were cropped around the fishing line area. Second, the contour function was applied to the cropped image. This function is displayed the figure of the contour automatically in MatLab. It works initially by computing the intensity values along a middle line in the cropped image and then plotting these values. This is known as the profile of the image. After that, the mean of the two maximum intensities on both sides, and then averaging a mean of the maximums with the minimum value in the profile curve is calculated. The obtained value is what the contour is detected into the image. Appendix A-6 explains this function in details.

The figure (3.15) describes the contour function for the fishing-line into the phantom before and after applying a correction factor. At the top, the figure (a) shows the image of the phantom with selected area around the fishing-line and then (b) displays a cropped small area from the image where the fishing-line is located

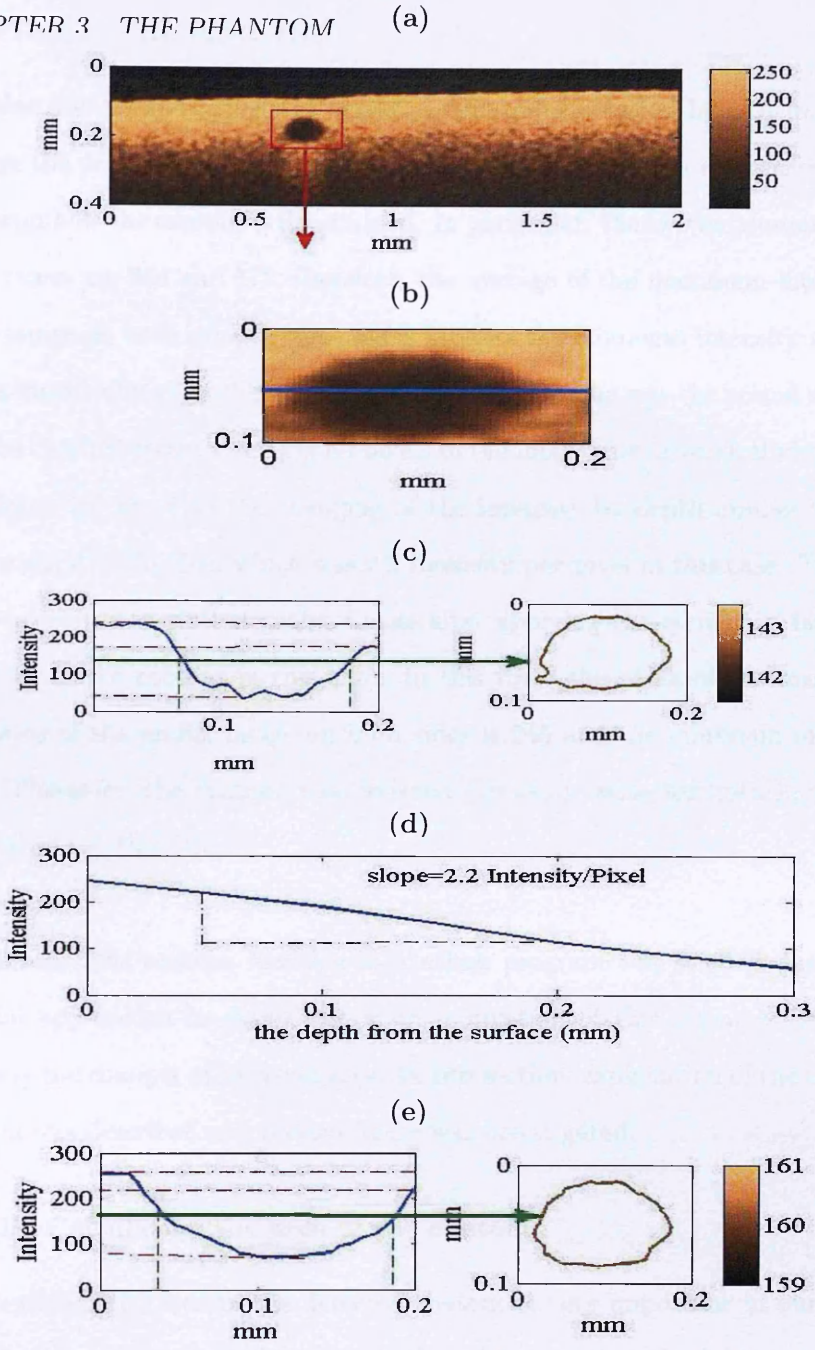

Figure 3.15: Steps of detecting a contour: (a) the fishing-line inside the phantom with presented intensity colour bar, (b) cropped image around the fishing-line, (c) the profile intensity of the image and the contour function before applying the correction factor with presented intensity colour bar, (d) the slope of changing intensity by the depth, and (e) the profile intensity and the contour function after applying the correction factor with presented intensity colour bar.

with blue line shows the place of detecting the profile image. The next image (c) displays the profile function of the small area before applying a correction factor to explain how the contour is determined. In particular, the two maximum values of the curve are 264 and 172; therefore, the average of the maximum intensities of the image on both sides in this case is 218. As the minimum intensity value is 67, the mean value of both intensities is 142.5. This value was the actual number that the contour detected among all pixels in the image from a vertical view. The next figure (d) presents the changing of the intensity by depth aiming to fond out the slope of the line, which was 2.2 intensity per pixel in this case. The last figure (e) shows re-plotted profile image after applying the correction factor to detect again the contour in this case. In this time, the mean of the maximum intensities of the profile image on both sides is 245 and the minimum intensity is 75. Therefore, the contour was detected the mean value for both intensities which is 160 at this point.

In summary, the contour function in MatLab program was studied due to its essential application to define the main motivation of this research, which is detecting the changes of a certain area. In this section, explanation of the contour function was described and related figure was investigated.

3.4.5.1 Calculating the area of the contour

As calculating the area of the detected contour is very important in our work, we looked for uncomplicated way to do this. The first step of calculation was to convert the image to the binary image which has typically just two possible pixel values 0 or 1. This type of image conversion works by identifying the half value of the maximum intensity in the image and then giving all values less than the calculated number the value of 0 and others the value of 1. After this conversion, the area of the contour is calculated by taking a sum of the zero pixels in the image, which appears as black, and then adapting the summation number to

mm^2 from the provided information on the system where (500 × 512) pixel point represent (2 × 1.2) mm^2 in this experiment. Appendix A-7 presents the code of this operation in MatLab format.

To manage this study, 10 different phantoms with immersed one fishing-line were prepared as explained in the section (3.2). Each phantom was imaged by using SROCT for 1 second at the same day. The fishing-lines into obtained images was analyzed using the described method in this section to calculate the area of the contour. The figure (3.15) presents the image of the fishing-line of one of theses phantoms and shows its conversion to the binary image. At the next, a comparison between the profile image of the same fishing-line before and after converting to the binary image is displayed to evaluate the function of the binary image. Finally, the figure presents the shape of contours side by side for the two cases to assess the approach of quantifying the area of the contour.
Using the method explained in the figure to calculate the area of the contour, the sum of the binary image pixels was identified as the initial step. After that, the summation was converted to mm^2 as explained before. Then, the area of the contour was defined after applying the refractive index value. In the figure (3.17), the calculated area of the contour was 4.14 E-2 mm^2. Comparing this result with the actual area of the fishing-line, which is about 4.15 E-2 mm^2, it can be seen that the measurement by using this method of computing the contour is a reasonable scheme because it provides an acceptable percentage error that is up to 0.24 % in this instance.

By repeating the same steps of calculation to all 10 measurement, the area of fishing liens can be presented as follow:
From the table (3.10), the area of the contour was calculated at each phantom and the mean value of these area was 4.13 E-2 mm^2. In addition, the percentage error of the mean values comparing to the real area was 0.67 %, which provide a

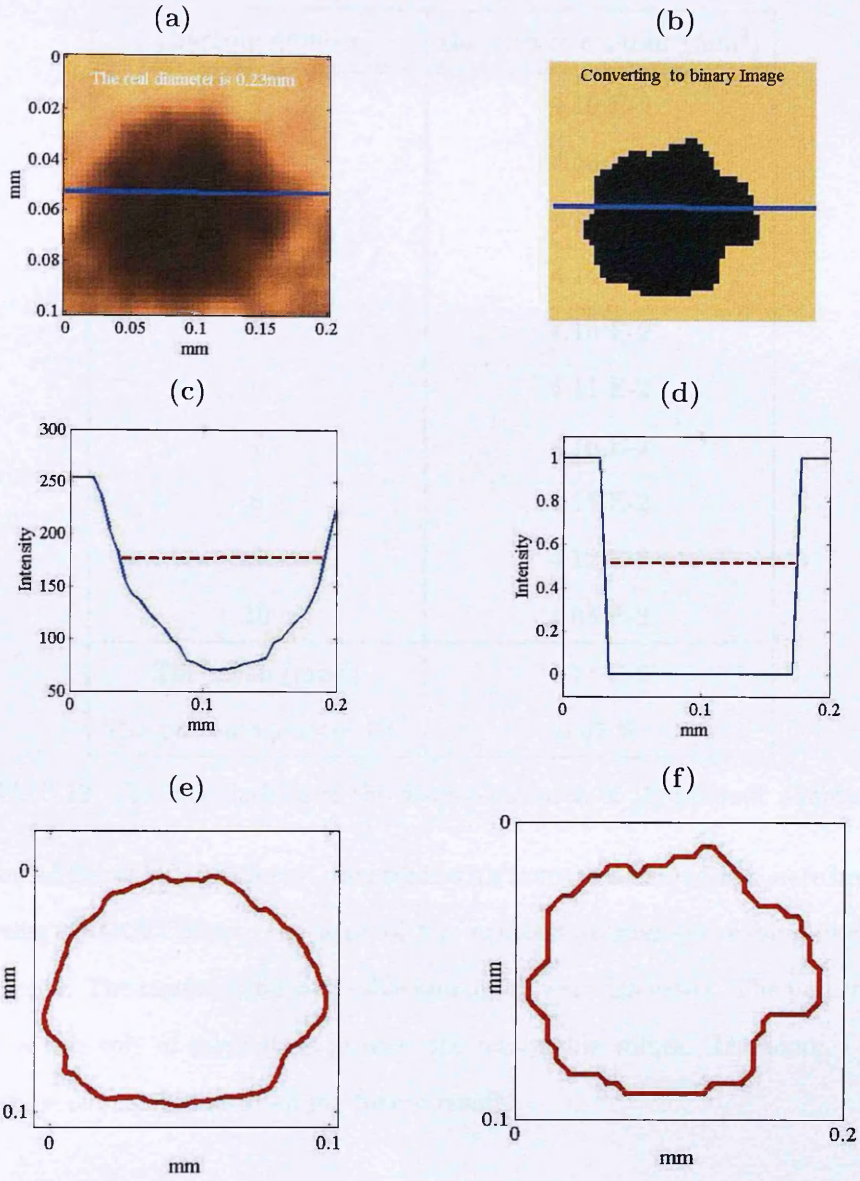

Figure 3.16: Calculating the area of the contour: (a) and (b) the image of the fishing-line and its conversion to the binary image, (c) and (d) comparison between the profile image of the same fishing-line before and after converting to the binary image, (e) and (f) the shape of contours for both cases.

nearly accurate result of the measurement.

In summary, the way of calculating the area of contour was explained in this

phantom number	the area of contour (mm^2)
1	4.10 E-2
2	4.16 E-2
3	4.15 E-2
4	4.14 E-2
5	4.15 E-2
6	4.11 E-2
7	4.16 E-2
8	4.15 E-2
9	4.12 E-2
10	4.08 E-2
The mean (mm^2)	4.13 E-2
The percentage error (%)	0.67 %

Table 3.12: The calculations of the fishing-line area of 10 different phantoms

section. After that, 10 different phantoms with immersed fishing-line were imaged by using SROCT. Then, the area of the contour around the fishing-line was calculated. The results in term of table and figure were discussed. The percentage error of this way of calculation provide the reasonable values. Therefore, I used this steps of calculation in all my future results.

3.4.6 Instrumental noise for a sequence of images

Finding out the instrumental noise level is an essential tool for this research to distinguish the oscillation of the chosen subject from other combined oscillations. In this section, three different phantoms were created as has been described in the section of the phantom's construction at section (3.2), page 43. One of theses phantoms was with immersed one fishing-line. The second one was with was with 4 stretched fishing-lines to get different cross sectional area. The last phantom with created several air bubbles inside it. After created the phantoms, the exper-

iment was setup as explained on the section (3.3), page 46. Each phantom was placed on a static table and the images were recorded for 10 minutes. All data were saved into SROCT memory for future processing and analyzing.

In order to identify the instrumental noise level for this technique, the areas of all created subjects into the three phantoms were calculated by following all previous calculation methods. Then, the calculating area in mm^2 were plotted as a function of time in seconds to explore any changing of the values by the time and to draw firm conclusions about the level of the noise level that may occur using the SROCT system.

3.4.6.1 Data processing and results

1- Fishing-line in stable phantom

In this case, the area of the contour of simulated vessels was calculated for all sequence images. Then, they were plotted as a function of time to clearly show any fluctuation of these values that may have occurred by using the selected routine.

Using the algorithm described in Appendix A-8 and from the figure (3.16), several important facts can be identified:

- The area of the contour for the simulated vessel changes with time within the range of the real area of the fishing-line, which is about $1.28\times\ 10^{-2}$ mm^2.
- The Root Mean Square (R.M.S.) of the fluctuation is calculated to give a sense for the typical value of the areas. In this case, it was about 1.182×10^{-2} mm^2. This result provides a slight discrepancy between the area measured and the real value which may reach up to 7 % or $\pm$ 0.098×10^{-2} mm^2.

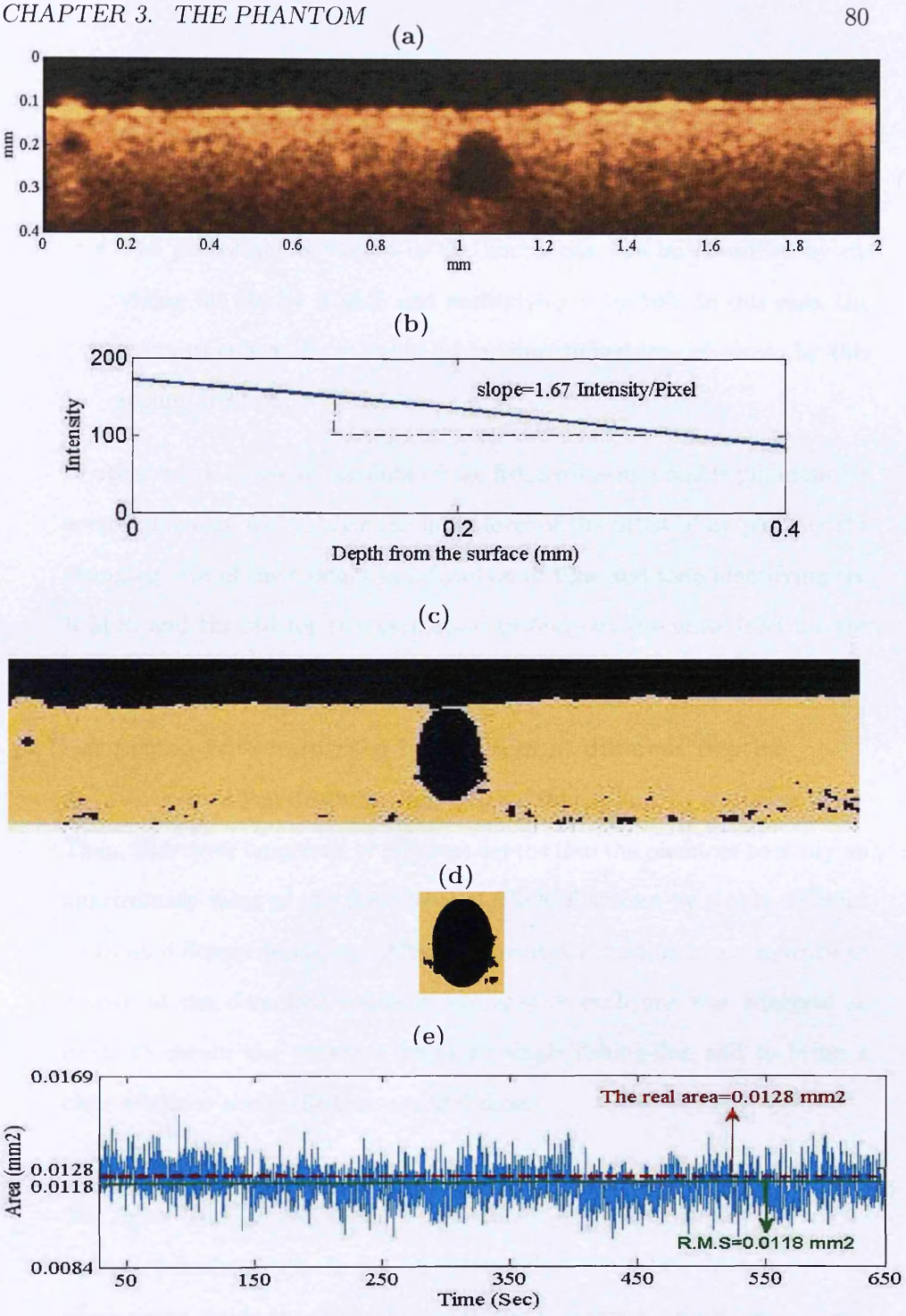

Figure 3.17: Fish line oscillation in a stable phantom: (a) the image of the fishing-line into the phantom, (b) the slope of changing intensity by depth, (c) the binary image after applying the correction factor, (d) cropped image around the mimicking vessel, and (e) the plot of the area of the contour by the time.

- The standard deviation (std) of this fluctuation will be presented as the instrumental noise level. We calculated its value from the results obtained in this experiment and it was 4.25×10^{-4} mm^2.
- The percentage deviation of the fluctuation can be identified by dividing the std by R.M.S. and multiplying it by 100. In this case, the fluctuation level for a stable fishing-line dipped into phantom by this regime is 3.6 %.

In other word, by recording data of the fishing-line in a stable phantom for several minutes, we evaluate the noise level of the SROCT by plotting the changing area of the contour as a function of time and then identifying the R.M.S. and the std for this oscillation to find out the noise level for the system and which was 3.6 % in this case.

2- Four fishing-lines immersed in phantom at different depths

Here we created four dissimilar diameters of fishing-lines by starching them. Then, they were immersed at different depths into the phantom to study an approximate value of the noise level of SROCT system by stable different areas at different positions. After 10 minutes recording of a sequence of images of the described subjects, the area of each one was analyzed in order to obtain the variation for every single fishing-line and to bring a clear evidence about the instrumental noise.

The figure (3.17) shows at the top (a) the image of the phantom with four immersed fishing-lines. It can be noticed that the fishing-lines appear as black shape inside the phantom due to the absorption properties of them. In addition, there is a bright shadow under each fishing-line which may be an instrumental artifact or could be due to the refraction of the light from the lower side of the subjects. The second line of the figure (b) presents the curve of changing intensity with depth and the value of the slope in order

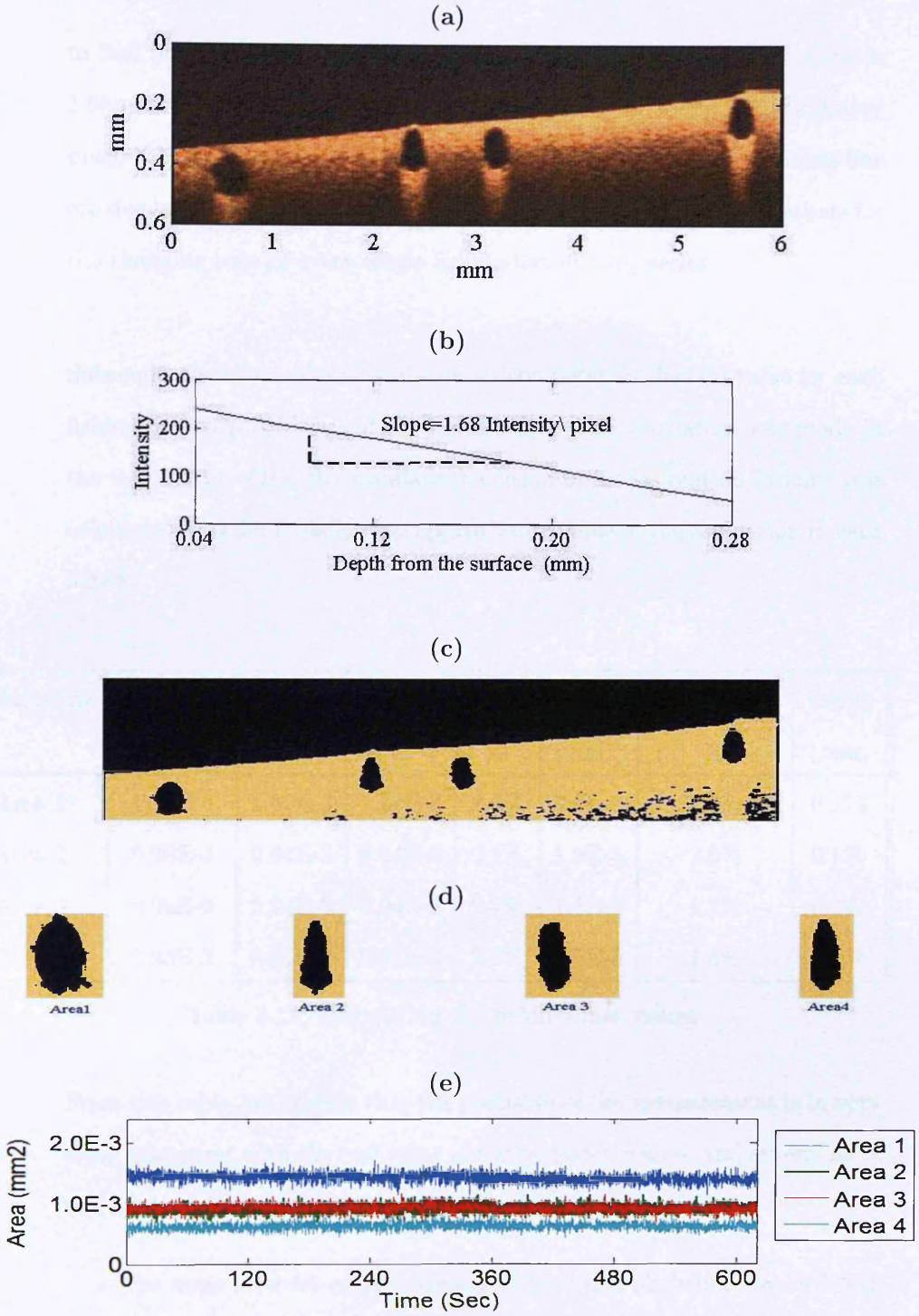

Figure 3.18: Several fishing-lines immersed into phantom: (a) the image of 4 immersed fishing-lines into the phantom, (b) the slope of changing intensity with depth, (c) and (d) the binary image for the full image and the cropped images for every single fishing-line, and (e) the oscillation of contours fishing-lines by the time

to find out the correction factor for the images. In this case, the slope is 1.68 intensity per single pixel depth. Below that, at (c)and (d) the binary image for the full image and the cropped images for every single fishing-line are displayed. In the last line of the figure (e) are shown the oscillations for the changing area of every single fishing-line as time series.

Subsequently, the mathematical comparison between the real value for each fishing-line with R.M.S. and the mean value of its oscillation was made in the table (3.1). Also, the standard deviation of its fluctuation in mm^2 was calculated in order to define the approximate value of the oscillation in each depth.

Fishing-line	Real area (mm^2)	R.M.S. (mm^2)	Mean (mm^2)	Error %	std (mm^2)	Fluctuation %	Depth (mm)
Area 1	1.29E-3	1.32E-3	1.32E-3	2.3%	2.6E-5	2.0%	0.174
Area 2	0.96E-3	0.94E-3	0.94E-3	2.1%	1.9E-5	2.0%	0.170
Area 3	0.96E-3	0.94E-3	0.94E-3	2.1%	1.7E-5	1.7%	0.141
Area 4	0.93E-3	0.91E-3	0.91E-3	2.2%	1.5E-5	1.6%	0.156

Table 3.13: Calculating the fishing-lines values

From this table, we can see that the precision of the measurement is in very close agreement with the real value of the fishing-line area, and several facts can be deduced in this case:

- The noise level for every fishing-line fluctuates slightly between 1.6 % to 2 %. This range of values could be related to difference of fishing-line area and depth.
- It can be seen that area 4 is the closest one to the surface and it provides lowest values of fluctuations value compared to the others.

On other hand, the area 1 is the deepest one from the surface and it has the highest fluctuation.

- Also, it can be noticed that area 2 and area 3 have the same area in mm^2, however, the fluctuation value of area 2 is bigger than the fluctuation of area 3. This result is due to the different depth into the phantom. This point leads to the fact that the fluctuation of the subject increases with the depth.
- By comparing area 1 and area 2, it can be figured out that area 1 and area 2 are almost under the same depth in the phantom. Although, the fluctuation of area 1 is more that the fluctuation of area 3 due to the different areas. At this point, the conclusion is the oscillation increases with increasing area.

In short, different fishing-lines were tested when immersed into the phantom and recording a sequence of frame images for several minutes to identify the noise level of the instrument. The results indicated that there is minimal noise level from SROCT images, which is about 1.6 % to 2 % in this case. These changes of fluctuation are clearly increased by increasing the depth and the area of the studied subject.

3- Phantom with bubble voids

As the vessels are displaced under skin in an unorganized way, and their positions under the skin are not kept constant due to the natural movements, we aimed in this part to simulate a slightly the vessels to get a clear conclusion about this level of the noise by creating several bubbles into the phantom. The recorded data was examined by going through all the earlier steps to classify the noise level, figure (3.18) demonstrates the sequence in this procedure.

The image of several bubbles distributed into the phantom along the width

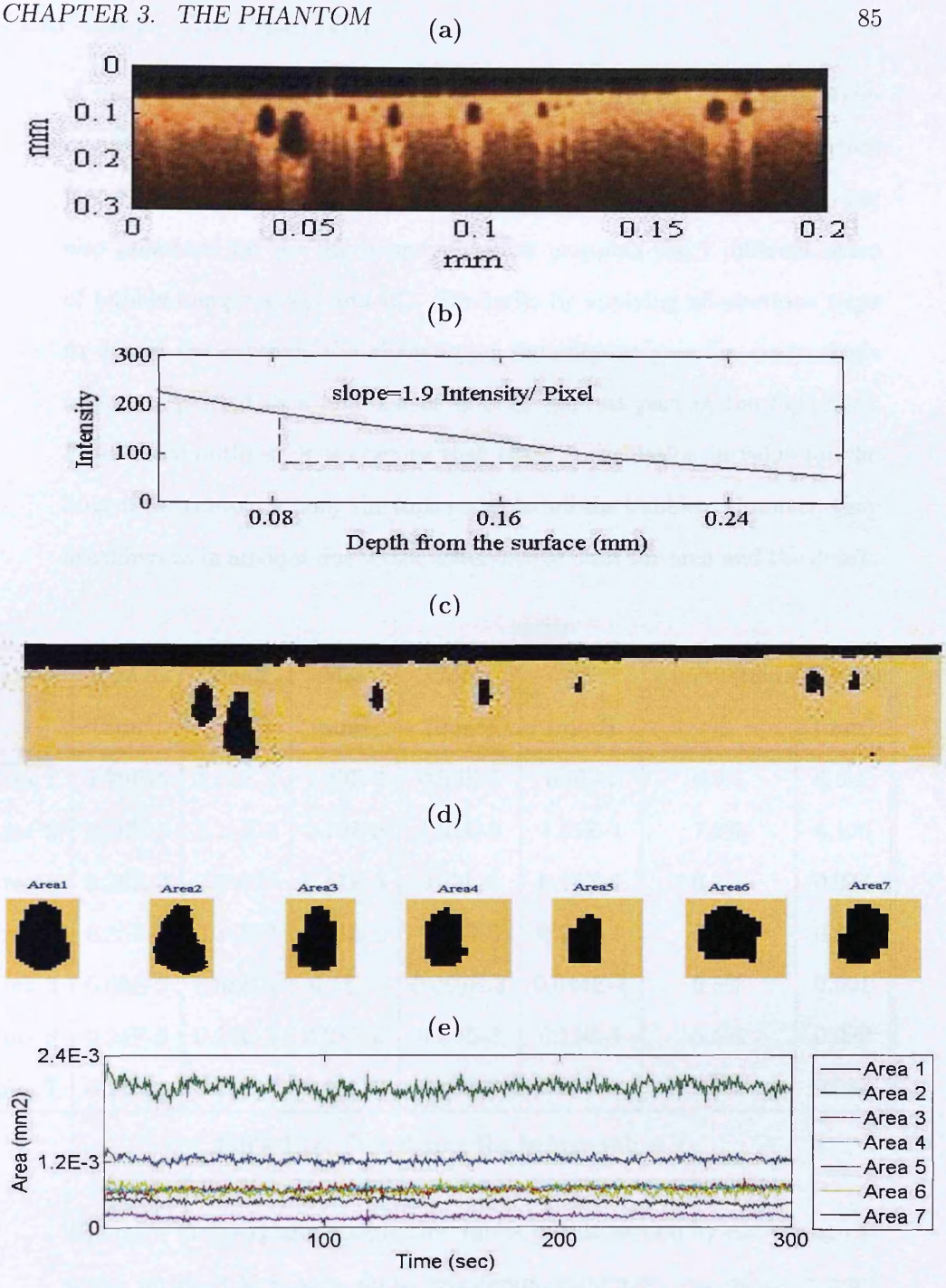

Figure 3.19: (a) The image of several bubbles inside the phantom, (b) the slope of changing intensity by depth, (c) the binary image after applying the correction factor to the image, (d) cropped 7 images of bubbles, (f) fluctuations of contours of 7 bubbles in the phantom

of the window is presented at the top of figure (3.18) (a). The second element in the figure (b) shows the curve that is made to identify the correction factor, which is found in this case to be about 1.9. The binary images are also presented for the full image and after cropping the 7 different areas of bubble images at (c) and (d). Similarly, by applying all previous steps to detect the contour, the changing of the contour area for every single bubble is plotted as a function of time in the last part of the figure (e). From these outlines, it is obvious that there is oscillation in value for the area of the contour among the time series for all the bubbles. However, they are different in amount due to the difference of both the area and the depth.

Bubble	R.M.S. (mm^2)	Mean (mm^2)	Max (mm^2)	Min (mm^2)	std (mm^2)	Fluctuation %	Depth (mm)
Area 1	1.29E-3	1.28E-3	1.49E-3	0.90E-3	0.9E-4	6.9%	0.087
Area 2	2.16E-3	2.15E-3	2.70E-3	1.65E-3	1.55E-4	7.2%	0.136
Area 3	0.26E-3	0.25E-3	0.41E-3	0.29E-3	0.16E-4	6.2%	0.073
Area 4	0.35E-3	0.34E-3	0.51E-3	0.28E-3	0.21E-4	6.1%	0.068
Area 5	0.08E-3	0.08E-3	0.1E-3	0.069E-3	0.044E-4	5.5%	0.061
Area 6	0.24E-3	0.24E-3	0.28E-3	0.20E-3	0.13E-4	5.4%	0.080
Area 7	0.11E-3	0.11E-3	0.13E-3	0.09E-3	0.65E-4	5.9%	0.059

Table 3.14: Calculating the bubble values

The table (3.2) explains clearly the results in this section by displaying the values of the R.M.S. area, mean, maximum, minimum, std values in mm^2 and the oscillation for every bubble which is presented as the noise level as a percentage. It can be noticed from the table that:

- The fluctuation of the fishing-lines is slightly less than the oscillation of the bubbles due to the stability of the fishing-line and the lack of control of the bubbles over a period of a few minutes. In detail, it

can be seen from table (3.2) that the minimum fluctuation for several bubbles inside the phantom is 5.4 %, which is more than the maximum value of the fluctuation for several fishing-lines, which is up to 2 %.

- The different absolute areas and the different positions in depth of the bubbles in the phantom give a fluctuation of values for the fluctuation that may be lower or higher than each other for the nearly similar areas. On other hand, there could be nearly the same oscillation for different areas due to the different depth.
- The table highlights every bubble fluctuation and it can be seen that the range of the oscillation is between 5.4 % and 7.2 %. This range provide information about the range of the noise level, which can guide any future data analysis by the chosen technique.

In conclusion, the fluctuation of several bubbles in the same phantom was calculated to determine the instrumental noise level and we found that this fluctuation varies minimally from one to another depending on the depth and the area of the bubble. However, it provides a suitable range for the noise level which will help for all future analysis.

To conclude all previous cases for identifying the noise level, we studied carefully the fishing-line in stable phantom, several fishing-lines in different depth and area, and several bubbles inside the phantom. We can highlight that there is a small percentage instrument noise level which may reach up to 7.2% in some cases. In addition, the fluctuations are slightly increased due to some facts such as increasing the area, increasing the depth and instability of the subject. These facts should be accounted for in all future experiments on human skin and will be definitely present in all the results that will be obtained.

3.4.7 Three dimensional images (3D)

In this part, we aimed to visualize the three dimensional images (3D) of the phantom, which is the best way to explain easily what is really seen by the system and what is the structure of the subject. The 3D images provide a good aspect of viewing for the subject to help understand in detail its layers and their locations in the phantom. As it was explained before, recording data by using the SROCT provides the 2D images which can be displayed in X and Y dimension. The X represents the width and the Y represents the depth of the subject. In addition, the Z direction can be obtained by moving a camera on the phantom for several millimeters. Then by using ImageJ computer program for a set of recorded 2D images, a 3D model of the original sample was reconstructed to build a picture of the 3D phantom image [Appendix B].

First, two different subjects are immersed into the Intralipid with gelatin; one with the fishing-line and another with serval small tubes. After that, the camera of the system was fixed on the phantoms. Then, the imaging recording was started. As the same time, the camera on the phantom was moved constantly with speed of 40 μm per second for 2 mm in Z direction for several millimeters by using an automatic mechanical technique. Finally, the two dimensional (2D) sequences images was reconstruct in order to obtain the 3D images for both cases.

As shown in the figure (3.19) the 3D images of the phantom were defined and the outlines of both the tubes and the fishing-line were easily visible in both cases. These images indicate an overview of how future measurement on human skin will presumably be made and how the cross sectional images of the layers are different depending on the position of the subject under the camera of the imaging system.

As has been said, all previous figures in this section bring a clear visualization of any features lying inside the phantom in three dimension. These results will

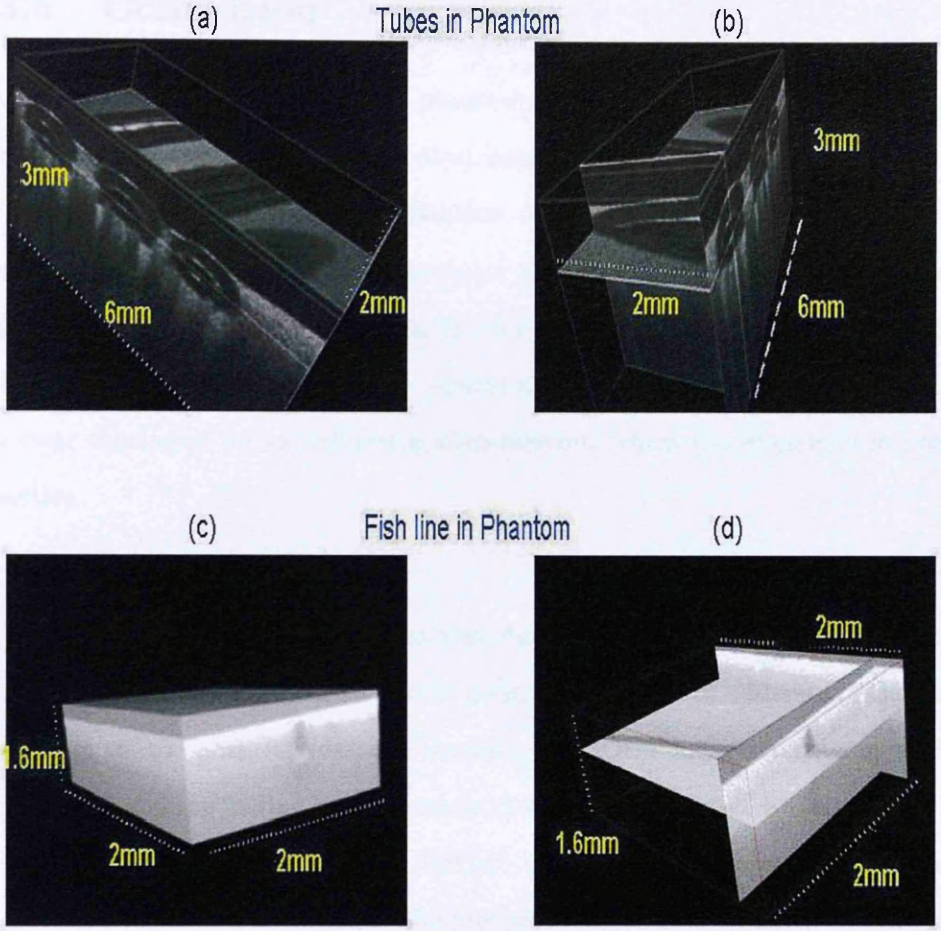

Figure 3.20: (A cross-sectional view of three-dimensional images of several immersed tubes obtained by SROCT; (c), (d) a cross-sectional view of three-dimensional images of fishing-line obtained by SROCT.

provide a good visualization for any future measurement on human skin, and will help by providing good evidence from the cross sectional images for human skin.

3.5 Conclusion

On the whole, a tissue-mimicking phantom is an essential tool for performance testing and optimization of the medical imaging system without the necessity of in vivo scanning. Therefore, the phantom of human skin and its measurements were explained in this chapter to evaluate the SROCT system and to definitely provide the right steps for analyzing any future data on human skin. The results on the phantom in the form of the figures and tables were presented to provide a clear conclusion for experimental measurement, which was explained in every section.

- First, several phantom images were displayed with different immersed subjects to simulate different vessels under human skin to understand the output of the images. Next, the accuracy of SROCT measurement was evaluated and the finding showed clearly that all measurements by using SROCT images and data analysis by MatLab image processing provide a high precession, with a deviation of the precession which is always less then 2 %.

- Subsequently, studying the intensity of images was explained and the results indicated that the intensity of the pixels in the image steadily decreased with depth, which guided us to calculate a correction factor for the images to normalize all pixels in intensity and verify any mathematical function applying to different depths. Meanwhile, the intensity changes of the image with depth was studied to identify the correction factor of the images. However, the results indicated that there is no general correction number and it is varied from 1.6 to 2.1 intensity per single pixel in depth. Therefore, we conclude that the correction equation has to be applied separately to each created image for every experiment before starting any calculation.

- Next, the description of the profile images was highlighted to identify the contour function of the simulated vessel. Moreover, the method of calcu-

lating the area of the contour was identified, by converting the corrected intensity images to the binary images and then summing all zeros pixels into a cropped image.

- Furthermore, investigation the SROCT noise level was defined by recording sequentially a series of frame images for several minutes on the different stable subjects such as: fishing-line in stable phantom, several different fishing-lines in the phantom at different depths, and several bubbles in the phantom. Those different subjects were used to trace the oscillation level of the instrument and to draw a definite conclusion about the noise level. The findings clearly show that there is normally oscillation for the stable phantom which at the maximum reaches 2.0 % in the case of immersed fishing-lines and 7.2 % in the case of introduced bubbles. The value of these percentages of the instrumental noise level depends on area, depth and stability of the phantom.

- Finally, several three dimensional images for the phantom layers were obtained, providing a clear visualization for any lying features inside the subject and which will draw a nice view of any cross sectional images on human skin.

In simple terms, the phantom was studied carefully in details to evaluate the SROCT images system and to build undoubtedly the way of the measurements and the steps of the calculations on human skin.

Chapter 4

Measurements on human skin

4.1 Introduction

Human skin is a unique engineered organ that has a complex tissue system which is built up from several thin layers. As we have seen in chapter 1 these layers are enormously well supplied with blood vessels; they are pervaded with masses of arteries, veins, and capillaries. Visualizing the important systems inside these layers and detecting blood vessel function *in vivo* is one of the fundamental aims in this research.

The figure (4.1) presents generally the blood vessel distribution under skin in the human forearm. The distribution of theses vessels are different from person to another; however, they are generally started laying at the surface of the dermis from the range between 0.01 mm to 0.1 mm.

In this research, Spectral Radar Optical Coherence Tomography (SROCT) was used as a technical instrument for all measurements. The general selection is made relying on the fact that it does not require any invasive procedures or exogenous contrast agents that may perturb the intrinsic physiology of the microcirculation. Also, it provides a suitable depth resolution to achieve this research aim.

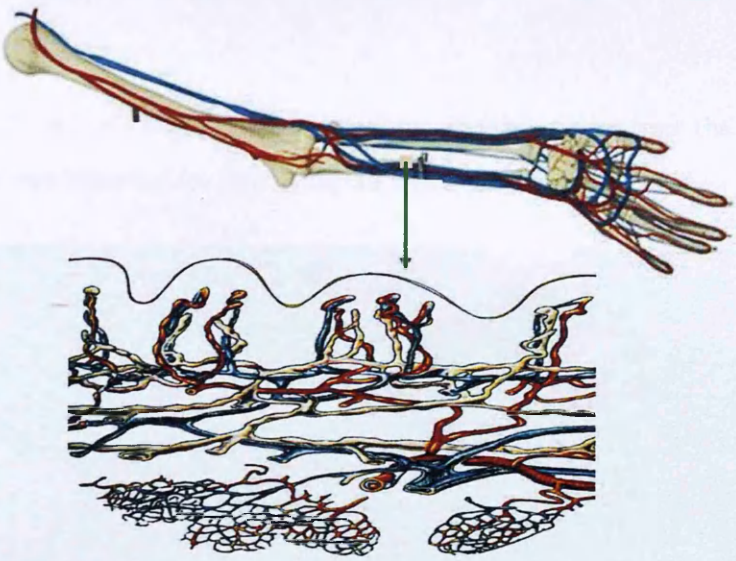

Figure 4.1: The diagram of Vessels distribution in human arm [76]

4.2 Experimental set-up

In this study the implications of the real time oscillation of blood vessels under human skin *in vivo* by using the non-invasive SROCT imaging system was explored. Several human skin images were preformed at the laboratory of the Physics department to detect the blood vessels and to visualize their function *in vivo*. The following steps were made at each experiment:

1. The subject set on the chair and its arm was placed on a stable fixing arm to minimize any movements and to give comfort to the arm to manage being static for several minutes as shown in the figure (4.2).

2. The camera was slightly moved on the skin to figure out the best position for observation of the vessels which can be identified easily from displayed images on the system screen.

3. The camera was fixed over the selected area by a stable holder.

4. In the case of investigating the single image, the data was recorded for few seconds.

5. In the case of studying the information into the images over the time, the data was recorded for more than 10 minutes.

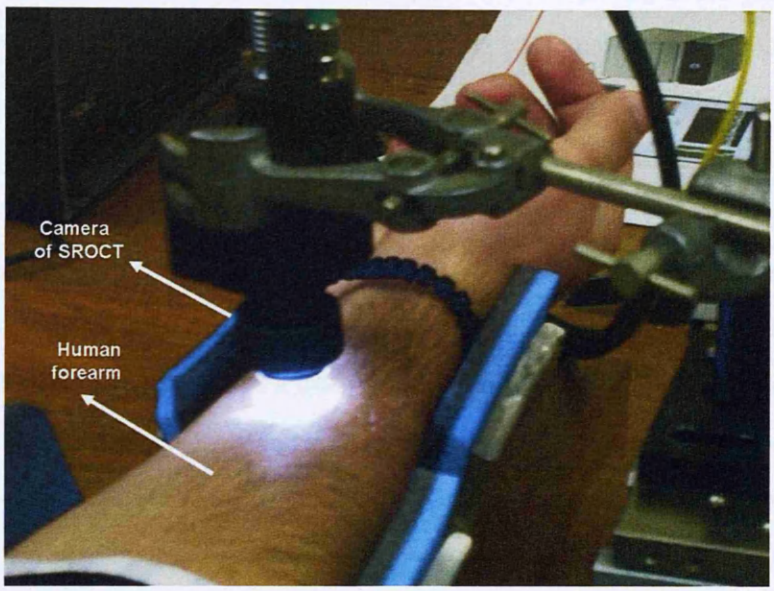

Figure 4.2: Human arm placed into a hand holder and imaged by a stabilized camera.

4.3 Data Recording and results

In this chapter most of the results in the form of figures and tables on human skin will be presented. In the first section in this chapter, several images at different places on human arm will be displayed to evaluate what the best area that may provide the best quality of the images is. After that, the selected area for all future experimental images will be identified and then several videos of blood vessel motions will be created at speeds of 1 - 8 frames per second to detect with certainty the vessel oscillation in real time as a movie. At the same time, the changes of distinguished vessels will be presented by creating a montage

for several of the sequence images, and then following these changes in size and position with time will be shown in this chapter to provide a proof about this investigation. In this chapter as well, the changing of the intensity with depth is going to be studied and the correction factor for recording image data will be investigated by following the same steps as for the phantom measurements. Then, to classify the method of the measurements on human skin, the comparison between the results which are obtained from human skin with the results that are found by measuring the phantom will be considered . After that, the contour will be applied to detect the distinguished vessel after applying the correction factor to the images. Subsequently, the area of the contour will be worked out as in previous steps that were made in the case of the phantom, and then their values plotted in a sequence as a function of a time series will be presented in this chapter. Next, a comparison between the range of the variations of vasomotion with the instrumental noise level will be made graphically and mathematically relying on different analysis techniques such as Fourier and wavelet transform. Finally, the three-dimensional images for the human skin layers will be presented to provide information about the structure of the skin layers and to find out the position of the vessels.

4.3.1 First human skin images

This experiment is very important as the first stage in all measurements to discover the best area for seeing the vessels and then to unify of all future measurements. At this point, to select the best area for visualizing clearly the blood vessels, one person was imaged at six different places on the arm by following the previous experimental steps at section (4.2), page 93. These places are: the back of the arm, forearm, finger, hand dorsum, nail and thumb. Relying on the fact that the blood has the property of highly absorbing a light, the vessels will appear as black dots or lines in any obtained images depending on their positions.

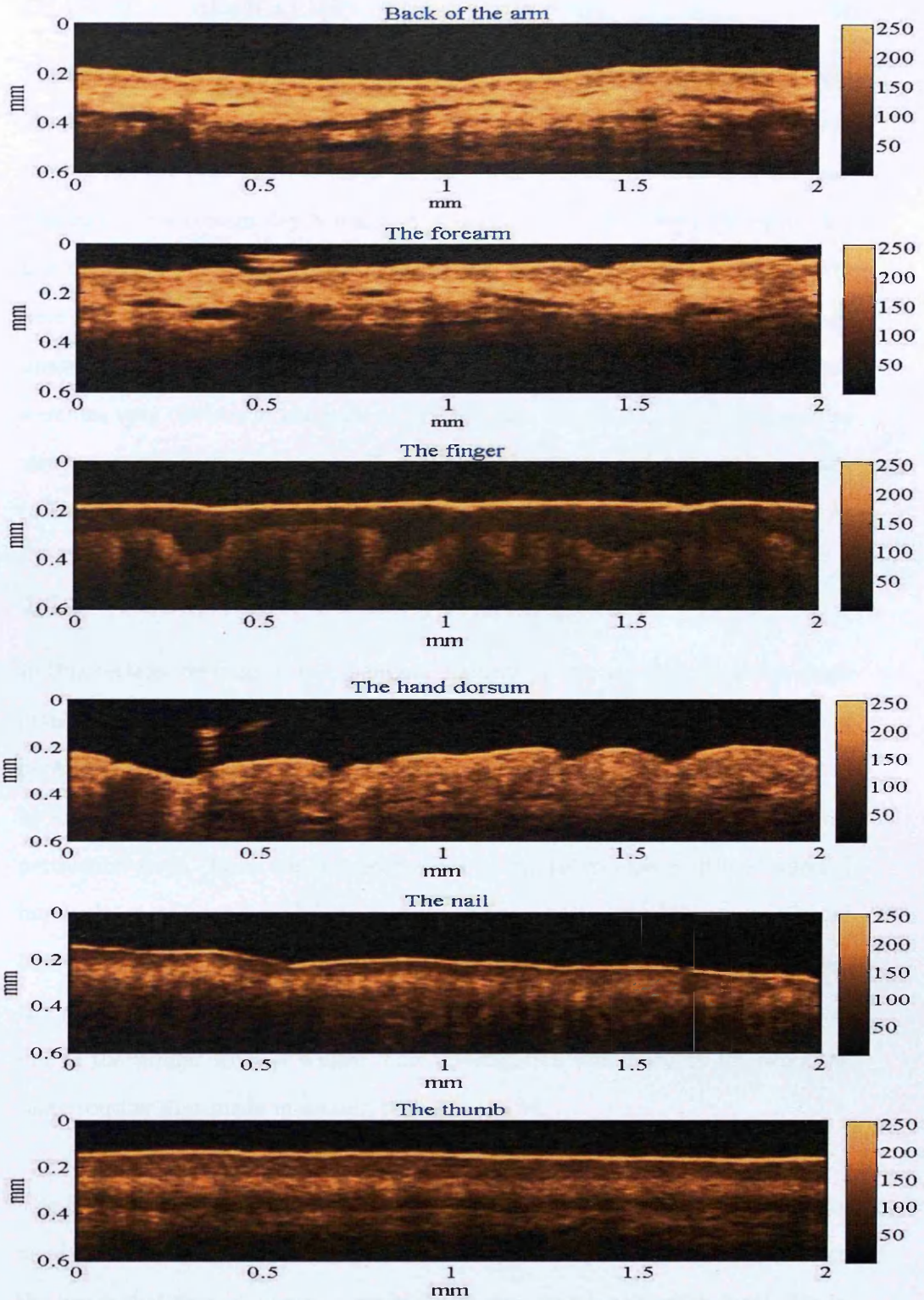

Figure 4.3: Different SROCT images of human skin with column intensity bars of the image pixels: it presents in order from the top the image of the back of the arm, the forearm, the finger, the hand dorsum, the nail and the thumb.

The figure (4.3) displays several images from the same subject at different selected places. As can be seen from the figure, it is very hard to identify the vessels in the thumb, the nail, and the finger because they contain very small vessels and capillaries at a certain depth which it is hardly possible to see at the provided instrumental resolution. However, at the hand dorsum, the vessels under the skin were seen as black dots and lines into the images. By comparing all these three images, it can be conclude that detecting the cross section area of the vessels were not very obvious at the back of the arm and the hand dorsum compared to the images of the forearm sides. Therefore, the forearm was always selected as a reference point for comparing all involved measurement.

4.3.2 Reduction of intensity with depth

In this section, we studied the changing intensity of the images with every single pixel in mm depth which has been obtained from the human skin as a function of depth within several micrometers. To form the conclusion in this step, I started by imaging the forearm of eight subjects for 1 second using the same previous experimental steps. Then, the intensity values of similar window widths at selected horizontal depth were studying carefully. Theses horizontal lines wear selected based on there is no any interrupted images' vessel into that depth. After that, the image was studied by plotting the pixel values for each selected horizontal line in the similar window width. This investigation was made by following the same routine that made in section (3.4.3), page 64.

The figure (3.12) presents an intensity as a function of depth within a small width window at the middle of the image from one of created phantoms. It is clear from the figure that there is always a gradual reduction in intensity with depth due to the scattering of the light by the phantom. This scattering reduces the ability of providing information by the depth and makes it hard to see any thing deeper than 0.4 mm from the surface. Moreover, it can be seen that there is a slight

fluctuation in intensity for the same image at same depth due to the different time of the scattering from different points at the same depth.

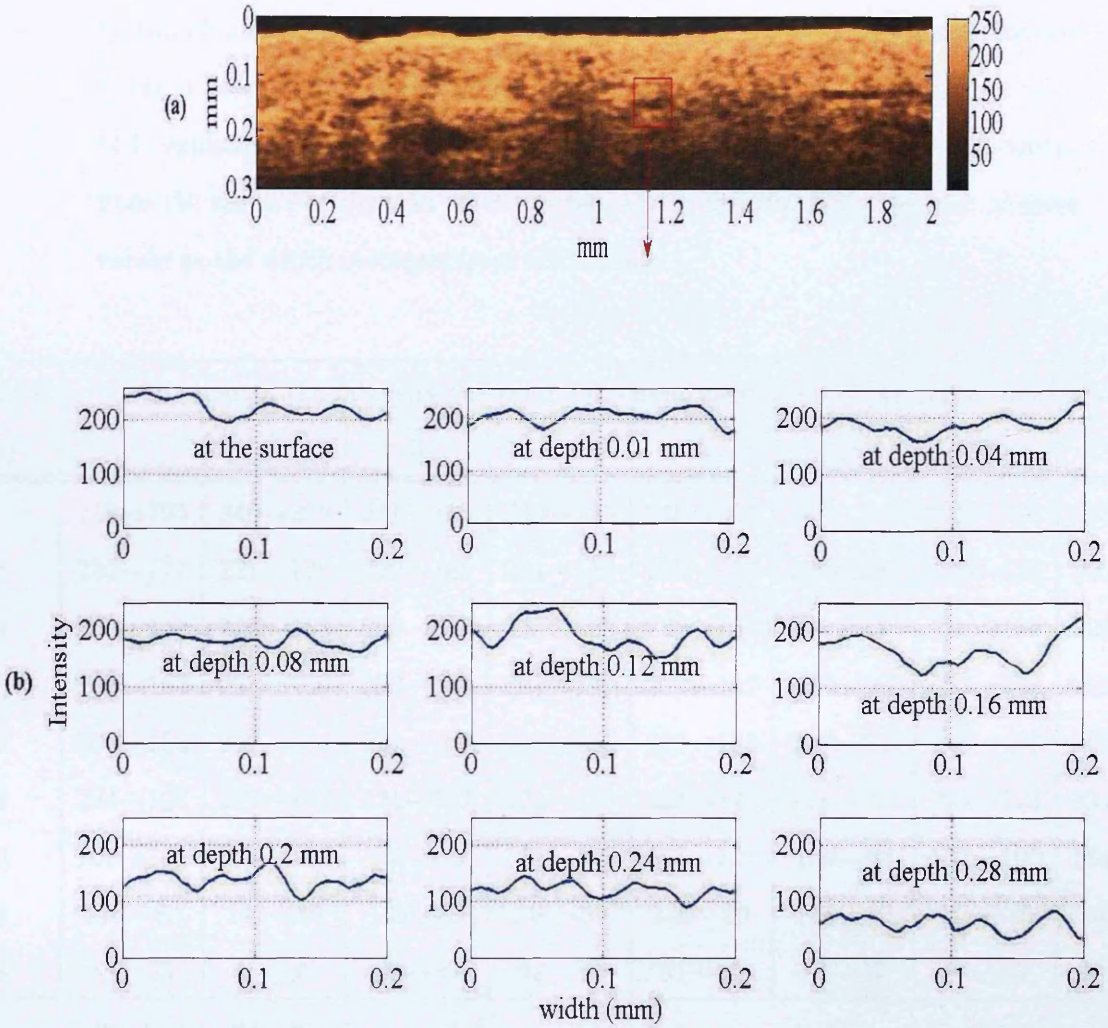

Figure 4.4: Changing intensity by depth for small width: (a) human skin image by SROCT, and (b) the intensity of the specific width at different depths into the image

The figure (4.4) presents one of the results from measured subjects. As can be seen, the intensities values are analyzed at different depths in the same image.

This particular study indicates that there is a clear fluctuation in intensity at the same depth; also, there is a gradual reduction in intensity by the depth for the same window image which is similar to the oscillation that has been identified by the phantom images in section (3.4.3), page 66. All these variations are due to the different values of scattering light from components under skin. The table (4.1) explains the range of these changes in the intensity values at several depths from the surface of the skin for 8 subjects and it presents the reduction of these values as the depth increases from the surface.

The depth	The range of the intensity values of 8 different participants (minimum→maximum)							
(mm)	1	2	3	4	5	6	7	8
0	248→195	240→200	241→185	239→195	240→201	248→195	242→191	253→198
0.01	225→171	221→170	222→169	224→174	223→176	225→171	230→176	220→169
0.04	220→158	226→158	220→158	220→150	220→158	215→158	220→158	220→158
0.08	202→162	208→160	202→162	202→159	202→162	198→162	202→162	202→162
0.12	200→153	200→154	201→153	202→150	203→153	200→153	208→153	205→153
0.16	224→128	229→129	221→127	224→130	224→120	224→123	224→124	224→123
0.20	167→102	168→102	167→99	161→102	167→101	169→99	167→100	164→102
0.24	146→89	147→89	146→89	146→89	146→89	146→89	146→89	146→89
0.28	82→33	80→36	86→39	82→37	81→35	82→37	84→33	82→35

Table 4.1: The fluctuation of the intensity at the same depth and its reduction with depth for 8 human subjects

The conclusion from these findings is that the intensity of skin images has unstable values for ever single pixel and these values are decreased on going down from the surface of the skin due to scattering properties of the light. These results provide a similar determination to what has been identified from the case of the phantom. For that reason, we attempted to proceed as in the earlier analysis by the phantom and which started by identifying the correction factor of the

intensity for images. This step will bring as far as possible a consistency on all forthcoming analysis and confidence to judge any comparison between the images from the human skin and from the phantom.

4.3.3 Calculating the correction factor

In this part, we studied the changing of intensity of the images by human skin at every single pixel within several micrometers depth to define the factor that will unify the intensity of images with the depth. By following the same steps that are made for the phantom to calculate the correction factor in section (3.4.4), page 68, the human skin will be tested. We started this point by analyzing the eight obtained images in previous section. Then, the intensity values and their changes on going deep from the surface for every case were studied by plotting the intensity value for a single column pixel as a function of its depth. After that, the slopes of the reduction lines were calculated for each subject and then comparison presented in the table (4.2).

Figure (4.5) shows the curve of changing the intensity values for the same pixel point by going deep from the surface for eight different subjects. It is clear that the intensity is generally decreased by going away from the surface in depth.

The table (4.2) shows the range of these slopes. They are graduated between 1.54 and 2.02 for intensity per pixel in depth. The standard deviation (std) in this case was 0.14 intensity per pixel and the mean value of these slopes is 1.78 which is nearly similar to what has been found out from previous experiments on the phantom.

This result leads to the same conclusion as previously, which is that there is no generally accurate number for the correction factor that can be confirmed as a

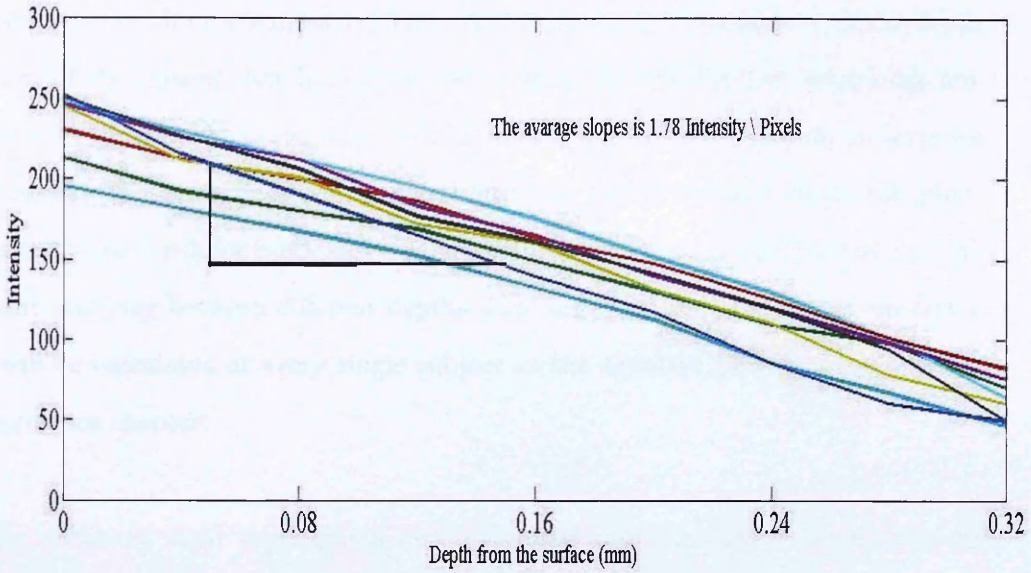

Figure 4.5: The reduction of the intensity by depth for 8 different participants

participant number	slope (intensity pixel)
1	1.75
2	2.02
3	1.80
4	1.90
5	1.54
6	1.68
7	1.79
8	1.81
The mean (intensity \ pixel)	1.78
The standard deviation (intensity \ pixel)	0.14

Table 4.2: The calculated slopes at the same width window position for 8 different participants with presented values of the mean and standard deviation of the slopes

standard in all future measurements. As the intensity is unstable with the depth for all the images that have been tested by using this routine, comparing any single points at the same image with different depth will not provide an accurate results. Therefore, we attempted to identify the factor that will steady the intensity by the depth for every single experiment. This step is an essential for making any studying between different depths with any certainty. Therefore, this factor will be calculated at every single subject as the equation (3.1) presented in the previous chapter.

In summary, eight participants were measured and their images were analyzed with the aim to calculate the correction factor of the intensity by depth. The conclusion that can be drawn in this case is similar to that obtained from the phantom, which is the variation in value of the slopes can not be determined generally as standard in all future measurement. Therefore, we endeavor to define this factor for every subject at every measurement by calculating its value from the general equation obtained.

4.3.4 Montage sequence images

Montage image is a technique that is performed on selected images by cutting and joining a number of sequence images. The composite figure presents multiple image frames as a rectangular figure to allow any small differences between the selected images to be visualized. At this point, we recorded several images in a time sequence for one participant over 10 minutes by following all explained experiment steps. Subsequently, the same window of the obtained images is cropped where the vessel is supposed to be located to visualize closely the vessel. Then, to detect the function of the vessel, a montage of sequence images in a time series is created by using MatLab images processing toolbox as has been described in Appendix A-8.

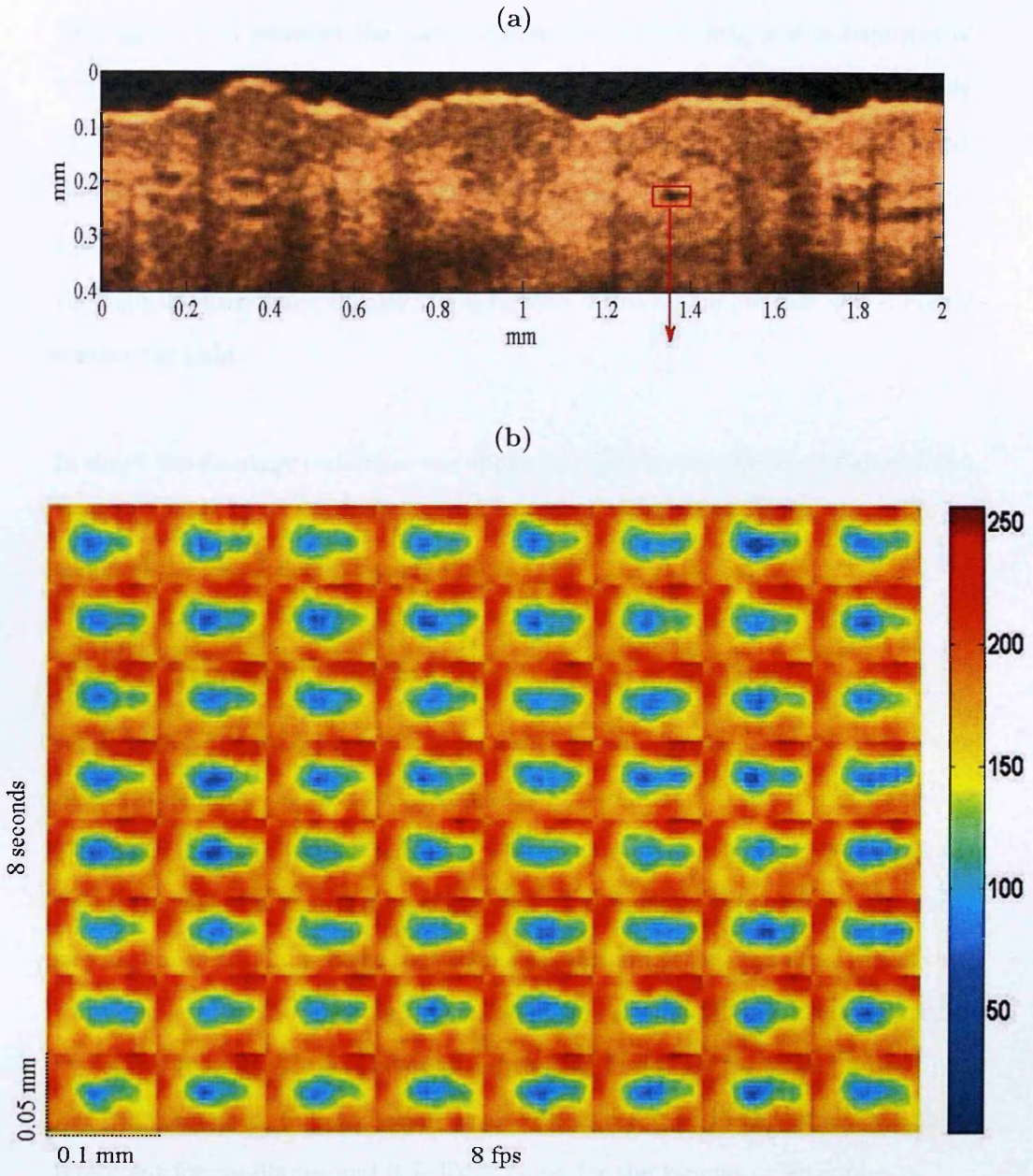

Figure 4.6: Detecting a small vessel from a sequence of recording images: (a) selected a vessel area from the human skin image, (b) a montage of sequence recorded images during 8 seconds.

The figure (4.6) presents the same window for several images in a sequence of 8 frames per second (8 fps) (the speed of data recording per second) by using SROCT. Every window has an area of 0.1 mm × 0.05 mm which displays closely the detected vessel under skin. The low intensity color in this figure represents the vessel area as the light is highly absorbed by the blood inside the vessel and the high intensity color display the skin with different components which highly scatter the light.

In short, the montage technique was applied to the sequence images from recorded data on human skin. The results shows clearly in the form of a figure the changing shape of the vessel due to vasomotion.

4.3.5 Contour of vessel

As detecting the oscillation of vessels under human skin is the main aim of this research, defining the contour of vessels is an essential function which guides us to achieve the main goal. First of all, a series of images in chronological sequence for human skin was recorded by using SROCT technique. From all recorded measurements, the finding shows that the smallest diameter of visualized vessel that can be imaged in sequence for fifteen minutes is around 28 μm. From indication by several researchers, the diameters of the capillaries are between 7.5 μm to 25 μm [73]; therefore, the oscillation of all vessels detected in this study are absolutely not for capillaries and it is likely to be for the venules or arterioles.

By following the same procedure for defining the contour as in the chapter on the phantom, the correction factor has been calculated for selected images. Then, the determined value is applied to all recorded images before they are cropped in equal size of 0.1 mm × 0.05 mm around the vessel location. After that, the contour function is applied to all cropped images using the calculations steps that was explained in section (3.4.5) by using MatLab Image processing toolbox. At

the final stage, a sequence of plotted contours from skin's recorded images are presented in the same figure to show distinctly any changes in shape of the vessel with time.

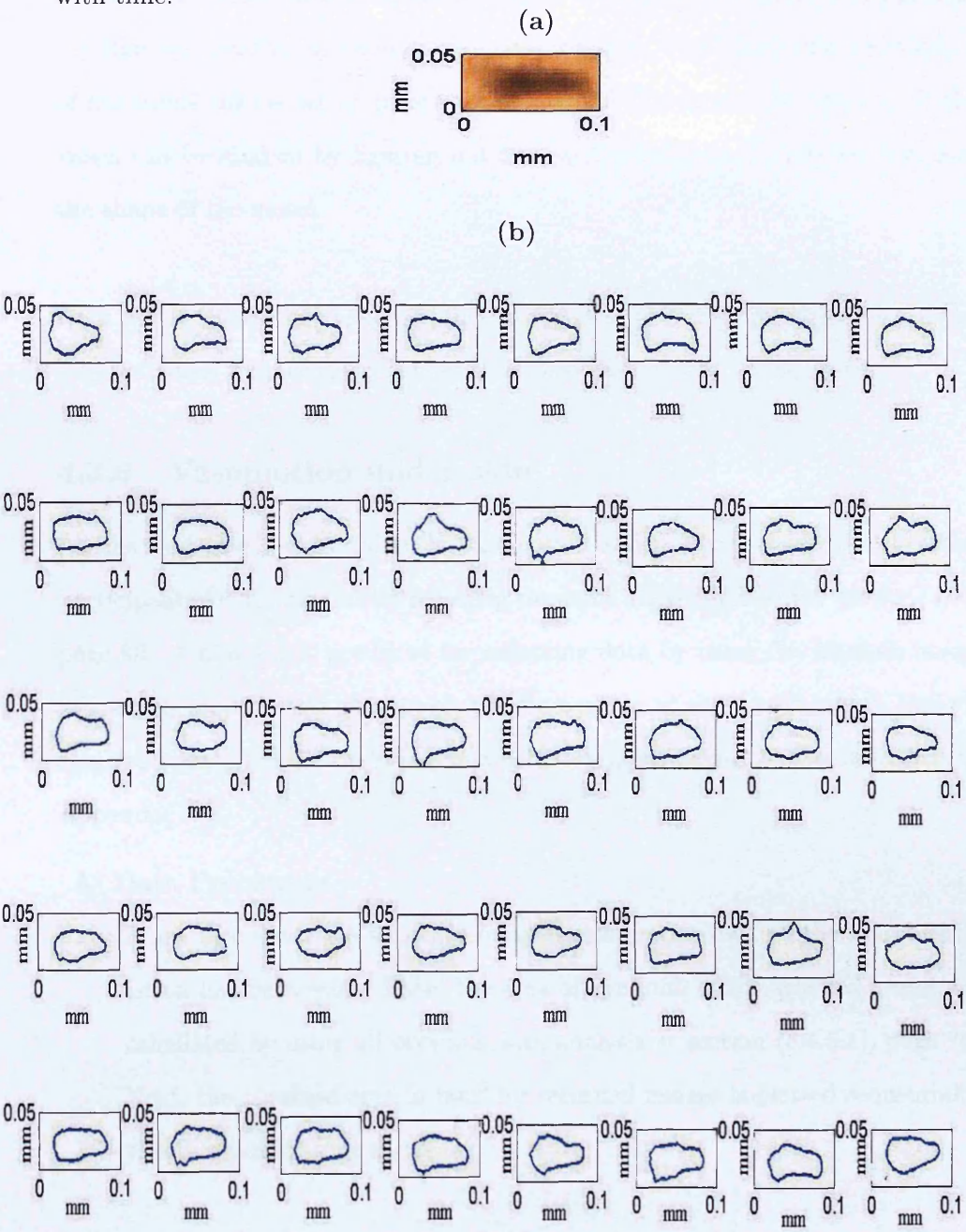

Figure 4.7: (a) The image of small vessel, (b) The contour of the vessel for a sequence 5 seconds recorded images

In the figure (4.7), the supposed vessel is displayed in a small window image area which is about 0.1 mm $\times$ 0.05 mm. In addition, in the same figure, the contour of the same window area in sequence images is shown as five rows, which present the time of recording in seconds, and eight columns, which represent the number of the frame that is set-up in one second. From this figure, the function of the vessel can be studied by figuring out the chronological changes of the size and the shape of the vessel.

Over all, it should be easily possible to judge in this part the functions of the selected vessel by studying changes of defined contours as a time series.

4.3.6 Vasomotion under skin

At this stage, we look to define the vasomotion under skin by imaging six healthy participants for 15 minutes by following the same steps described in section (4,2), page 93. A movie was produced for collecting data by using the MatLab image processing toolbox. At this stage, the fluctuation of the blood vessels was visualized clearly for the first time in various created movies as was described in Appendix A-9.

A- Data Processing

From all 6 data, the sequence images were cropped where the vessel oscillation has been seen. Then, the area of contours of the selected vessel are calculated by using all previous data analysis at section (3.4.5.1), page 75. Next, the obtained area in mm^2 for recorded images is plotted sequentially as a function of time series.

To be precise about all obtained results, the area of two vessels for one of the subject were plotted together as a function of time. At the same time, the Root Mean Square (R.M.S.) of the oscillation of the two vessels and for the vessels from the six participants were calculated. This numerical

quantity represents a measure of the area of the defined vessel. Moreover, the standard deviation (std) of this oscillation is calculated as well to present the level of the vessel variations.

B- Results

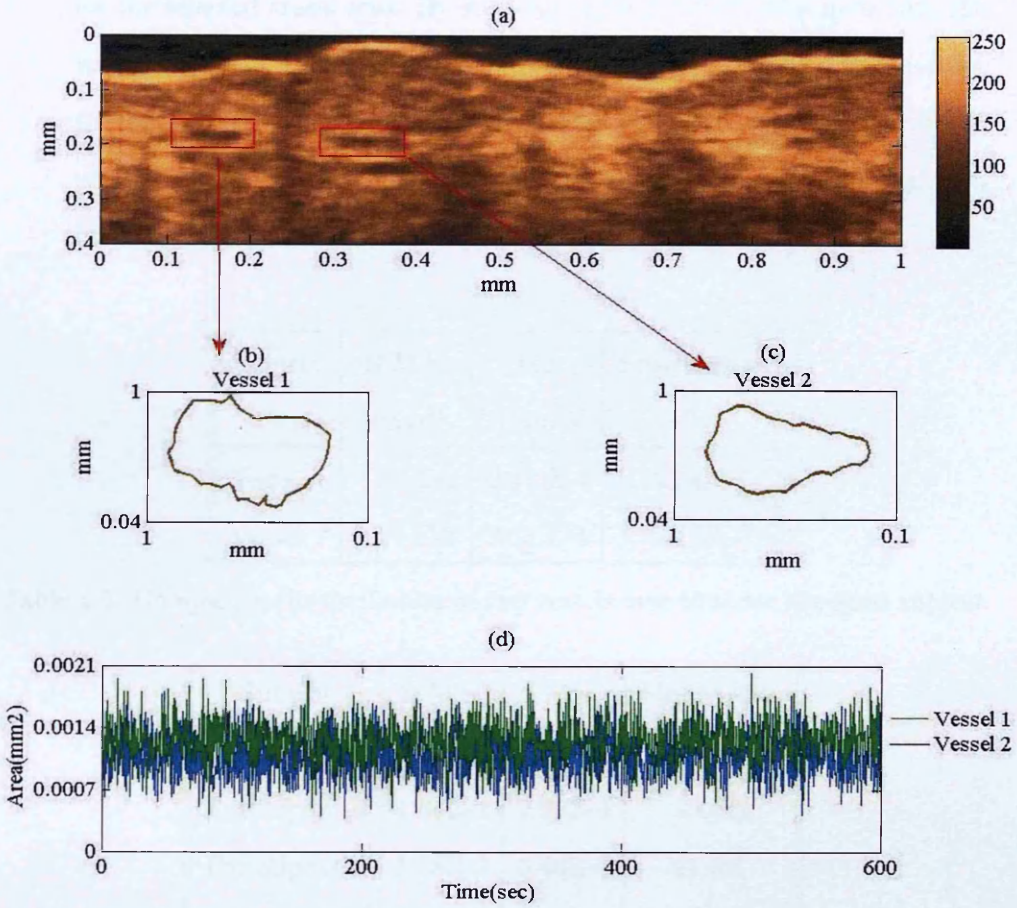

Figure 4.8: Comparing the oscillation of two selected vessels over time for the same subject: (a) the image of human skin by using SROCT with selected two different vessels, (b) the contour of the two selected vessels, and (c) the oscillation of the area of the two vessel over the time

The figure (4.8) (a) displays the image by SROCT of one of the subjects. The (4.8)(b) presents the contours of two different selected vessels. Then the last part of the figure shows the plots of cross section area of the two vessel as a function of time. This figure shows clearly the waving of the value for the selected vessel area. By studying defined information in details, the values of R.M.S. (mm^2), std (mm^2) and fluctuation (%) were calculated for the both vessels. It can be conclude from table (4.3) that both different vessels in terms of their locations under skin and their cross sectional area provide a nearly similar oscillation for the same subject.

Subject	R.M.S. (mm^2)	std (mm^2)	Fluctuation %
Vessel 1	1.09 E-3	2.34 E-4	21.4%
Vessel 2	1.36 E-3	2.65 E-4	20.5%

Table 4.3: Comparing the oscillation of two vessels over time for the same subject

Subject	R.M.S. (mm^2)	std (mm^2)	Fluctuation %
Participant 1	1.36E-3	2.78E-4	20.5%
Participant 2	1.58E-3	3.44E-4	21.8%
Participant 3	0.95E-3	2.09E-4	22.1%
Participant 4	1.12E-3	2.37E-4	23.7%
Participant 5	1.42E-3	2.81E-4	19.8%
Participant 6	0.89E-3	1.84E-4	20.7%

Table 4.4: Comparing the oscillation of 6 different participants

The vessels oscillations for the six subjects were similarly investigated and the results of one selected vessel for each case were presented in the table (4.4). It can be conclude that the oscillation of different subjects is slightly different which could be due to the different locations of the vessels under

skin or the diffident cross sectional areas of study.

4.3.6.1 Comparing the vessel oscillation with the noise level

Distinguishing the real oscillation of the vessel from the fluctuation of the instrumental noise is an important step to be certain about the reality of vessel oscillation. Therefore, finding out the relation between the defined vessel oscillation and the instrumental noise level was studied in this part.

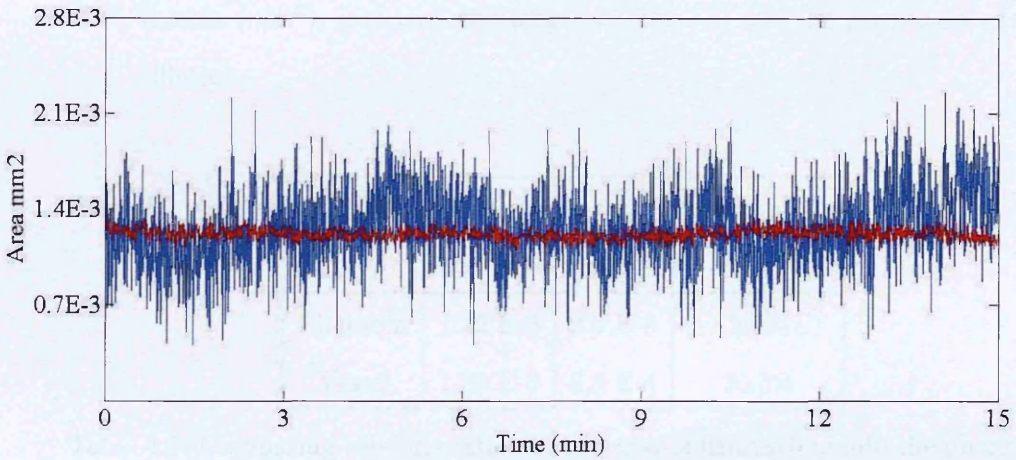

Figure 4.9: The fluctuation of the area of fishing-line into the phantom (red line) with the area of real vessel under human skin (blue line) at the same depth

1- Data Processing

As a consequence, the two similar previous measured areas of phantom in the section (3.4.6.1), page 83 and vessel in the section (4.3.6), page 107 were investigated in this particular case. The both selected cases were at almost same depth position which is at around 0.1 mm. By plotting the fluctuation of both areas as a function of time in the same figure, the difference of the range in both fluctuation can undoubtedly be recognized.

2- Results

From figure (4.9), it can be seen without doubt that the range of the oscillation of a selected vessel is more than the fluctuation of a mimicked vessel, which provides a clear indication of the reality of the observed vasomotion.

With attention to particulars, the following table shows a comparison between the two subjects that has been presented in the figure in terms of R.M.S. (mm^2), standard deviation (std) (mm^2) and the percentage of oscillation.

Subject	R.M.S. (mm^2)	std (mm^2)	Fluctuation %
Phantom	1.32 E-3	2.6 E-5	2.0%
Vessel	1.36 E-3	2.8 E-4	20.5%

Table 4.5: Comparing the fluctuation of the area of fishing-line into the phantom with the area of vessel under human skin

According to the table (4.2), it can be concluded that:

- The root mean square (R.M.S.) and the mean value of the both fluctuations is almost the same which builds a confidence for any comparison between any calculated values for both the human skin vessel and the phantom with the fishing-line.
- The range of the oscillation of the vessel is nine times as large as the range of the fluctuation of the phantom.
- The standard deviation (std) of the vessel fluctuation is about ten times as large as that calculated for the phantom.

- The percentage of oscillation by the vessel is ten times more than the percentage of fluctuation by the phantom.

From all previous comparison points, the oscillation of the vessel has evidently been discovered by graphical and mathematical comparisons between the fluctuation in similar areas of simulated vessel in phantom and in the blood vessel at the same depth. Beyond any doubt, it can be concluded that the defined variations from human subjects are related to the vasomotion under skin.

4.3.7 Fourier Transform for experimental data

As has been known that some of the signals are not periodic and could be random fluctuation, the need to define a technique to find the frequency content of an arbitrary function is motivated. According to this point, the Fourier transform technique has been used to detect oscillatory components in the measured signals in this chapter.

The Fourier transform is a mathematical operation that maps a time series into the series of frequencies. It disintegrates a function into its constituent frequency components and defines a relationship between a signal in the time domain and its representation in the frequency domain by decomposing any complex valued signal in a unique way of viewing as the sum of simple different frequencies, which are in time signals[77]. If the signal is complicated but periodic, it will be represented as the sum of several fundamental frequencies; otherwise, the output function will be as a noise signal see. The description of this function is at Appendix A-10-1.

4.3.7.1 Fourier transform for human data

In this work, an attempt was made to visualize the dynamics of the motion of blood vessels, based as several researchers have indicated, on the highly complex oscillatory patterns that have been seen in cardiovascular system (CVS) time

series. The oscillatory patterns of CVS comes from several different vascular and neurophysiological processes at different levels and on time scales of minutes manifest in six different oscillatory components [78]. The figure (4.10) shows the different oscillatory components that have been found, based on several studies [79].

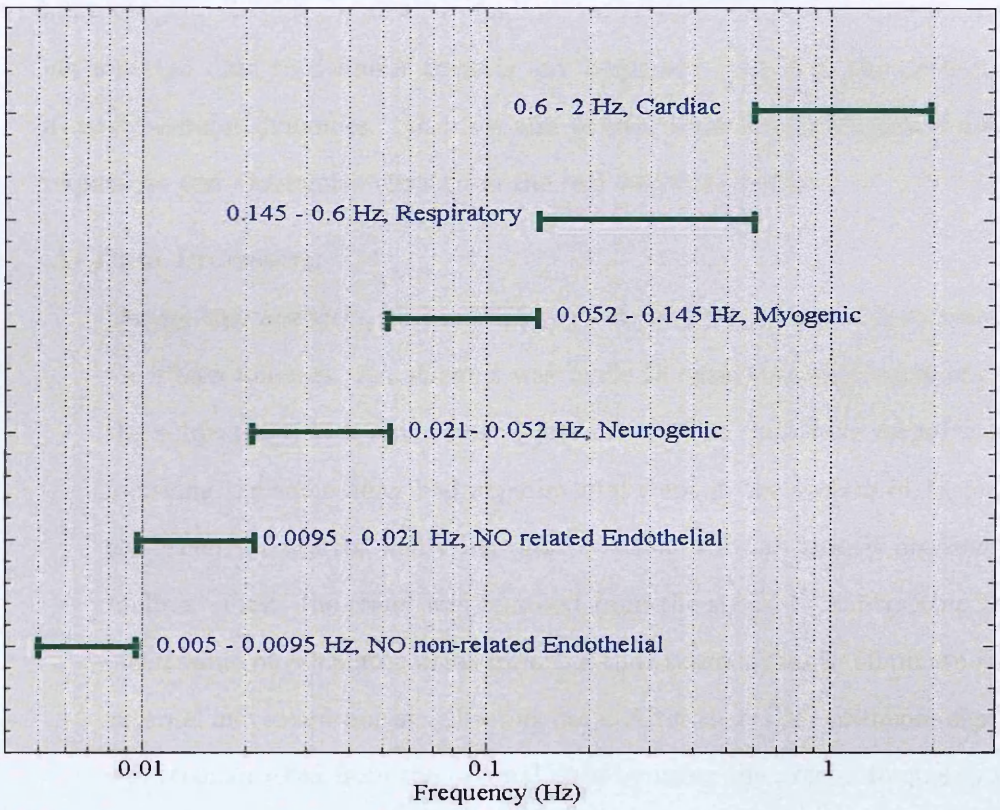

Figure 4.10: The frequency ranges of the main components of the cardiovascular oscillations [79]

As can be seen from the figure, there are six fundamental periodic constituents in cardiovascular system time series.

The characteristic frequencies of the oscillatory components are in the interval

between 0.0095 Hz and 2.0 Hz. The cardiac and respiratory oscillations have frequencies of between 1 and 0.2 Hz. Moreover, the low-frequency oscillations around 0.145 - 0.0095 Hz are involved in the intrinsic myogenic activity of vascular smooth muscle, the neurogenic activity of the vessel wall, and the mechanisms of vascular endothelial function. Furthermore, nitric oxide and endothelium-derived factors are hypothesized to be involved in the frequencies between 0.0095 and 0.021 Hz [80]. Relying on all these finding, we applied the Fourier transform to our collected data to define if there is any frequency related to the oscillators of cardiovascular dynamics. Also, we aim to determine the instrumental noise frequencies and distinguish them from the real vessel oscillation.

A- Data Processing

During this research, six participating subjects are measured semi-supine for fifteen minutes. An attempt was made to ensure resting conditions of the subject and lack any physical movement. The data were recorded by following the same described experimental steps in the section (4.2), page 93. Then, we started analyzing data by using MatLab images processing toolbox. First, the trend was removed from the signal by subtracting the mean value of calculated areas from the time series signal to eliminate any external movement during collecting data. After that, the continuous signal was reconstructed from the original data by using the precise frequency of recording data, which is 8 Hz, to dismiss any frequency noises. Finally, the Fourier transform function is applied to the computed area of all vessels as a function of time as described in details in Appendix A-10-2.

B- Results

The figure (4.11) shows Fourier transforms obtained from time series of cross sectional area obtained for six subjects. According to these figures and relying on comparison of spectral components in normal physiology, it can be noticed from all of these plots that there are between four to six peaks at each plot in the figure. By analyzing each plot in the figure, we

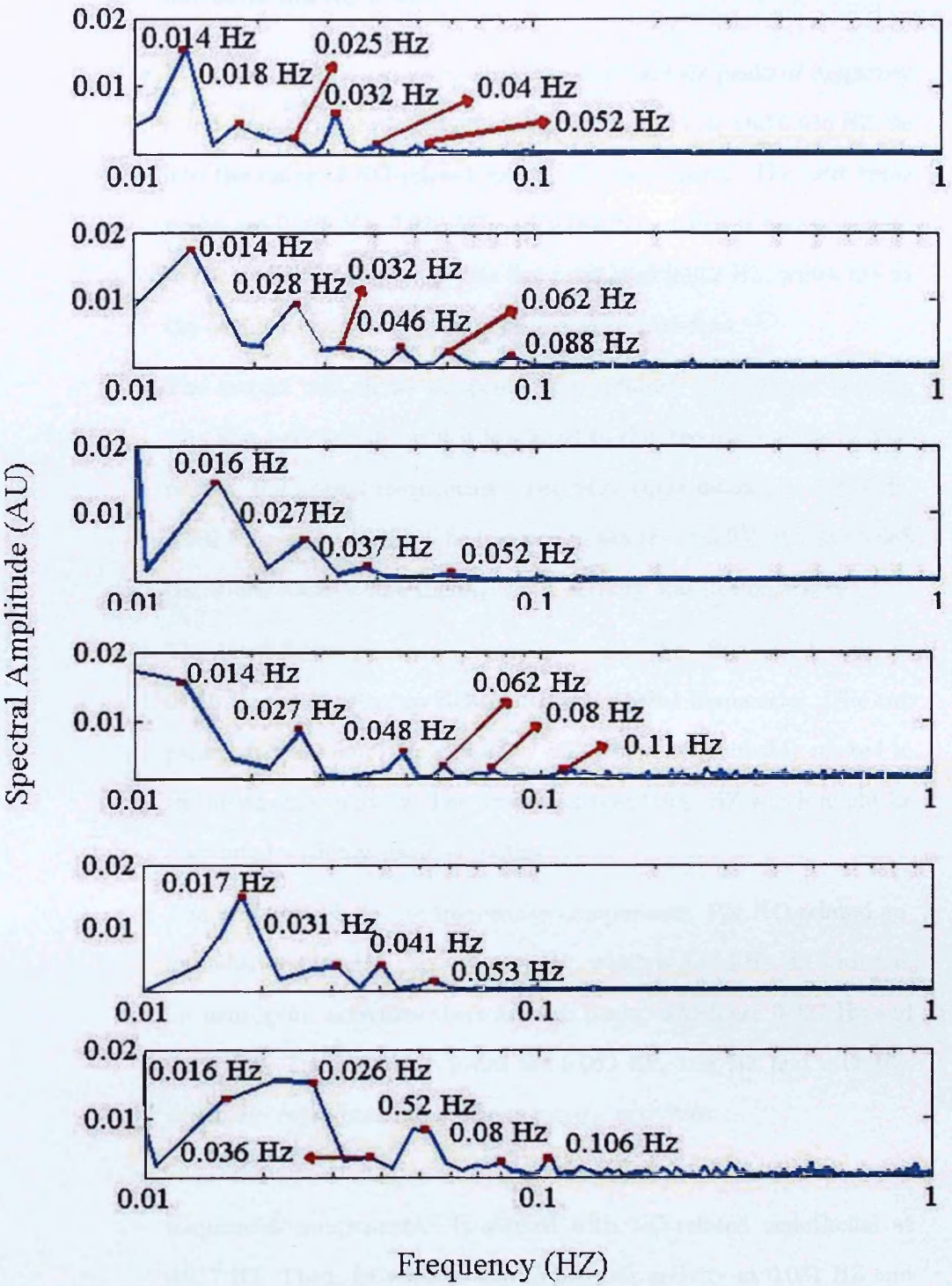

Figure 4.11: The main frequency components (red marks) of the vessel oscillation of six subjects by using Fourier transform.

can summarize this result as:

- In the first plot, it can be noticed that there are six peaks of frequency components. The first two peaks, which are 0.014 Hz and 0.016 HZ, lie into the range of NO-related endothelial frequencies. The next three peaks are 0.025 Hz, 0.032 HZ and 0.046 HZ, which is corresponding to the neurogenic activity. The last peak is at 0.052 HZ, which lies at the edge between neurogenic and myogenic activities.
- The second plot shows six peaks of oscillatory components as well. The first peak is 0.014 which is related to the frequency range of NO-related endothelial frequencies. The next three peaks are 0.028 Hz, 0.032 HZ and 0.046 HZ. The last two peaks are at 0.062 HZ and 0.088 Hz, which likely where the myogenic activity was demonstrated.
- The third figure presents four main peaks. The first one locates at 0.016 Hz which refers to NO-related endothelial frequencies. The two peaks after are 0.027 Hz and 0.037 HZ, which are probably related to the neurogenic activity. The final peak is at 0.052 HZ which might be associated with myogenic activities.
- The next plot shows six frequencies components. For NO-related endothelial frequencies, there is one peak, which is 0.014 Hz. In addition, for neurogenic activities there are two peaks, which are 0.027 Hz and 0.048 Hz. The last three peaks are 0.062 Hz, 0.08 HZ and 0.11 HZ, which are corresponding to the myogenic activities.
- From the figure after, it can be noticed that there are four peaks of frequencies components. It started with NO-related endothelial at 0.017 HZ. Then, followed by the neurogenic activity at 0.031 HZ and 0.04 HZ. The last peak is related to myogenic activities which is found at 0.053 HZ.
- At the last plot, the results shows that there are six main frequency

components. The first one is at 0.016 HZ, which lies into the range of NO related Endothelial oscillations. The next two peaks are 0.026 Hz and 0.036 Hz, which refer to the neurogenic activity. The last three peaks are at 0.052 HZ, 0.08 Hz and 0.106 Hz, which represents the myogenic activities.

From the above points, we can draw the conclusion that the oscillations that have been observed and computed from human skin subjects are for blood vessels oscillations and in the range of NO related endothelial, myogenic and neurogenic activities as identified previously using laser doppler flowmetry. First, all defined peaks that were related to myogenic activity have been previously observed in blood flow signals, and also in the Heart Rate Vibration (HRV) signals [81]. Moreover, it has been hypothesized to be associated with blood-pressure regulation, which continually cause changes in intro-vascular pressure from the smooth-muscle cells in the vessel walls and is related to the rhythmic regulation of vessel resistance to the blood flow initiated by concentrations of metabolic substances in the blood as well [82]. Second, the peaks related to the neurogenic activity have been found in blood-pressure and also in HRV signals by several authors . It has been demonstrated from previous research on human data that this peak was dramatically reduced after denervating, local and ganglionic nerve blockade and after sympathectomy. The final obtained activity refers to NO-related endothelial frequencies, which is related to endothelial functions in vessels and which is the main cause of the vasomotion [83].

4.3.7.2 Fourier transform for phantom data

To make an unambiguous conclusion about this point, the Fourier transform was established on phantom data as well to detect all frequency components and to compare the characterized values with the defined mathematics of oscillators of cardiovascular dynamics.

A- Data Processing

The collected data from the phantom of one fishing-lines in the section (3.4.6.1), page 79 was used in this particular study. The Fourier transform was applied to the fluctuation area of the fishing-line by using the same steps in the last section. This obtained results was displayed in the figure (4.12)

B- Results

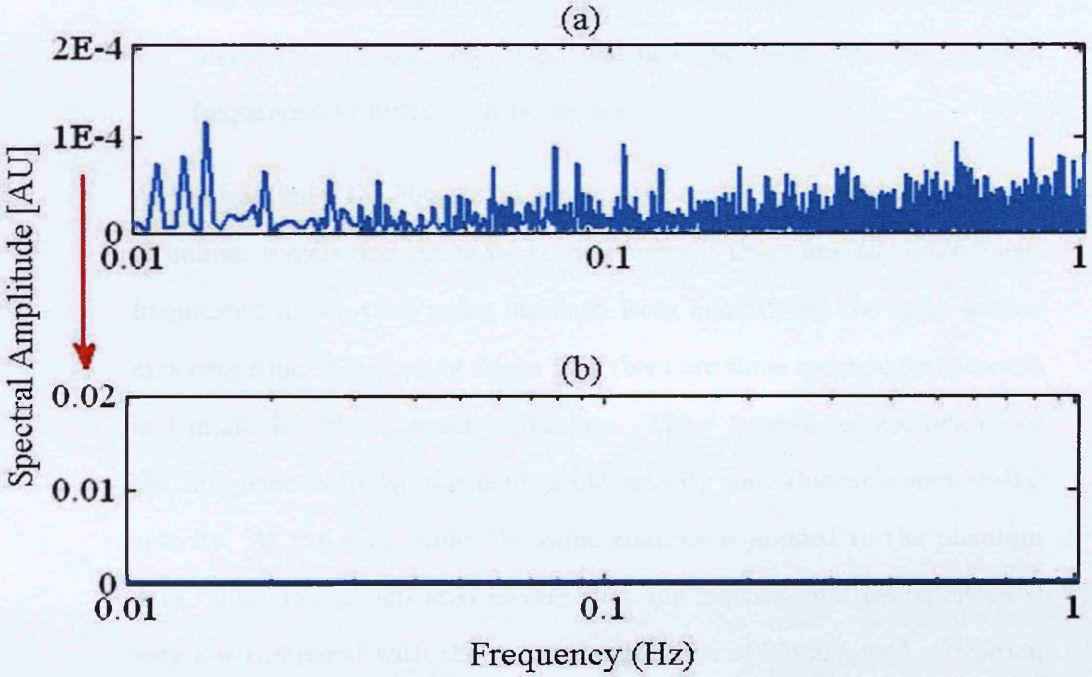

Figure 4.12: (a)Spectral amplitude of the fluctuations of the contour of the phantom obtained by Fourier transform, (b) re-scaled spectral amplitude of the phantom to be similar to the scale of the spectral amplitude of vessel oscillation in figure (4.11)

It can be seen from the figure (4.12) that decomposed frequencies from

phantom data are so random and unstructured that no clear frequencies can be detected in the plot. As all computed frequencies are absolutely coming from stable phantom data, any defined peaks will be clearly due to the instrumental noise variations. In addition, the spectral amplitude of Fourier transform is around a hundred times less than the defined amplitude for human skin data. So in the same figure, the spectral amplitude on the y-axis is re-scaled to be similar to the spectral amplitude for human skin. This conversion shows clear and substantial evidence that the resolved frequencies of vibration by phantom approach zero amplitude in comparison with the resolved frequencies of fluctuation by vessels.

As has been said, the Fourier transform has been applied to the fluctuations of human vessels and phantom to determine if there are any constituent frequencies in the time series obtained from quantifying the cross section area over time. The finding shows that there are three spectral components in human skin blood vessel oscillations. These frequencies are related to the myogenic activity, the neurogenic activity and rhythmic endothelial activity. At the same time, the same analysis is applied to the phantom data. The results indicated clearly that the instrumental contribution is very low compared with the spectral amplitude of blood vessel oscillation frequencies.

4.3.8 Wavelet transform for experimental data

The FFT constitutes the basic method of frequency analysis, but it has shortcomings when applied to the analysis of finite or non-stationary data. Firstly, the FFT cannot follow a time-varying frequency. If the signal has a time-varying frequency, the corresponding frequency peak is broadened. Furthermore, it is dependent on the window length and detects the low frequencies which demands a wide window. To improve the frequency resolution and to reduce a global effect

of any sudden change, the more suitable technique for signals with time-variable frequencies is introduced which is a wavelet transform.

Wavelet analysis is a time-frequency method which allows a signal to be viewed in multiple resolutions. It is a function that helps to find the detailed frequencies of a continuous signal by extending it over a wide frequency scale and varied their periods in time. This function is effective for noise reduction, and for detecting the faults in machinery, or in sensor measurements such as biomedical signals. Usually one can assign a frequency range to each scale component, which by then can be studied with a resolution that matches its scale. Wavelet transforms have advantages over traditional Fourier transforms for representing functions that have discontinuities and sharp peaks, and for accurately de-constructing and reconstructing finite, non-periodic and/or non-stationary signals [84]. From defined results in the part of analyzing the data by using the Fourier transform, it can be noticed that there are sharp peaks in the frequency domain and they are spread over a wide frequency interval. To overcome this problem and to achieve a good time resolution for both the high frequencies and low frequencies in the data collected, the continuous wavelet transform was used. This transform gives the possibility to have logarithmic frequency resolution, which crucial for the detection of low-frequency components. The wavelet transform function was introduced in details in Appendix A-11-1.

4.3.8.1 Wavelet transform for human data

1- Data Processing

At this stage, to achieve the purpose of analysis and before applying the wavelet transform, fifteen minutes of recording data was selected as a constant time to reduce any noise frequency coming from slight movements and to evaluate all low frequencies related to the vessel function. In this part, the previous six data at section (3.4.6), page 106 were selected. Before

applying t he wavelet transforms a reasonable frequency scale was chosen according to the frequency intervals. A scale between 0.0095 Hz and 2 Hz is fixed to include the highest frequency of the cardiac oscillations at 2 Hz and the lowest frequency of No related endothelial at 0.0095 Hz. Moreover, the high frequency of recording signal was filtered by using average filter of data. In addition, the transform was not calculated for the first and last 100 second. Moreover, the influence of boundaries was reduced by dismissing the first and the last points from the transform function. Finally, the wavelet transform was applied to the vasomotion processed signals in order to capture the time variability of the fundamental oscillation frequencies within these measurements [85] [Appendix A-11-2].

2- Results

From the three dimensional displayed plots in the figure (4.13), the absolute value of the wavelet transform as a function of frequency and time are presented for six sets of human data. For clearer presentation, the x-axis was marked at the boundary of the cardiovascular oscillation bands in the logarithmic scale which are [0.0095, 0.021, 0.052, 0.145, 0.6, 1], whereas time is plotted on a linear scale to figure out easily any related frequency. It can be clearly delimited from all defined plots in the figure that three bands of constituent frequency components in vascular oscillation can be recognized in all measured subjects:

- First, all have characteristic frequency peaks within the interval 0.01 Hz to 0.02 Hz are related to rhythmic endothelial activity.
- Next all have defined peaks around (0.021 - 0.052) Hz. These have previously been associated with neurogenic activity which regulates the blood pressure by changing the radius of the vessels.

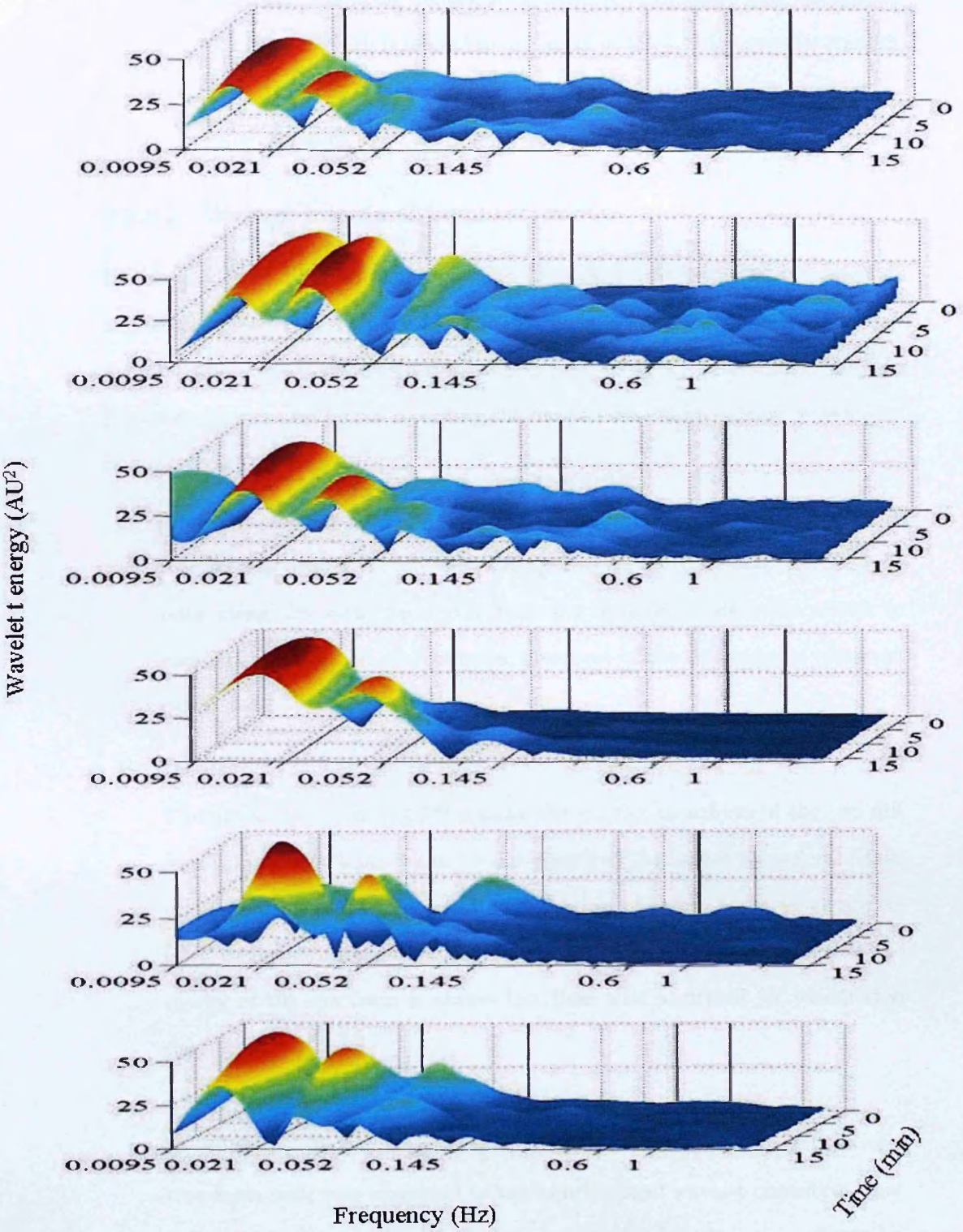

Figure 4.13: The wavelet energy amplitude of vasomotion for 6 different subjects

- The last remarkable frequencies is from the frequencies intervals around 0.1 Hz and which is related to myogenic activity of the vascular smooth cells in the vessels which respond continually to changes in intravascular pressure.

4.3.8.2 Wavelet transform for phantom data

In this part, two different phantoms with immersed fishing-line were created as explained in section (4.2), page 43. The first on was imaged by exactly the same experimental steps that described in section (4.3), page 46. The second one was placed on human arm before recording the data to mimic the natural movements of human body.

A- Data Processing

The wavelet transform function was applied on the both cases of phantom data using the same parameter that was applied on data for vessels to compare similarly all characteristic measures of the dynamics in phantom case.

B- Results

The figures (4.14) and (4.15) display the wavelet transform of the two different phantoms data. It can be easily noticed that there are several peaks in different locations that could be defined in phantom cases which are related to the instrumental noise level. In addition, it is clearly seen that the energy of the spectrum is always less than that identified for vasomotion signal.

By following the same previous routine in section (4.3.7.2), the wavelet transform scale was converted to the same scale of wavelet transform, that is defined for vessels. The finding shows clearly that the power of wavelet transform of the phantom is twenty five times less than the power of transform of the vessels. In addition, from the displayed figure (4.16), it is showed

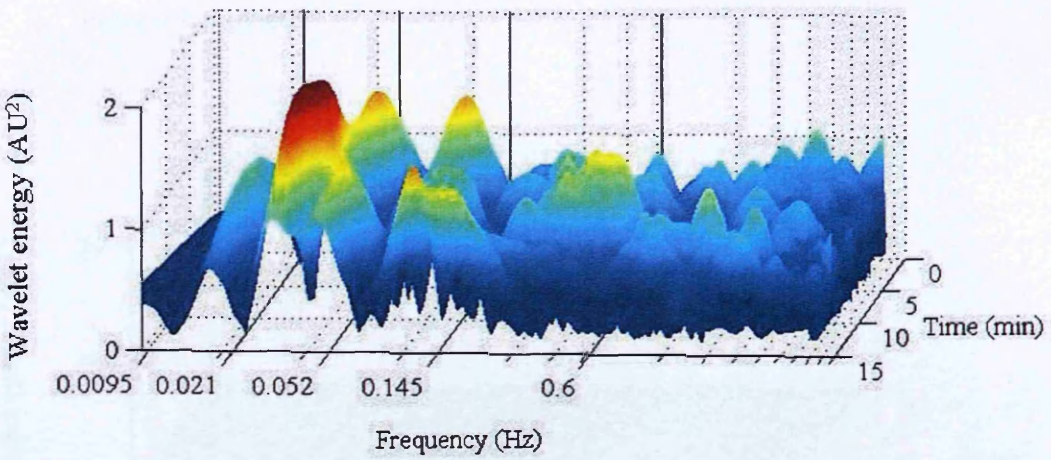

Figure 4.14: The wavelet energy amplitude of the stable phantom

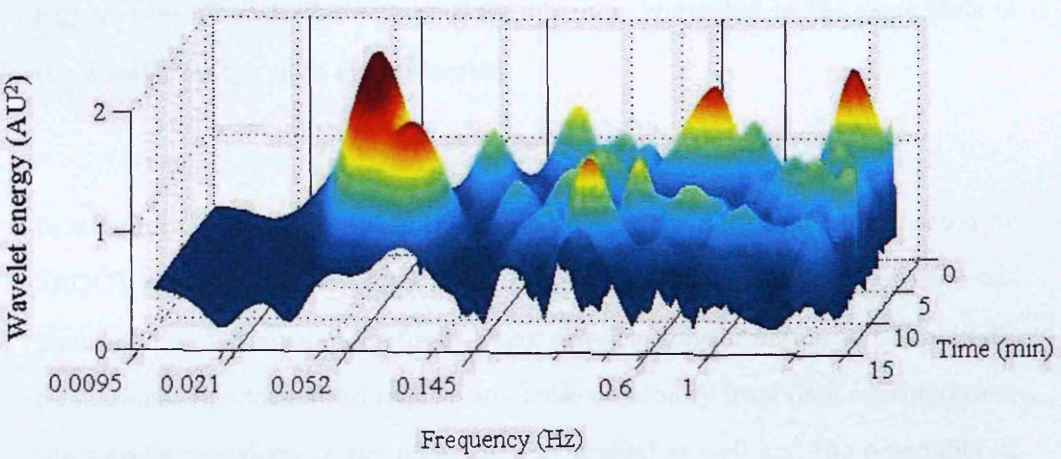

Figure 4.15: The wavelet energy amplitude of unstable phantom

that the power of spectrum of phantom goes to zero comparing to power defined for vessels. From this comparison and limitation step, it can be said that there is clear and substantial evidence that the power of all previous

peaks from human data are for cardiovascular oscillations and not from any other noise source.

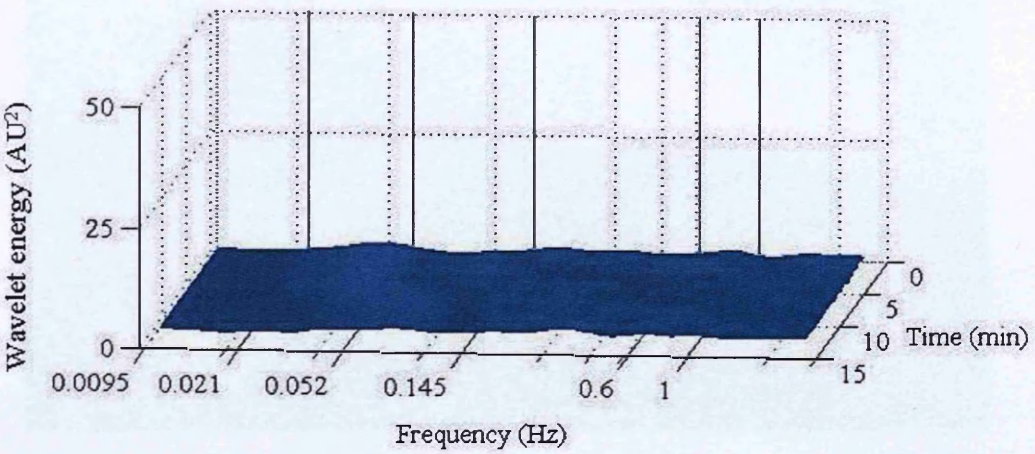

Figure 4.16: The wavelet energy of the phantom converted to the same scale of the wavelet energy data of vasomotion

In summary, in order to assess the oscillations of the data that are collected by SROCT to visualize the blood vessel movement, six time-frequencies were implemented and studied carefully by using wavelet transformation of the periodic oscillations. In addition, to remove any noise possibility from final consideration, the wavelet transform of the phantom was studied as well and the possibility of any effects from the natural body movement was eliminated. By logical analysis, the results described show that the frequency components from the phantom go to zero in comparison with what was determined by vessels. Furthermore, it can be noted clearly from all human subjects that there are three noticeable groups of constituent frequency components in vascular oscillations. These frequencies could be related to the myogenic activity, neurogenic activity and rhythmic endothelial activity.

4.3.9 Three dimensional images

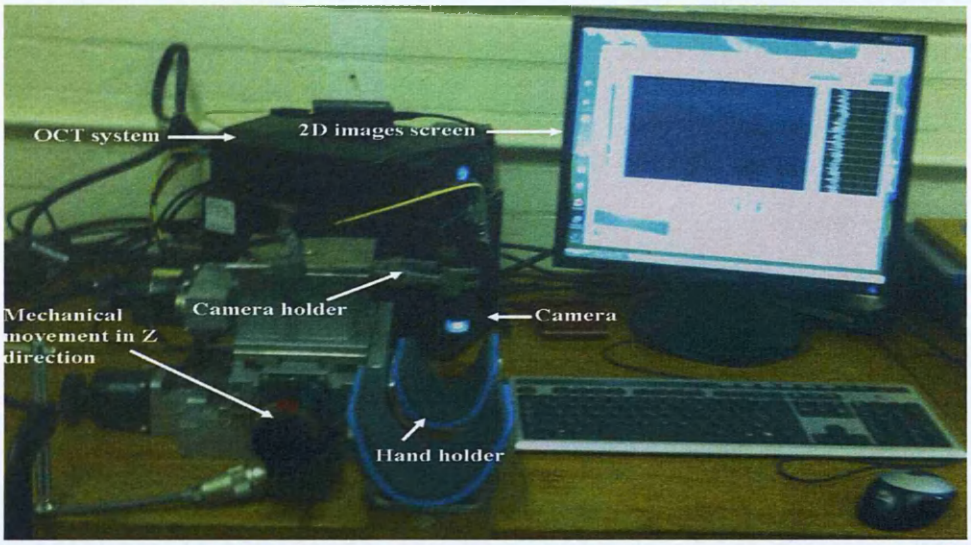

Figure 4.17: The experimental set-up of SROCT to create the 3D images.

The purpose of the three dimensional images (3D) is to enhance the performance of clinician in assessing anatomical information such as the orientation of blood vessels, cross-sectional area, and volume of disease. In addition, these kinds of images help to provide a good aspect of vision for the subject to help understand in detail skin layers and their locations. Moreover, it assists in understanding the necessity of stabilizing the hand and the camera during all measurements and provides a clear explanation about the variation of the vessel from one image to another in the same place which is due to the change of the cross sectional area by using this system. In this research we demonstrated the potential of SROCT for noninvasive imaging of living skin simultaneously by scanning rapidly two dimensional (2D) sequences images. At the same time, an automatic mechanical technique was used for moving the camera on the skin as has been described in the section (3.4.7). The data was recorded in a speed of 8 frames per second and every single window has a width of 2 mm. All defined images provide clear information under human skin at a depth of 0.3 mm.

The figure (4.17) presents the developed system that has been used to collect the data to reconstruct the 3D image for human skin and which will help to provide more information about any layers under skin.

In this section, we will present the results of 3D imaging of vessels under human skin non-invasively, using Spectral Radar Optical Coherence Tomography (SROCT) development technique. Moreover, a clear 3D gray picture of vessel under skin is seen by using image J computer program on the set of sequence 2D collected images. The figure (4.18) displays the 3D result on human skin and it can be noticed that the blood vessels can be easily outlined by this technique.

In other words, a visualization for some features lying under human skin in three dimensions has been achieved by using a development technique of SROCT which helps in understanding all underlying vessels in the real image. This technique does not result in a large error because the vessels are running parallel to the skin and a 3D object is projected in to 2D and analyzed as described in the previous section.

4.4 Conclusion

On the whole, visualizing the blood vessels inside the skin layers and detecting their oscillations *in vivo* is the main goal of this research. In this chapter, the human skin was imaged by using SROCT system and the results in the form of the figures and tables were presented to provide a certain mathematical and graphical conclusion about any experimental measurements at every section in this chapter.

- At first stage, several images at different places on human arm are created by using SROCT system. Then, the forearm was selected to be the place of

(a)

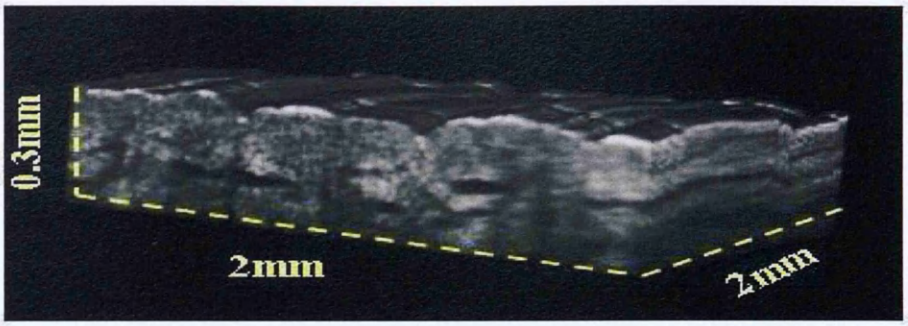

(b)

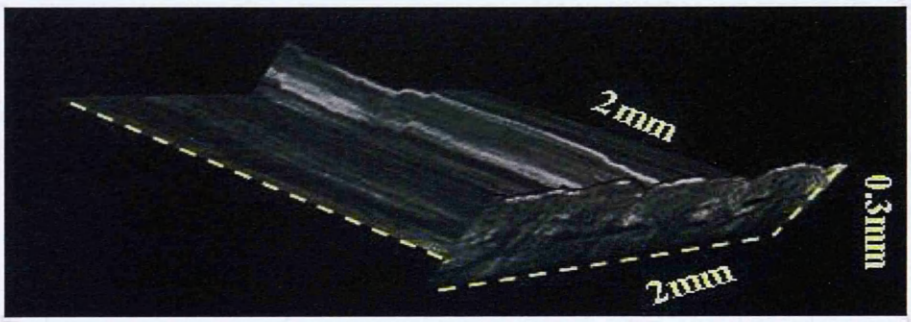

Figure 4.18: (a) and (b) Human skin images in three dimensions from different cross sections

all measurements as it was the best area that shows the clear vessels under skin.

- Subsequently, the intensity of skin images has been studied and the finding shows that it has unstable values for every single pixel and these values are decreased on going deep from the surface of the skin due to scattering properties of the light. Moreover, the correction factor of the images in the case of human skin was calculated for several subjects and it can be concluded that, similarly to the phantom case, there is no general correction value that may be applied to all calculations. Therefore, the general correction equation is applied on all collected data before starting any mathematical

calculation.

- Next, the montage imaging function was introduced and applied to one of the sequence images of a vessel. As a result, the oscillation of the vessel with the time is visualized by following the changing of the shape and the size of the image.

- After that, a movie was created for a series of images and the function of vessels was observed in time.

- Afterwards, the contour was made to detect the vessel and to approximate its area by following the same steps that had been utilized in the case of the phantom.

- Furthermore, the fluctuations of the cross sectional area of the vessel was carefully studied. In addition, the equivalent cases of phantom and vessel are compared graphically and mathematically in terms of the fluctuation of the area and it can be reasoned out definitely that the defined variations from human subjects are related to the vasomotion under skin.

- Simultaneously, the Fourier transform has been used on the fluctuations of the data by the vessel and the phantom to define if there are any constituent frequencies in defined fluctuations. The determination displays that there are three spectral components in vessels oscillations. These frequencies are related to the myogenic activity, the neurogenic activity and rhythmic endothelial activity. At the same time, this function is set on the fluctuation of the phantom data as well and the results determined that the instrumental noise is too low compared with the values for blood vessels frequencies.

- In a supplementary study, by using wavelet transformation of the periodic oscillations of vessels for 6 human subjects, it can be absolutely determined that there are three noticeable groups of constituent frequency components in vascular oscillations which were exactly the same as was figured out by

Fourier transform. These frequencies represent the myogenic activity, the neurogenic activity and the rhythmic endothelial activity. In addition, to remove any noise possibility from final consideration, the wavelet transform of phantom was studied with a count of the natural body movement. By logical analysis, the defined shows that the frequency components by phantom approach zero in comparison with those defined by vessels.

- Eventually, SROCT technique was developed to allow the imaging of three dimensional (3D) pictures of human skin which will provide clear evidence for all underlying vessels in the real image.

In simple terms, the images of human skin by using the SROCT technique were studied carefully in detail and the main aim of this work, which is visualizing the vasomotion in real time by using OCT system was reached. To best to our knowledge, there is no similar study for blood vessels oscillation as a function in real time. Also, no similar results of visualizing blood vessels variation have been reported till now.

Chapter 5

Effect of temperature on vasomotion

5.1 Introduction

Skin is the main controller to regulate the thermodynamics of the human system and it is strongly affected by external temperature. As the core body temperature needs to be maintained for normal physiological activities, body temperature is regulated through a balance of heat absorption, production and loss. When the external temperature is increased, blood vessels in the skin dilate and heat is lost through their walls [86]. Sweat is also produced, which evaporates and lowers temperature. If a human is too cold, the blood vessels constrict, conserving heat. In fact, there are different mechanisms involved in the response to local temperature changes [87]. For example: endothelial and smooth muscle cells respond to temperature changes in order to produce an appropriate redistribution of vascular resistance. Moreover, venous basal tone may respond to temperature increase with constrictions to help regulate the systemic blood flow [88].

From the accounts of several early reporters, the fluctuations of skin blood flow during temperature provocation have been studied [89], [90], [91]. It was identified

that local heating causes an increase in skin blood flow by activating sensory axon reflex and metabolic nitric oxide controls. Moreover, it has been observed during the heating, that on increasing the skin temperature there is shown an increase in spectral energy associated with vasodilation where myogenic mechanisms play a key role. The mechanism responsible for this indirect vasodilation remains unclear. It was hypothesized that the remote skin area will have enhanced synchronization of blood flow oscillations, thus inducing a vasodilatory response [92].

Measures that will enable the correct interpretation of the tissue thermal and vascular response to heating are very essential for users of hyperthermia equipment and for researchers in various related studies. Exploring rhythmical fluctuations in cross sectional area of blood vessel time series during increased local heating is the main motivation beyond the scope of this section. A detailed characterization of the dynamic vessels with the temperature profiles within the skin was made by using a locally developed method, which relies on combining the SROCT imaging technique with the Peltier-based Melcor Thermoelectric Temperature Controller system (Temperature controller, MTTC-1410, Melcor, Trenton, NJ). The particular combination was made to measure and control an external heating temperature at the same time as measuring and visualizing the vasomotion of human skin. This part of the research aims to help understanding the mechanisms of vasomotion in response to temperature change and to define the oscillatory nature of vessels during changes in skin temperature. In addition, this work might find particular application in skin thermal lesions research, that is, research on the influence of physical and chemical factors on skin microcirculation [93].

5.2 Methodology and experimental set-up

This study focuses on the effect of increasing the local skin temperature on blood vessel oscillations. Because of the complexity of understanding the cardiovascular

oscillations and their relations to any temperature changes at the same time, we have followed some previous investigators, who have carried out an interpretation of the vascular contribution in blood flow amount to heat transfer in surrounding tissues by using Peltier-based Melcor Thermoelectric Temperature Controller system (MTTC) for heating skin [94]. We used a modification of the commercially available system which had been modified by the Department of Physics, University of Lancaster to enable local heating of the skin and recording of skin physiology. Furthermore, in order to capture the time variability of the basic oscillation frequency of the area of the vessel, the data was recorded for some subjects and then characterized both mathematically and graphically.

5.2.1 A model of Melcor Thermoelectric Temperature Controller (MTTC) with SROCT

At this part of the methodology, I will introduce first the Melcor Thermoelectric Temperature Controller (MTTC) and then I will describe the new developed system that has been used in this part of the work. In general, the MTTC is a precision instrument which provides accurate temperature control of the thermoelectric device. The fundamental core of the system parts are shown in figure (5.1). It can be seen that the system comes mainly standard with two main parts: a base unit and a temperature- controlled metal plate.

The unit's LED front control panel can be used to adjust the setpoint of current temperature.

1- The base unit has a dimension of 15 cm× 12.5 cm× 26 cm and an approximate weight of 4.5 Kg. It can be seen that this part has a LED (Light Emitting Diode) front control panel to view the current temperature of the metal plate, which is used to attach to the subject. In addition, it contains a four button user interface to adjust the set point temperature.

2- The temperature-controlled metal plate is made from solid state heat pumps

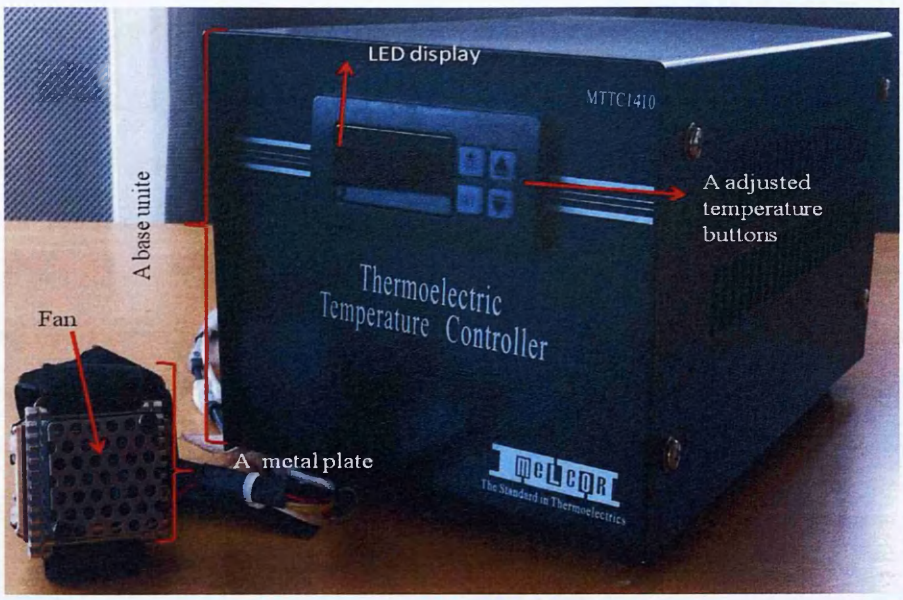

Figure 5.1: Melcor Thermoelectric Temperature Controller, MTTC-1410, Melcor, Trenton, NJ

that allows the heating transfer from one side to another. It contains a fan which is mounted directly on the metal plate to provide forced air convection to the internal heating system. Both the metal plate and fan have a suitable weight to be placed directly on the human arm without affecting the regular microcirculation of the human body.

In this particular work, MTTC technique is utilized for heating the skin for a controlled time because it has several properties which are important for our work. The main characteristics and features of this device are [94]:

1. A non-invasive monitoring of skin temperature.
2. A quickly controlled temperature between 0° C and 100° C.
3. A high accuracy with fast response.
4. Reduced space, size and weight on skin.
5. Virtually no electrical noise.

6. Reliable operation with no sound.

For all of these suitable features that help in performing the specific research goal, MTTC heating instrument was modified for an earlier study with the help of the electronic workshop in the Physics Department at Lancaster University. This was achieved by designing a new temperature- controlled metal plate with a small aperture in the center to fit the camera of SROCT. This joining of SROCT imaging technique with MTTC helps to visualize the blood vessel oscillations at the same time as heating the skin and at the exact specific area. The figure (5.2) displays the newly designed method that is used in this work.

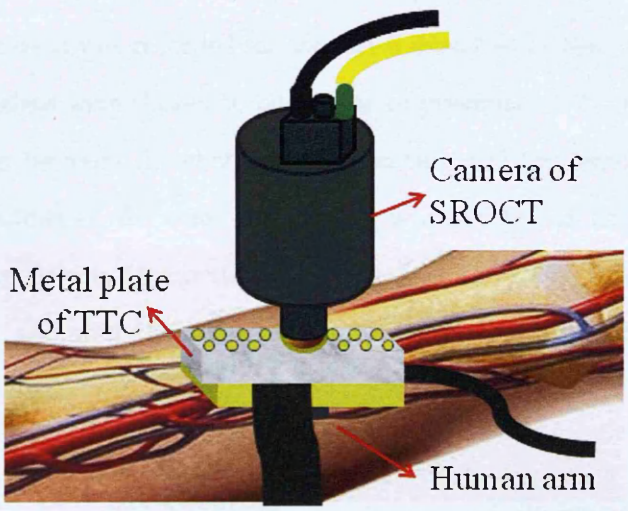

Figure 5.2: A diagram of human forearm measured by combining SROCT and MTTC, both supported together by a stable stand holder

5.2.2 Data recording

All tests were performed on human forearms at the laboratory of the Physics department. Three healthy subjects were recruited into the study. They each stabilize their arms on a comfortable holder and sit in a pleasant ventilated room at 20 $\pm$ 1.0 °C. Skin temperature was topically perturbed by attachment of the metal plate of the developed heating system, which was placed on the forearm.

The plate surface of MTTC activated control of the temperature in the area of measurement and the LED screen of MTTC enabled display of the temperature of the plate surface. At the same time, the camera of SROCT adjusted to ensure cross sectional view of the blood vessels.

A preliminary measurement of 2 minutes prior to the main measurement was made with the temperature controlled plate and image recording by SROCT at a natural temperature. Then, the temperature of the plate was gradually increased to 40 $\pm$ 1.0 and the recording was continued for 9 minutes. After that, the temperature was switched off to reduce the temperature to the original one and continually the data was recorded for the last 3 minutes. In this experiment, the temperature values were chosen to be similar to previous research, which looked for the relation between the changing temperature and the oscillation of blood flow [95]. In addition, the time of recording was selected as the maximum for recording image data is 15 minutes. Therefore, the time was divided with a few minutes before and after the main 10 minutes time of recording data during the heating of the skin.

5.2.3 Data pre-processing

The skin temperature and the time series of the area of blood vessels was analyzed by following generally previous papers in this matter [96], [97]. First, the time series of the data collected was de-trended by subtraction of a moving average over 250 seconds to remove the trend and any variability below 0.004 Hz. Next, every signal was subdivided at the point of temperature perturbation into three parts. In the three parts, the image and the time series of vessel oscillation were presented before, during and after heating. After that, the wavelet transform analysis was used to study blood vessel periodic fluctuations caused by local heating of an area of skin and to determine the change of the band of the frequencies of the basic cardiovascular oscillations within the change of the tem-

perature during the experiment. In this particular study, the minimum frequency resolution was selected as 1 over the recording frequency =1/8= 0.125 Hz. The maximum frequency resolution can be defines as 1 over the recording frequency multiply by the length of recording data in seconds= 1/8 × 900= 112.5 Hz. In addition, before applying the function, a reasonable frequency scale was selected according to the frequency intervals which are between 0.0095 Hz and 2.0 Hz. Furthermore, the x- axis marked the boundary of cardiovascular oscillations on a logarithmic scale, whereas the time is plotted on a linear scale to discover easily any related frequencies.

5.3 Results

The area of blood vessel response during local heating on the area of skin heating has been studied by using MTTC heating system. As skin heating stimulates vasodilation of blood vessels, it increases average blood flow. Therefore, different mechanisms are involved in the response to local heating of the area of skin which may affect all frequency intervals in cardiovascular oscillations. These responses may inform global thermoregulatory activity coordinated by the sympathetic nervous system rather than any local reaction.

In this part, three representative examples of blood vessel oscillations during increasing the skin temperature are presented in the figures (5.3), (5.4) and (5.5). These three figures show at the first line the image of human skin and the selected area of this particular study. The next line of the figures display the signals of the blood vessel oscillations divided at the point of temperature perturbation and the time series before, during and after temperature changing. After that, the three different images of the vessels are presented to show the vessel in each condition period. All figures are accompanied by 2D and 3D wavelet transforms of defined signals in the three separate periods of heating.

According to the figures, the increasing of the cross sectional area of the vessel and its oscillation have been particulary observed during temperature changing in both images and signals. These results are due to the rise of the vessel vibration when the skin was heated to 40°C from a regular temperature during the 10 minutes of heating. After this increase the fluctuations start slowly to reduce after moving the heating effect from the skin in the next three minute recorded time as the vessel tries to go back to normal activity after moving the external effect. In addition, the variability of area of the vessel is dramatically increased in each subject, which may be caused by the increasing of average blood flow and that is because of an increase in skin temperature. These changes enlarge the vessel average radius, hence increasing the relative contribution of all other oscillatory processes. Furthermore, relying on the results of the wavelet transform, we found an increase in the proportion of signal energy in all the frequencies related to all cardiovascular oscillations. In detail, we may notice from the figures that the increasing of frequencies are varied from person to person. In particular, as the radius of the vessel and the vasomotion are increased, all related dynamics will be affected from this change. As has been demonstrated from the figures, the energy of the intrinsic myogenic activity of vascular smooth muscle, the neurogenic activity of the vessel wall, and the mechanisms of vascular endothelial function are all markedly increased after heating the skin.

Subsequently, all the information from those figures has been studied carefully by applying the statistical analysis in each condition period on every set of data collected from the three participants. The table (5.1) explains clearly the results in this section by displaying the mathematical values between all tested subjects in terms of R.M.S (mm^2), mean (mm^2), the standard deviation (std) (mm^2) and the percentage of oscillation in each temperature duration.

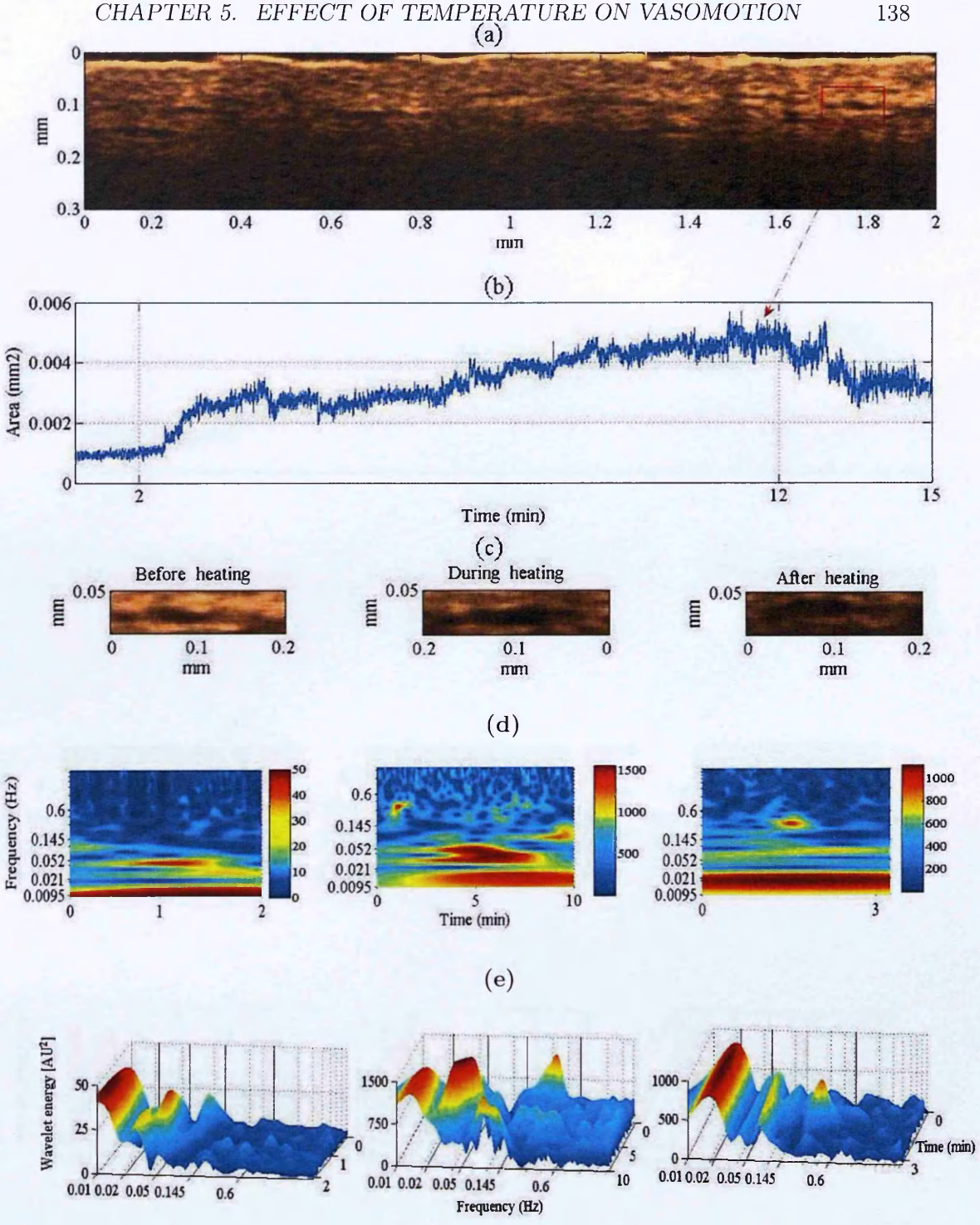

Figure 5.3: The effect of heating on vasomotion for subject 1: (a) the OCT image of human skin, (b) the oscillation of the area of vessel while the heating is applied after 2 min and is moved after 12 min from the beginning of the recording, (c) the images of the vessel before, during and after heating, and (d), (e) the wavelet energy in 2D and 3D where the brightest colour defines highest wavelet energy

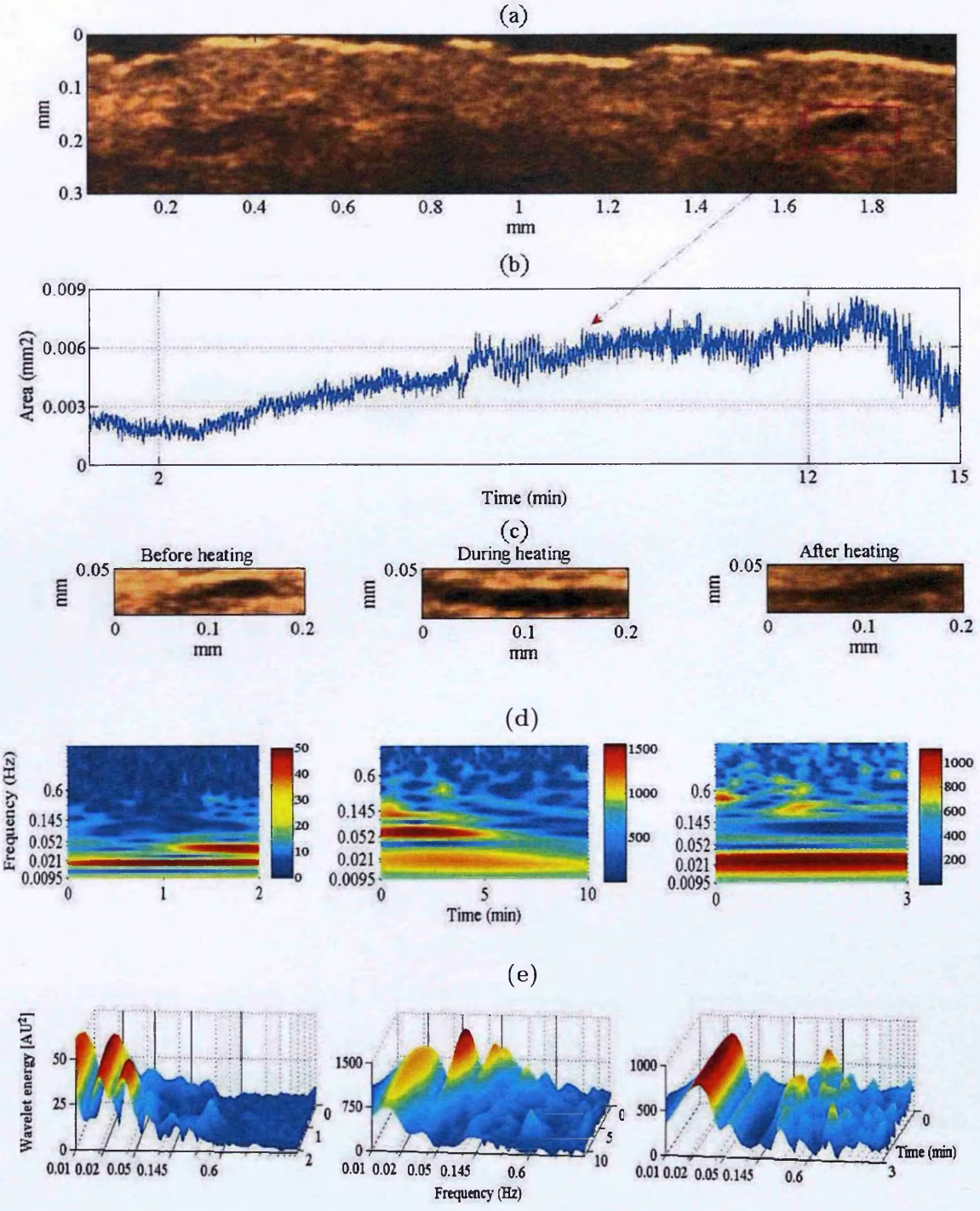

Figure 5.4: The effect of heating on vasomotion for subject 2: (a) the OCT image of human skin, (b) the oscillation of the area of vessel while the heating is applied after 2 min and is moved after 12 min from the beginning of the recording, (c) the images of the vessel before, during and after heating, and (d), (e) the wavelet energy in 2D and 3D where the brightest colour defines highest wavelet energy

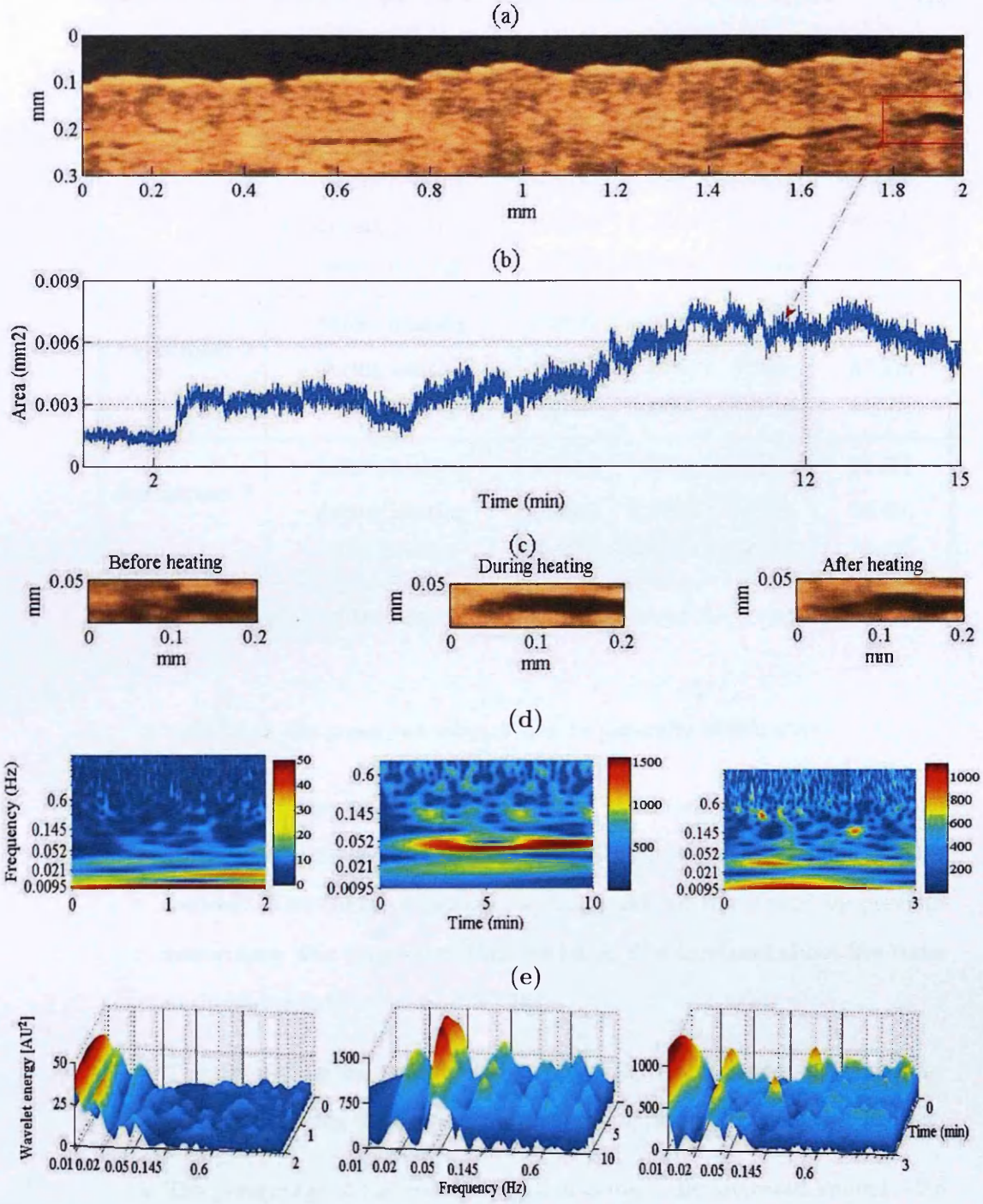

Figure 5.5: The effect of heating on vasomotion for subject 3: (a) the OCT image of human skin, (b) the oscillation of the area of vessel while the heating is applied after 2 min and is moved after 12 min from the beginning of the recording, (c) the images of the vessel before, during and after heating, and (d), (e) the wavelet energy in 2D and 3D where the brightest colour defines highest wavelet energy

Subject	Period of calculations	R.M.S (mm^2)	Mean (mm^2)	std (mm^2)	Oscillation %
Participant 1	before heating	0.0012	0.0011	0.00029	24.16%
	during heating	0.0048	0.0048	0.003	62.5%
	after heating	0.003	0.0029	0.0014	46.6%
Participant 2	before heating	0.0022	0.0022	0.00045	20.5%
	during heating	0.0086	0.0087	0.005	57.5%
	after heating	0.006	0.0061	0.0019	31.6%
Participant 3	before heating	0.0014	0.0012	0.00034	24.3%
	during heating	0.0052	0.0052	0.0031	59.6%
	after heating	0.003	0.0031	0.0013	43.3%

Table 5.1: The effect of the heating on the oscillations of the vessel cross sectional area

According to the presented table, it can be generally stated that:

- The area of the vessel is increased about ~4 times during the heating for 10 minutes and then step reduced as has been noticed in 3 minutes after heating. This range of increase is comparable to that found by previous researchers, who determined that the blood flow increased about five times during heating the skin to 40°C [95].

- The std of the vessel, which refers to the oscillation of the vessel, is raised by ~10 times during the heating and then dramatically declined after heating.

- The percentage of the vessel oscillation is markedly increased around ~2.5 times during the heating and dropped to ~1.5 times after heating.

These indications can be simplified in two tables to present the changing of the each of these values during and after heating. The symbols ↑ and ↓ in the tables refer to the increasing and decreasing in values.

Subject	Area (mm^2)	std (mm^2)	Oscillation %
Participant 1	↑ 4 times	↑ 10.3 times	↑ 2.58 times
Participant 2	↑ 3.9 times	↑ 11.1 times	↑ 2.8 times
Participant 3	↑ 3.7 times	↑ 9.1 times	↑ 2.45 times

Table 5.2: The changing of the blood vessels cross sectional area, its standard deviation (std) and the oscillations compared to before heating in three participants

Subject	Area (mm^2)	std (mm^2)	Oscillation %
Participant 1	↓ 1.59 times	↓ 2.14 times	↓ 1.3 times
Participant 2	↓ 1.43 times	↓ 2.6 times	↓ 1.8 times
Participant 3	↓ 1.67times	↓ 2.3 times	↓ 1.4 times

Table 5.3: The changing of the cross sectional area, its std and the oscillations within 3 minute of removing the heat source compared to the values obtained during heating

The results in the last two tables indicate that there are no fixed numbers of increasing and decreasing in each value during and after heating and these values vary from one person to another. However, there are general conclusions, which can be drawn, which are that there is an obvious increase in all of the areas of the vessels, the standard deviation and the percentage of the oscillation during the heating. In addition, there are noticeable decreases in all these functions after removing the heating effect from the skin.

Consequently, from displayed results in figures (5.3), (5.4) and (5.5), and relying on the studying of the wavelet transform for each period in all the subjects, it can be seen that the spectral amplitudes of the wavelet transform are enlarged in the proportion in all the frequency intervals to cardiovascular oscillations. In

detail, the endothelial function is increased and a dramatic rise occurred in the neurogenic activity followed by increasing myogenic activity and marked fluctuation in the oscillations with frequencies related to the respiration and cardiac activities after heating. At the same time, we may notice the decrease in energy of the wavelet transform three minutes after the end of heating in all the frequency intervals with the dynamics of the cardiovascular oscillations. All these observations are presented in table (5.4) to clarify the changes after applying the heating and after removing it.

Subject	Oscillations	During heating	After heating
Participant 1	Endothelial	$\uparrow \sim 25$ times	$\downarrow \sim 1.3$ times
	Neurogenic	$\uparrow \sim 70$ times	$\downarrow \sim 2.5$ times
	Myogenic	$\uparrow \sim 30$ times	$\downarrow \sim 3$ times
	Respiration	$\uparrow \sim 100$ times	$\downarrow \sim 3$ times
Participant 2	Endothelial	$\uparrow \sim 13$ times	$\downarrow \sim 1.1$ times
	Neurogenic	$\uparrow \sim 30$ times	$\downarrow \sim 5$ times
	Myogenic	$\uparrow \sim 30$ times	$\downarrow \sim 3$ times
	Respiration	$\uparrow 30$ times	$\downarrow \sim 2.5$ times
Participant 3	Endothelial	$\uparrow \sim 12$ times	$\uparrow \sim 1.3$ times
	Neurogenic	$\uparrow \sim 50$ times	$\downarrow 2.8$ times
	Myogenic	$\uparrow \sim 30$ times	$\downarrow 3.2$ times
	Respiration	$\uparrow \sim 100$ times	$\downarrow \sim 1.4$ times

Table 5.4: The changing of the values during heating compared to 3 minutes after removing the heat source

The results in table (5.4) show the range of the changes of the energy of the wavelet transform in some of the cardiovascular oscillations during and after heating and it can be concluded that all these oscillations are increased during the heating and then start to reduce after heating and their values are different from

one subject to another.

Over all, the oscillation of blood vessel responses during and after skin heating have been studied by using the MTTC heating method. The figures and the tables provided a clear conclusion about the changing of different mechanism of the responses to heating skin. In general, there is an obvious increase in the area of vessel and all related statistical functions as well, such as std and percentage of oscillations after heating, and then slow reduction of its values after heating. Also, there is a clear increase in the energy spectral amplitude of the wavelet transform in related cardiovascular activities during heating and decrease in its values after heating.

5.4 Conclusion

In simple terms, we have used a Thermoelectric Temperature Controller (MTTC) metal plate in conjunction with Spectral Radar Optical Coherence Tomography (SROCT) to investigate dynamical aspects of vasomotion, in response to temperature change. We have used previous image analysis steps to define the fluctuation of data collected such as: R.M.S, the standard deviation std and the percentage of oscillation in each temperature duration. Moreover, we applied wavelet transform function to study the changes in the oscillatory components of blood vessel areas due to local heating of the skin. We conclude from analytical figures and statistical tables that the mechanisms of vasomotion, in response to temperature increase, is to gradually increase the area of the vessel and its fluctuation, thus increasing markedly the relative contributions of all the other cardiovascular oscillation components. At the same time, these increases start dramatically to drop down after removing the heating effect from the skin. These changes appear to different a little from one person to another further data are required.

Chapter 6

Summary of the results and future work

6.1 Summary of the results

On the whole, as non-invasive imaging techniques become the normal for studying many major diseases, some of these current techniques have been generally reviewed to select the most suitable technique to achieve the aims of this thesis, which are visualizing and studying the diameter oscillation of the smallest vessels in real time under human skin. The comparison between several imaging techniques was widely made, and it led to the conclusion that SROCT is the most suitable non-invasive system for visualizing vasomotion under human skin in real time, and which will guide this work to achieve the main goal of this research.

In the first part of this research, tissue-mimicking phantoms of human skin were studied to evaluate the SROCT system and to provide the right way of the measurements and the steps for analyzing any future data on human skin. The clear results for experimental measurement on the phantom was presented in the form of the figures and tables and the summary of the conclusion of this results are:

- Firstly, the accuracy of SROCT measurement was evaluated and the finding

showed clearly that all measurements by using SROCT images and data analysis by MatLab image processing toolbox provide high precision.

- Subsequently, the results indicate that the intensity of images steadily decreased with depth, which guided us to calculate a correction factor for the images to normalize all pixels in intensity and verify any mathematical function applying to different depths.

- Meanwhile, the intensity changes of the image with depth was studied to identify the correction factor of the images. However, the results indicated that there is no general correction number and it is varied from subject to another. For that reason, we attempted to define the correction factor to each created image for each experiment before starting any calculation.

- Next, the contour function was studied carefully before it was applied on the simulated vessel. After that, the area of the contour was calculated by converting the corrected intensity images to the binary images and then summing all zeros pixels into a cropped image.

- Furthermore, investigation of the SROCT noise level was defined by using different subjects to trace the fluctuation level of the instrument. These different subjects were fishing-line in stable phantom, several different fishing-lines in the phantom at different depths, and several bubbles in the phantom. The findings show clearly that there are normally fluctuations in the stable phantom, and that the difference in percentage of the instrumental noise level depends on the cross sectional area, depth and stability of the subject.

- Finally, several three-dimensional images for the phantom layers were obtained providing a clear visualization of any features inside the subject.

After studying all data related to the phantom, the human skin was studied by using SROCT system. To the best of our knowledge, there is no similar study for

cross sectional area of blood vessel oscillations as a function in real time. Also, no similar results of visualizing blood vessels variation have been reported till now. In general, the results that were obtained in this part of the study are:

- Formerly, several images at different places on the human arm were created by using SROCT system. Then, the forearm was selected to be the place for all measurements as it was the best area that shows the vessels clearly under the skin.

- Subsequently, the intensity of skin images have been studied and the finding shows that there are unstable values for every single pixel and these values are decreased on going deeper from the surface of the skin due to scattering properties of the light.

- Moreover, the correction factor of the images in the case of human skin was calculated for several subjects and it was concluded that, similarly to the phantom case, there is no general correction value that may be applied to all calculations; therefore, the general correction equation is applied on all collected data before starting any mathematical calculation.

- Next, the oscillation of vessel with the time was visualized by introducing the montage function and applying it to one of the sequences of images of a vessel to follow the change of the shape and the size of the image.

- After that, a movie was created for a series of images and the function of vessels was clearly observed in time.

- Afterwards, the contour was made to detect the vessel and to approximate its area by following the same steps that had been utilized in the case of phantom.

- Furthermore, the oscillation of the area of the vessel was carefully studied. In addition, the equivalent cases of phantom and vessel were compared graphically and quantitatively in terms of the fluctuation of the area and it

was reasoned out definitely that the defined variations from human subjects are related to the vasomotion under skin.

- Simultaneously, the Fourier transform has been used on the time series of the cross sectional area of the vessel and the phantom to investigate whether there are any characteristic frequencies. The analysis reveals that there are three spectral components in vessels oscillations which are the myogenic activity, the neurogenic activity and rhythmic endothelial activity as described previously in human skin using Laser Doppler Flowmetry (LDF) for example.

- At the same time, the Fourier transform was also used to analyze the fluctuations in the cross sectional area of the phantoms and the results determined that the instrumental noise is low compared with the values for blood vessels frequencies.

- In a supplementary study, by using wavelet transformation of the time series of the cross sectional area of vessels for 6 human subjects, it can be reliably determined that there are three noticeable groups of constituent frequency components in vascular oscillations which were exactly the same as were obtained by Fourier transform.

- In addition, to remove the possibility that the characteristics frequencies obtained could be due to noise, the phantom was imaged when placed on human arm, to allow the influence of body movement to be taken into account. However, the frequency components obtained in this case approach zero and are negligible compared to those obtained for vessels.

- Eventually, the SROCT technique was developed to allow the creation of three-dimensional (3D) pictures of human skin which provide clear evidence that under laying vessels can be seen in the image.

In the final part of the study, we have used a Thermoelectric Temperature Con-

troller (MTTC) metal plate in conjunction with Spectral Radar Optical Coherence tomography (SROCT) to investigate dynamical aspects of vasomotion, in response to temperature change. The figures and the tables provided the following conclusion about the changing of some of the mechanisms in response to heating skin.

- Firstly, the increase of the area of the vessel during heating and the subsequent reduction in the area after heating was visualized in real time.
- Next, from calculated plotted figures, the findings show that, the range of the area oscillation were increased during the heating, and then decreased after removing the heating effect from the skin.
- In addition, it can be seen from the figures, that there is a clear increase in the energy spectral amplitude of the wavelet transform in all investigated frequency bands related to previously explained cardiovascular activities during heating, and a decrease after heating.
- Finally, from the statistical tables, the mechanisms of vasomotion increase gradually in response to temperature, thus increasing markedly the relative contributions of other cardiovascular oscillation components. At the same time, these increases start to dramatically drop down after moving the heating effect from the skin. However, all these changes differ from one subject to another.

6.2 Further work

These results show that Spectral Radar Optical Coherence Tomography (SROCT) is a viable technique for visualizing the blood vessel oscillation in real time and for obtaining information about this rhythmic variation in vascular diameter and cross sectional area.

As has been said before there have been no similar results obtained previously

to those presented in this study. Therefore, one should try to achieve the largest sample size possible for more accurate statistics and confident results. In addition, I suggest that the subjects are broken down into subgroups (i.agent, gender, treated with curare, which relaxes the skeletal muscles or not) to draw a precise conclusion about each specific group. More physiological measurements would be useful for further study in this field. It is recommended that any future study should consider including the following: a standardized arm and continuous measurement. Furthermore, it could be useful repeating the measurement several times for the same subject to assess the reproducibility of skin microvascular activity.

As with any investigation some compromise must be reached between what is desired and what can be practically achieved. Other techniques of analysis could be also useful to investigate a harmonic relationship of these biological oscillators. It would also be possible to use Laser Doppler Flowmetry (LDF), which measures the blood flow velocity, combined with OCT images within same area to study the relation between the blood flow oscillation and the vasomotion for the same subjects and at the same time.

It would also be valuable to find a way to extend the time of recording the data to reach 30 minutes, which will help provide more precise information about the low frequency oscillations. In detail, this extension of time will open another area that could be explored, which is using different external effects on human skin and study carefully the data during a suitable period of time before and after the effect. There are several suggestions of external effects on human skin that could be used to study their affects on vasomotion such as: cooling the skin, external pressure, and effect of iontophoretically delivered vasoactive substances, such as: acetylcholine and sodium nitroprusside.

Appendix A: MatLab Images Processing toolbox

MatLab is an interactive environment which includes a high-level programming language that can be used for computationally intensive tasks. In particular, this language is designed for fast numerical matrix calculations. The basic data structure in MatLab is the array, an ordered set of real or complex elements. In case of images, the data is stored as two-dimensional arrays, where each element of the array or matrix corresponds to a single pixel in the displayed image. For example, an image composed of 500 rows and 512 columns of different colored dots would be stored as a 500-by-512 matrix. This convention makes working with images in MatLab similar to working with any other type of matrix data making the full computational ability of MatLab available for image processing applications.

The Image Processing Toolbox provides a comprehensive set of standard algorithms and graphical tools for image processing, analysis, visualization, and algorithm development. The core package comes with several functions that can be used to load, save, and perform custom functions on images. Moreover, it allows several manipulations such as [98]:

- Exploring an image, examining regions of pixels.
- Direct visualization of images in MatLab window.

- Detecting and measurement of features, analysis of shapes and textures.
- Filtering and fast convolution.
- Adjustment of the contrast, and the color balance.
- creation of contours.
- Tools to create and Play movies.

and many others.

However, it is often necessary to perform more complicated operations on images to achieve the main goal. Therefore, in this work some functions were added together to reach the aim of the research. In the next sections, I will introduce in details all of the functions that were applied in my analysis of the data.

A-1: Display an image

To display the image in the MatLab window:

1. An image from a graphics file is read by using the *imread* command:
   I=*imread*('*image name.image format*');
   This image I can be logical or a nonsparse numeric array of any class and dimension.

2. The filter F of the multidimensional array I with the multidimensional filter H is applied to clear the output of image before displaying the image:
   H=ones$(5,5)/25$;
   F=imfilter(I,H);
   Each element of the output F is computed using double-precision floating point. If I is an integer or logical array, then output elements that exceed the range of the integer type are truncated, and fractional values are rounded.

3. An interactive crop image tool associated with the image displayed in the current figure is used to specify the area of interest:
   C=imcrop(F, [$xmin$ $ymin$ $width$ $height$]);
   This function crops the image I in a four element position vector [$xmin$ $ymin$ $width$ $height$] that specifies the size and position of the crop rectangle.

4. Before displaying the image, the input of the coordinator image is set by identifying the two real parameters. $'Udata'$ and $'Vdata'$ specify the spatial location of the output image C in the 2-D output space $X - Y$. The two elements of $'Udata'$ give the x-coordinates (horizontal) of the first and last columns of C, respectively. The two elements of $'Vdata'$ give the y-coordinates (vertical) of the first and last rows of C, respectively:
   $Udata$= [$xmin$ $xmax$]; $Vdata$= [$ymin$ $ymax$];

5. Finally, to display the image, we use *imshow* command. However, to define the output image properties (the color, the font (size, name), the dimensions, the title, the labels and the axis), we add the *image* function to this command:
   $imshow(C)$;
   $image(C$, 'XData', $Udata$, $'YData'$, $Vdata)$, colormap(copper);
   set(gca, 'FontName', '...', 'fontsize', ...);
   xlabel($'mm'$, 'FontName', '...', 'fontsize', ...);
   ylabel($'mm'$, 'FontName', '...', 'fontsize', ...);
   title('write the title of the image');

A-2: Measure the distance

For measuring the distance between two pixels (two points):

1. Display an image in the Image Tool by using *imtool* command.
   $imtool('image\ name.image\ format')$ or $imtool(I)$

2. Use the Distance tool from the Image Tool toolbar or the Tools menu. The Distance tool displays the Euclidean distance between any two selected endpoints of the line in a label superimposed over the line. The distance in data units is determined in pixels.

3. Alternatively, open a figure window using *imshow* and then call *imdistline*. The Distance tool appears as a horizontal line, which can be easily repositioned or resized to display over any measured subject on the image.

4. The units of the distance can be easily converted from pixels to mm as the size of displayed image is $2mm \times 1.2mm$ or 500 pixel$\times$ 512 pixel. So, the X distance and the Y distance in mm are:
   $X(mm) = (X(pixels) \times 2mm)/500$
   $Y(mm) = (Y(pixels) \times 1.2mm)/512$

A-3: Define the intensity by depth:

To define the intensity or the pixel value of cross-sections along line segments, the $improfile$ function is applied to compute the intensity values in an image. In more details, the intensity value for each point can be found by using the following command:

$$P = improfile(I, x, y)$$

P displays the intensity values among specific width window and at certain selected depth. x and y are the length vectors specifying the spatial coordinates of the endpoints of the line segments.
$x = [xmin \quad xmax]$; this is the width of the window that we are looking for the intensity values into it.
$y = [y1 \quad y1]$; $y1$ is the particular depth that is being studied.

A-4: Plot several intensity changes by depth:

To plot several intensity changes by depth, the same previous steps are applied to several images to create several arrays. However, there is a small change in the range of x, which will be for just at one single point between $xmin$ and $xmax$.

Then, all arrays can be easily plotted in the same figure by using this command:
$Plot(x1, y1, ...)$;
this function plots all lines defined by the xn, yn pairs,
where xn is the depth of any selected pixel point from the surface of the image and in this case $x1 = x2 = ...$,
yn is the intensity values for n number of subjects.

A-5: Apply the correction factor to the image

To apply the calculated correction factor to the image and then generated the modified image, these steps have been followed:

1. Open a new array, which has the same dimensions as the matrix of the image.
   $J = zeros(x, y)$; In a general case and before cropping the image, the x= 500 (number of columns) and y=512 (number of rows).

2. Write the loop function that works on all elements of the matrix to correct the intensity values:
   for $n = 1 : x$
   for $m = 1 : y$
   $J(n, m) = I(n, m) + (n - 1) \times slope$;
   end
   end
   where n is the number of the columns in x coordinate, and m is the number

of the rows in y coordinate.

3. Convert the obtained matrix from double array to image style; the following command is used in this case:
   $J1 = uint8(round(J - 1));$

4. Adjust and increase the contrast of the output image by using this function:
   $M = imadjust(J1, stretchlim(J1), []);$

5. Use imshow(M) to display the corrected intensity images.

A-6: Define the contour function

To create a contour plot of image data, the *imcontour* command is used. This command draws a contour plot of the image I, automatically setting up the axes so their orientation and aspect ratio match the image. The values of the contour are chosen automatically based on the mean value of the minimum and the maximum values of the matrix elements for the image I. This process can be easily understood by defining the pixel values of the cross sectional image, which can be specified by using $improfile(I)$ command. The mean values of the intensity can then be mathematically identified.

In this research, the command of $imcontour(I, n)$ is used to draw the contour plot of selected image I with n contour level. Where n is the number of equally spaced contour levels in the plot, and is fixed as n=1 in this work.

A-7: Calculate the area of the contour

To calculate the area of the contour, the number of the pixels inside the contour should be counted. As this step is difficult to calculate, several steps have been applied.

1. Convert the grayscale cropped and corrected of intensity image M to a binary image. The output image BW replaces all pixels in the input image with luminance greater than level or equal to 1 (white) and replaces all other pixels with the value 0 (black). This conversion is applied to the image by using $BW = im2bw(M)$ command.

2. Apply the contour function to the binary image BW.
   $imcontour(BW, 1)$

3. Now, the area of the contour can be easily calculated by counting all the zeros pixel in the image $Area.vessel$= sum($\sim BW$).
   This area is presented roughly, and might not match exactly with the area of the contour in the real image because different patterns of pixels are weighted differently.

4. As the calculated area is in pixels, a conversion is applied to obtain the area in mm^2 as has been explained before.

In this research, I used several commands as a first step to introduce all sequence images in the folder, and to locate all these images under the same file, and then to count all the images in the located file.

$dirOutput = dir('*.bmp');$
$fileNames = dirOutput.name;$
$numFrames = numel(fileNames);$

Afterwards, a new array is containing the same number of elements as the number of images and is opened and following loop commands are applied to all frame images in the file from 1 (the first image) to the last image (which has the same number of the images in the file) by using all previous explained steps:

$Area.vessel = zeros(numberofimages, 1);$

$for\ p = 1 : numFrames$

$I = imread(fileNames\{p\});$

$H = ones(5, 5)/25;$

$F = imfilter(I, H);$

$C = imcrop(F, xmin\ \ ymin\ \ x - width\ \ y - height]);$

$J = zeros(x - width, y - height);$

$for\ n = 1 : x - width;$

$for\ m = 1 : y - height;$

$J(n, m) = C(n, m) + (n - 1) \times slope;$

end

end

$J1 = uint8(round(J - 1));$

$M = imadjust(J1, stretchlim(J1), []);$

$BWI = im2bw(M);$

$Vessel = imcrop(BW1, [The\ size\ of\ the\ rectanagule\ around\ the\ selected\ vessel]);$

$Area.vessel(p) = sum(sum(\sim Vessel));$

end

The final step is to plot the area of the contours in time by using $plot(Area.vessel(p))$ command.

A-8: Montage images

To view multiple frames in a multiframe array at one time, the montage function is used. The command $montage(filename, param1, value1, param2, value2, ...)$ displays all the image frames, arranging them into a rectangular grid. This view depends on the values of the optional parameter/value pairs. There are three main parameters in the montage function, which are: DisplayRange, size, and

indices. Each parameter can be functioned as follow:

1- DisplayRange controls the display range of each image in a grayscale sequence by the vector [low high] intensity.

2- Indices is a numeric array specifying which frames to display in the montage [from any selected frame: another one], where (:) means (to) in the MatLab commands.

3- Size is specifying the number of rows and number of columns in the montage [rows columns].

For example in my work the details of montage function that I used is:

$montage(fileNames,'Size',[88],'indices',[1:64],'DisplayRange',[]);$

$axisnormal; colormap('hsv');$

A-9: Create a movie

To create a movie from a sequence recorded images by using MatLab images processing, the following steps is followed:

1. Create an avi file object, giving it the name specified in filename by using the command $[mov = avifile(filename)]$.
2. Select a parameter of the compression of the movie $[mov \cdot compression =' None']$.
3. Choose the speed of playing recorded movie, which in this case I selected to be 8 as in the speed of recording the data $[mov \cdot fps = 8]$.
4. Then use the previous loop function to read all images in the folder and apply the same treatment apply the same treatment as before.
5. After that use the *print* command to copy the displayed figure to the system clipboard in any selected format. In this work, JPG format image is selected

because it has a less size compared to others without the loss of the quality of the image.

6. Use the *addfram* command to append the data in frame to the avi file identified by *mov*, which was created by a previous call to *avifile*.

7. Then apply *delete* command to delete the named file from the disk.

8. Close the *mov* after adding the last frame of printed image

In this research, the following commands are used together to create a movie:

$dirOutput = dir('*.bmp');$

$fileNames = dirOutput.name;$

$numFrames = numel(fileNames);$

$mov = avifile('name\ of\ the\ movie.avi');$

$mov \cdot compression =' None';$

$mov \cdot fps = 1;$

$for\ p = 1 : numFrames$

$I = imread(fileNames\{p\});$

$H = ones(5,5)/25;$

$F = imfilter(I, H);$

$C = imcrop(F, xmin\ \ ymin\ \ width\ \ height]);$

$J = zeros(width, height);$

$for\ n = 1 : width$

$for\ m = 1 : height$

$J(n,m) = C(n,m) + (n-1) \times slope;$

end

end

$J1 = uint8(round(J-1));$

$M = imadjust(J1, stretchlim(J1), []);$

$Udata = [xmin \quad xmax]; \; Vdata = [ymin \quad ymax];$

$imshow(M);$

$image(M,'XData', Udata,'YData', Vdata), \; colormap(copper);$

$set(gca,'FontName','...','fontsize',...);$

$xlabel('mm','FontName','...','fontsize',...);$

$ylabel('mm','FontName','...','fontsize',...);$

$title('write\ the\ title');$

$print('-djpeg',['M'num2str(p)'.djpeg'])$

$mov = addframe(mov, imread(['M'num2str(p)'.djpeg']));$

$delete(['M'num2str(p)'.djpeg'])$

end

$mov = close(mov);$

A-10: Fourier transform

1- Introduction:

The Fourier transform is the technique that has been used to detect oscillatory components in the signals by using following equation [23]:

$$\hat{g}(f) = \int_{-\infty}^{\infty} g(u)e^{-2\pi it}du. \tag{1}$$

where g(u) is the original signal that can be reconstructed by using inverse Fourier transform,

$$g(u) = \int_{-\infty}^{\infty} \hat{g}(f)e^{2\pi it}df. \tag{2}$$

From Plancherel's theorem and Parseval's theorem, the energy of the signal is equivalent to the total energy in the frequency domain and it can be defined as:

$$E_{tot} = \| g \|^2 = \| \hat{g} \|^2 = \int_{-\infty}^{\infty} |\hat{g}(f)|^2 df = \int_{-\infty}^{\infty} |g(u)|^2 du. \tag{3}$$

As the Fourier transform cannot deal with properties that are local in time, the short time Fourier transform (STFT) has been introduced to overcome with this

problem. A window $\omega(u)$ of fixed length is shifted along time t to obtain the local information around t. The original signal $g(u)$ can be obtained from

$$\hat{g}(f,t) = \int_{-\infty}^{\infty} \omega(u-t)g(u)e^{2\pi it}du. \tag{4}$$

In this case, the original signal is reconstructed as:

$$\hat{g}(u) = \frac{1}{2\pi \parallel \omega^2 \parallel} \int_{-\infty}^{\infty} dt \int_{-\infty}^{\infty} \hat{g}(f,t)\omega(u-t)e^{2\pi it}df. \tag{5}$$

As has been identified from equation(3), the energy can be expressed as:

$$E_{tot} = \parallel g \parallel^2 = \frac{1}{\parallel \omega^2 \parallel} \int_{-\infty}^{\infty} \int_{-\infty}^{\infty} |\hat{g}(f,t)|^2 df\, dt. \tag{6}$$

where $\parallel \omega^2 \parallel = \int_{-\infty}^{\infty} |\omega(t)|^2 dt$.

In this case, an uncertainty principle is used to emphasize the accuracy of localization in time, and frequency resolution, which states:

$$\Delta_t \Delta_f \geq \frac{1}{4\pi}. \tag{7}$$

where Δ_t and Δ_f are determined by:

$$\Delta_t^2 \equiv \frac{1}{\parallel \omega \parallel} \int_{-\infty}^{\infty} |\omega(t)|^2 (t-t_*)^2 dt, \tag{8}$$

$$\Delta_f^2 \equiv \frac{1}{\parallel \hat{\omega} \parallel} \int_{-\infty}^{\infty} |\omega(f)|^2 (f-f_*)^2 df. \tag{9}$$

and t_*, f_* are states as:

$$t_* \equiv \frac{1}{\parallel \omega \parallel} \int_{-\infty}^{\infty} |\omega(t)|^2 t dt, \tag{10}$$

$$f_* \equiv \frac{1}{\parallel \hat{\omega} \parallel} \int_{-\infty}^{\infty} |\omega(f)|^2 f df. \tag{11}$$

This uncertainty principle states that a narrow window should be used to gain good time resolution; however, this will provide a poor frequency resolution as the detection of low frequencies requires a wide window. Therefore, the discrete Fourier transform (DFT) is used in this case because it reveals periodicity in input

data as well as the relative strengths of any periodic components. The (DFT) is an extremely useful function which can be applied to real signals as follows:

$$G(f_k) = \sum_{j=0}^{N-1} g(jt_s)e^{-2\pi ijk/N}. \tag{12}$$

jt_s are the discrete points, where j= 0, 1,..., N-1.

N is equal to [T(the length of the signal)/t_s(the length of the discrete window)].

k is equal to [f_k (the discrete frequency)$*T$], where k= 0, 1,..., N-1.

The frequency resolution in this case is determined by the length of the signal as $\Delta_f = 1/T$ and the upper frequency limit is $f_{max}= t_s/2$.

2- MatLab code to calculate Fourier transform:

The MatLab commands that have been used to calculate Fourier transform are:

1. Create a new array sig by subtracting the mean value of the data from the original signal to remove any trend from the plot.
   $sig = Area \cdot Vessel - mean(Area \cdot Vessel)$.

2. Define the number of the images per second to sample the frequency of the continuous signal to make a time series consisting of a sequence of samples.
   $sampling\_freq = 8$.

3. In order to apply Fourier transform to real signal, we suppose that the original signal has a finite window length and it is sampled at the discrete point of the data with frequency resolution determined by the length of the signal.
   $f = sampling\_freq * (0 : ((length(sig))/2))/(length(sig))$.

4. Compute the two dimensional signal with a fast Fourier transform by writing $fft2(sig)$ command.

5. Calculate the power spectrum, which is a measurement of the power at various frequencies.

$Pyy = Y.^{*}conj(Y)/length(sig)$. Where $conj(Y)$ returns the complex conjugate of the elements of Y.

6. The final plot Fourier transform of the signal is applied by using *plot* command.

By using all previous steps of calculation, the following command has been used to present the results in the figure (4.11) and figure(4.12):

$sig = Area \cdot Vessel - mean(Area \cdot Vessel);$

$sampling\_freq = 8;$

$Y = fft2(sig);$

$Pyy = Y.^{*}conj(Y)/length(sig);$

$f = sampling\_freq * (0 : ((length(sig))/2))/(length(sig));$

$plot(f, Pyy(1 : ((length(sig))/2) + 1))$

$set(gca,'xscale','log');$

$title('Frequency\ content\ of\ signal')$

$xlabel('frequency\ (Hz)')$

A-11: Wavelet transform

1- Introduction

A wavelet is an oscillating function localized in time by an envelop of unite width. The transform is obtained by convolving the signal with the Morlet mother wavelet function to provide the frequency component information of a signal with time. This method is used for analyzing the signal because the inverse relationship between the frequency and the scale, $f = 1/s$ allows simple conversion to the frequency scale. In addition, it gives the optimal time resolution for low and high frequencies within previous uncertainty principle. This transform can be written

as:

$$\psi(u) = \frac{1}{\sqrt{\pi}} e^{-iu} e^{\frac{-u^2}{2}}. \tag{13}$$

This is scaled (stretched and compressed) by some factor s and a center time t by following equation:

$$\psi_{s,t}(u) = \mid s \mid^{-1/2} \psi(\frac{u-t}{s}). \tag{14}$$

In order to create wavelets that are applied in time to the original signal, The wavelet transform is introduced as a convolution of the wavelet and the time series:

$$\tilde{g}(s,t) = \int_{-\infty}^{\infty} \bar{\psi}_{s,t}(u) g(u) du, \tag{15}$$

where $\bar{\psi}$ represents the complex conjugate of ψ Hence, for every wavelet at each moment in time a coefficient is obtained, representing the strength of correlation between wavelet and the original signal. Thus a high coefficient for a small-scale wavelet at a given moment in time corresponds to the presence of a high frequency component at that time.

The total energy of the signal $g(u)$ can be calculated as:

$$E_{tot} = \| g \| = C^{-1} \int_{-\infty}^{\infty} \int_{-\infty}^{\infty} \frac{1}{s^2} |\tilde{g}(s,t)|^2 ds dt. \tag{16}$$

where the constant C is determined by the shape of the wavelet. Therefore,

$$C^{-1} S^{-2} \mid \tilde{g}(s,t) \mid^2 \tag{17}$$

can be interpreted as the energy density of the signal in the time scale plane [23].

2- MatLab code to calculate wavelet transform

In this research, several MatLab commands are used in order to find out the wavelet transform of the signal, and to obtain the time resolution for all of the frequencies band that have been presented in the figures (4.13), (4.14), (4.15), (4.16), (5.3), (5.4) and figure(5.5). In steps, the commands are:

1. Introduce the new array for the signal time series $[t\_series = sig]$.

2. Sampling the frequency of the signal to the frequency which the data was recorded at.

   $sampling\_freq = 8.$

3. Use several parameters to control the wavelet function such as:

   - Identify the value of sampling frequency.

     $parameters.sig\_sampl\_freq = sampling\_freq.$

   - Control the start of the signal by 0 value.

     $parameters.sig\_t\_start = 0.$

   - Control the end time of the signal by the length of the signal divided by sampling the frequency.

     $parameters.sig\_t\_fin = length(t\_series)/parameters.sig\_sampl\_freq.$

   - Set the minimum frequency as 0.125 (1/8) Hz and the maximum frequency as 200 Hz.

     $parameters.scale\_min = 0.125;\ parameters.scale\_max = 112.5.$

   - Set the incremental multiplier of the scale as 1.05.

     $parameters.sigma = 1.05.$

   - Select the central frequency of the signal to be 1.

     $central\_frequency = 1.$

4. Then define the wavelet transform function by applying this command $[wavelet\_fft(t\_series, parameters)]$.

5. Finally plot the figure as axis of handle $time\_1/60$ instead of the current axis by using the *mesh* command.

   $figure, mesh(time\_1/60, fr\_1, abs(w\_transform(2:end, 2:end)));$

   $title('wavelettransform'); ylabel('Frequency(Hz)').$

   where $w\_transform = wavelet\_fft(t\_series, parameters),$

   $time\_1 = w\_transform(1, 2:end),$

$scale\_1 = w\_transform(2 : end, 1)$

and $fr\_1 = central\_frequency./scale\_1$.

Appendix B: Create 3D images by using Image J

ImageJ is a public domain Java image processing program, which can display, edit, analyze, process, save and print images. It can read many image formats including TIFF, GIF, JPEG, BMP, DICOM, FITS and raw. It supports stacks, a series of images that share a single window. Moreover, it allows several manipulations such as [99]:

- Calculate of the area and pixel value statistics of user-defined selections.
- Creation of density histograms and line profile plots.
- Support for standard image processing functions such as contrast manipulation, sharpening, smoothing, edge detection and median filtering.
- Allow some geometric transformations such as scaling, rotation and flips. Images can be zoomed up to 32:1 and down to 1:32.
- Recoded a 3D images for a set of images.
- Creation a movie for a set of images.

Create 3D images

In order to create a 3D view of a sequence of images recorded using imageJ:

1. Open a file in the ImageJ program and then import image sequence in the stored folder, which should have a folder with sequential image files.

2. The images from the folder are now opened up within ImageJ as a stack of images.

3. To make a 3D view, select *'3D'* under Plugging tool section. This section counts the number of 3D objects in a stack and can display the volume, the interactive 3D surface, and stack 3D surface plot.

4. After selecting 3D viewer, the 3D image is created in a new window and the view of the cross section can be easily adjusted by selecting Edit from the new window and then choosing attributes to adjust the view to any specific point and within each coordinator.

Appendix C: The The area vibrations of Phantom and vessel

This DvD contains the same two movies of comparing the area vibrations of Phantom with the vessel in different speeds. One of them is in 8 frames in second as the speed of recording the data and the another one is in speed of 1 frame per second to shows clearly and slowly the vibrations of theses areas.

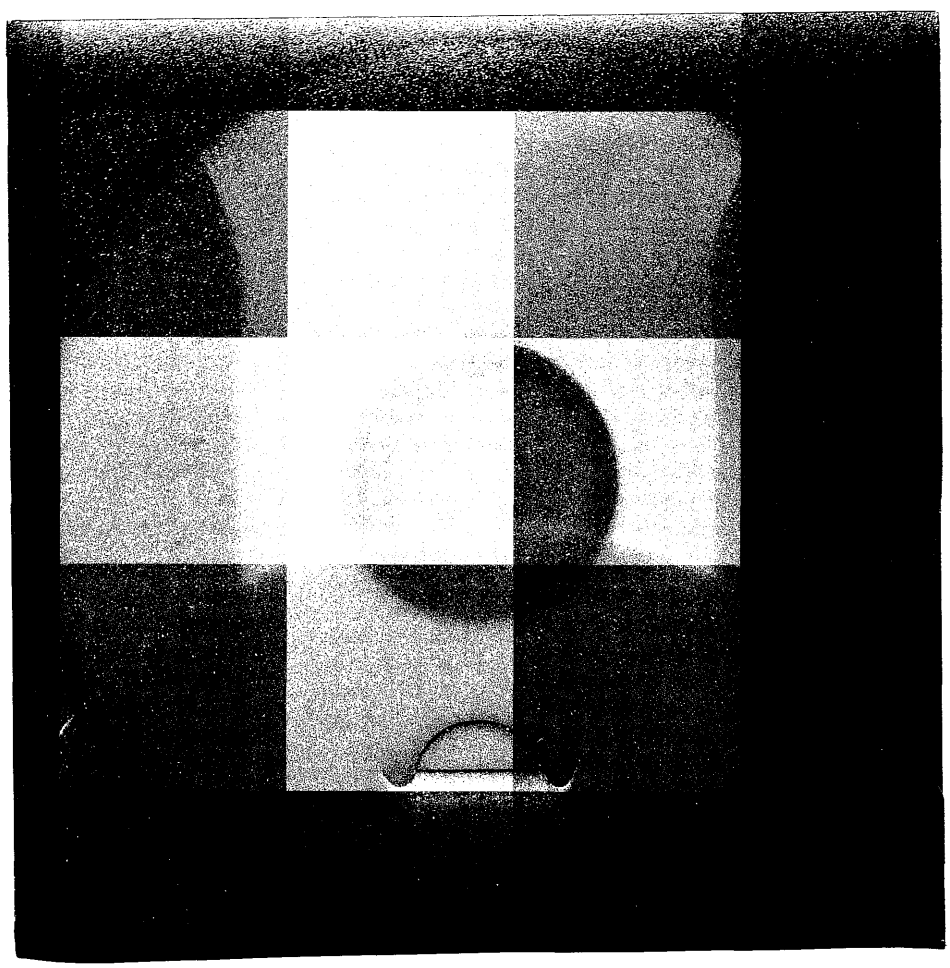

Bibliography

[1] R. Taggart, *Animals: Structure and Function*, McGraw-Hill Ryerson Ltd, Canada, 12:476, 2010.

[2] T. J, Gerard, B. H. Tortora, *Principles of anatomy and physiology*, Wiley John and Sons, New York, USA 9: 733, 2000.

[3] W. J. Germann, C.L.Stanfield,*Principles of Human Physiology*, Benjamin Cummings, San Francisco, CA, 2002.

[4] W. J. Cliff, *Blood vessels*, Cambridge university, Cambridge, 1976.

[5] J. A. Tuszynski Michal Kurzynski, *Introduction to molecular biophysics*, CRC Press LLC, Florida, 2003.

[6] G. Houghton, *Blood: The Circulatory System*, The Rosen Bublishing Group, Nwe York, USA, 1:5, 2007.

[7] A. Lin, Q. Jia , and W. Ruikang , *Ultrahigh sensitive optical microangiography for in vivo imaging of microcirculations within human skin tissue beds*, Optics Express, 18(8): 8220-8228, 2010.

[8] D. M. Hudson, *Human Anatomy Physiology*, Weston Walch, USA, 2006

[9] K. C. Madison, *Barrier function of the skin of the epidermis*, J Invest Dermatol, 121(2):231-41, 2003.

[10] M. Richardson, *Understanding the structure and function of the skin*, Nurse Times, 99(31):46-8, 2003.

[11] J. A. A. Huunter, J. A. Savin, and M. V. Dahl, *Clinical dermatology*, Blackwell science Ltd, Oxford, UK, 1989.

[12] P. F. Millington, R. Wilkinson, *Skin*, Cambridge University, Cambridge, 1983.

[13] M. Khazaei, F. Moien-afshari, and I. Laher, *Vascular endothelial function in health and diseases*, Pathophysiology, 15: 49-67, 2008.

[14] D. Shier, J. Butler and R. Lewis, *Hole's Human Anatomy and Physiology*, McGraw Hill, New York, USA, 8: 160-183, 1999.

[15] Antranik, Anatomy (Science), *Types of blood vessels*, retrieved from: http://antranik.org/blood-vessels/, last accessed: 3-12-12.

[16] M. Rossi, A. Carpi, F. Galetta, F. Franzoni, G. Santoro, *Skin vasomotion investigation: a useful tool for clinical evaluation of microvascular endothelial function?*, Biomed Pharmacother, 62(8): 541-556, 2008.

[17] C Aalkjær , D. Boedtkjer and V. Matchkov, *Vasomotion: what is currently thought?*, Acta Physiol, 202: 253-269, 2011.

[18] J. C. Arcieor and T. W. Secomb, *Spontaneous oscillations in a model for active control of microvessel diameters*, Mathematical Medicine and Biology, 1:18, 2011.

[19] D. B. Cines, E. S. Pollak, C.A. Buck, J. Loscalzo, G. A. Zimmerman, R. P. McEver, J. S. Pober, T. M. Wick, B. A. Konkle, B. S. Schwartz, E. S. Barnathan, K. R. McCrae, B. A. Hug, A. S., and D. M. Stern, *Endothelial Cells in Physiology and in the Pathophysiology of Vascular Disorders*, the Journal of The American Society of Hematology, 91(10): 3527-3561, 1998.

[20] M. Koenigsberger, R. Sauser, D. Seppey, J. Bèny, *Calcium dynamics and vasomotion in arteries subject to isometric, isobaric, and isotonic conditions*, Biophys Journal, 95(6): 2728-2738, 2008.

[21] R.L. Matz and R. Andriantsitohaina, *Age-related endothelial dysfunction, Drugs Aging*, 20: 527-550, 2003.

[22] B. E. Sumpio, J. T. Riley and A. T. Dardik, *Cells in focus: endothelial cell*, J Biochem Cell Biol., 34(12): 1508-1512, 2002.

[23] Y. Shiogai, A. Stefanovska, and P. V. E. McClintock, *Nonlinear dynamics of cardiovascular ageing*, Physics Reports, 488: 51-110, 2010.

[24] H. Nilsson, C. Aalkjaer, *Vasomotion: mechanisms and physiological importance*, Mol Interv, 3(2): 79-89, 2003.

[25] M. Koenigsberger, R. Sauser, J.Bény and J. Meiste, *Role of the endothelium on arterial vasomotion*, Biophysical Journal, 88(6): 3845-3854, 2005.

[26] R. Zhang, W. Verkruysse, B. Choi, J. A. Viator, B. Jung, L. O. Svaasand, G. Aguilar, J. S. Nelson, *Determination of human skin optical properties from spectrophotometric measurements based on optimization by genetic algorithms*, Journal of Biomedical Optics, 10(2): 024030, 2005.

[27] X. Ma, *Study of optical properties of skin tissues from ultraviolet to short wave infrared*, PhD thesis, Biomedical Physics, the Faculty of the Department of Physics East Carolina University, 2004.

[28] A. N. Bashkatov, E. A. Genina, V. I. Kochubey and V. V. Tuchin, *Optical properties of human skin, subcutaneous and mucous tissues in the wavelength range from 400 to 2000 nm*, Appl Phys, 38: 2543-2555, 2005.

[29] R. R. Anderson, B.S and J. A. Parrish, *The optics of human skin*, Journal of Investigative Dermatology, 77: 13-19, 1981.

[30] T. Igarashi, K. Nishino, and S.K. Nayar, *The appearance of human skin*, Technical Report, Department of Computer Science, Columbia University, New York, USA, 2005

[31] T. L. Troy and S. N. Thennadil, *Optical properties of human skin in the NIR wavelength range of 1000-2200 nm*, J Biomed Opt, 6: 167-176, 2001.

[32] K. S. Bersha, *Spectral imaging and analysis of human skin*, Master Thesis Report, University of Eastern Finland, 2010

[33] K. P. Nielsen, L. Zhao, J. J. Stamnes, K. Stamnes, J. Moan, *The optics of human skin: aspects important for human health*, The Norvegian Academy of Science and Letters, Oslo, 35-46, 2008.

[34] M. Makale, *Noninvasive imaging of blood vessels*, Methods in Enzymology, 444(8): 175-199, 2008.

[35] Y. Jia, P. Li, RK. Wang, *Optical microangiography provides an ability to monitor responses of cerebral microcirculation to hypoxia and hyperoxia in mice*, J Biomed Opt, 16(9): 096019, 2011.

[36] J. Callerame, *X-Ray backscater imaging: photography trough barriers*, American Science & Engineering, Billerica, USA, 13-20, 2006.

[37] D. Attwood, *Soft X-rays and extreme ultraviolet radiation*, Cambridge University Press, UK, 1999.

[38] A. F. Kopp, K. Klingenbeck-Regn, M. Heuschmid, A. Küttner, B. Ohnesorge, T. Flohr, S. Schaller, C. D. Claussen, *Multislice Computed Tomography: Basic Principles and Clinical Applications*, Electromedica, 68(2): 94-105, 2000.

[39] R. Luypaert , S. Boujraf, S. Sourbron, M. Osteaux, *Diffusion and perfusion MRI: basic physics*, European Journal of Radiology, 38: 19-27, 2001.

[40] W. H. Faulkner, *Tech's Guide to MRI: Basic Physics, Instrumentation and Quality Control*, Malden: Blackwell Science, 2001.

[41] B. Pollet, *Bruno Pollet Power Ultrasound in Electrochemistry: From Versatile Laboratory Tool to Engineering Solution*, John Wiley and Sons, Canada, 2012.

[42] E. M. C. Hillman, C. B. Amoozegar, T. Wang, A. F. H. McCaslin, M. B. Bouchard, J. Mansfield and R. M. Levenson, *In vivo optical imaging and dynamic contrast methods for biomedical research*, The Royal Society, 369: 4620-4643, 2011.

[43] M. Maddah, H. Soltanian-Zadeh, A. Afzali-Kusha A, A. Shahrokni, Z.G.Zhang, *Three-dimensional analysis of complex branching vessels in confocal microscopy images*, Comput Med Imaging Graph, 29(6): 487-98, 2005.

[44] M, Zandvoort, W. Engels, K. Douma, L. Beckers, M. Egbrink, M. Daemen, and D. Slaaf, *Two-photon microscopy for imaging of the (Atherosclerotic) vascular wall: a proof of concept study*, Journal of Vascaular Research, 41: 54-63, 2004.

[45] W. Groner, J. W. Winkelman, A. G. Harris, C. Ince, G. J. Bouma, K. Messmer, and R. G. Nadeau, *Orthogonal polarization spectral imaging: a new method for study of the microcirculation*, Nature Medicine, 5: 1209-1212, 1999.

[46] A. F. Fercher, W. Drexler, C. K. Hitzenberger and T. Lasser, *Optical coherence tomography- principles and applications*, Reports on Progress in Physics, 66(2): 239-303, 2003.

[47] T. Vo-Dinh, *Raman Spectroscopy*, Biomedical Photonics, CRC Press, USA, (30): 750, 2003.

[48] T. Baks, F. Cademartiri, A. D. Moelker, A. C. Weustink, R. Geuns, N. R. Mollet, G. P. Krestin, D. J. Duncker, P. J. de Feyter, *Multislice computed tomography and magnetic resonance imaging for the assessment of reper-*

fused acute myocardial infarction free, Journal of the American College of the Cardiology, 48(1): 144-152, 2006.

[49] P. N. Wells, *Ultrasonic imaging of the human body*, Report of Progressing in Physics, 62: 671-722, 1999.

[50] Illinois, *Optical Coherence Tomography*, retrieved from: http://otm.illinois.edu/sites/all/files/files/optical-coherence-tomography.pdf, last accessed: 30-11-2012.

[51] A. R. Kherlopian, T. Song, Q. Duan, M. A Neimark, M. J. Po, J. K. Gohagan and A. F. Laine, *A review of imaging techniques for systems biology*, BMC Systems Biology, 2(74): 1-18, 2008.

[52] A. Forsea, E. M. Carstea, L. Ghervase, C. Giurcaneanu, and G. Pavelescu, *Clinical application of optical coherence tomography for the imaging of non-melanocytic cutaneous tumors: a pilot multi-modal study*, Journal of Medicine and Life, 3(4): 381-389, 2010.

[53] S. A. Boppart, W. Luo, D. L. Marks, and K. W. Singletary, *Optical coherence tomography: feasibility for basic research and image-guided surgery of breast cancer*, Cancer Research and Treatment, 84: 85-97, 2004.

[54] J. G. Fujimoto, *Optical coherence tomography*, 2(4): 1099-1111, 2001.

[55] L. Langevin, D. Gay, and M. Piché, *Spatial Domain Optical Coherence Tomography*, Proceedings of SPIE, 7099, 2008.

[56] J. G. Fujimoto, C.Pitris, S. A. Boppart, and M. E. Brezinski, *Optical Coherence Tomography: An Emerging Technology for Biomedical Imaging and Optical Biopsy*, Neoplasia, 2(1): 9-25, 2000.

[57] D. Huang, E. A. Swanson EA, C. P. Lin, J. S. Schuman, et al. *Optical coherence tomography*, Science, 254: 1178-118, 1991.

[58] A. G. Podoleanu, *Optical coherence tomography*, British Journal of Radiology, 78: 976-988, 2005.

[59] H. W. Lim, N. A. Sotter, *Clinical photomedicine*, Marcel Dekker, New York, 1993.

[60] B. Baumann, S. O. Baumann, T. Konegger, M. Pircher, E. Götzinger, F. Schlanitz, C. Schütze, H. Sattmann, M. Litschauer, U. Erfurth, and C. K. Hitzenberger, *Polarization sensitive optical coherence tomography of melanin provides intrinsic contrast based on depolarization*, Biomedical Optics Express, 3(7): 1670-1683, 2012.

[61] F. Fercher, W. Drexler, C. K. Hitzenberger and T. Lasser, *Optical coherence tomography - principles and applications*, Reports on Progress in Physics, 66 (2): 239-303, 2003.

[62] M. A. Choma, M. V. Sarunic, C. Yang, and J. A. Izatt, *Sensitivity advantage of swept source and Fourier domain optical coherence tomography*, Optical Express, 11: 2183-21899, 2003.

[63] M. Bail, G. Häusler, J. M. Herrmann, M. W. Lindner, and R. Ringler, *Optical coherence tomography with the Spectral Radar-Fast optical analysis in volume scatterers by short coherence interferometry*, Optics Letters, 21(14): 1087-1089, 1996.

[64] MA. Choma, K. Hsu and JA. Izatt, *Swept source optical coherence tomography using an all-fiber 1300-nm ring laser source*, Biomedical Optics, 10(4):044009, 2005.

[65] Optical Coherence Tomography, *Spectral Radar Optical Coherence Tomography*, retrieved from: http://www.thorlabs.com/Images/PDF/Vol18528-531.pdf, last accessed: 30-11-2012.

[66] P. H.Tomlins, R. K. Wang, *Theory developments and applications of optical coherence tomography*, Journal of physcis and applied physics, 38:2519-2535, 2005.

[67] J.A. Izatt and M.A. Choma, *Optical Coherence Tomography: Technology and Applications*, W. Drexler and J.G. Fujimoto, Eds., Springer, 2008.

[68] M. A. Choma, M. V. Sarunic, C. Yang, and J. A. Izatt, *Sensitivity advantage of swept source and Fourier domain optical coherence tomography*, Optics Express, 11(18): 2183-2189, 2003.

[69] B. W. Pogue, M. S. Patterson, *Review of tissue simulating phantoms for optical spectroscopy, imaging and dosimetry*, Journal of Biomedical Optics, 11(4): 041102, 2006.

[70] M. Lualdi, A. Colombo, B. Farina, S. Tomatis, and R. Marchesini, *A phantom with tissue-like optical properties in the visible and near infrared for use in photomedicine*, Lasers in Surgery and Medicine, 28:237-243, 2001.

[71] Archived drug label, *Intralipid 20 %*, retrieved from: http://dailymed.nlm.nih.gov/dailymed/archives/, last acceced: 2-12-2012.

[72] D. Irwin, *Infulance of tissue absorption and scattering on diffuse correlation spectroscopy blood flow measurement*, Master Thesis, University of Kentucky, USA, 2011

[73] J. Henshall, *Book of the Black Bass*, The Robert Clarke company, 1881.

[74] C. Preininger, A. Mencaglia, F. Baldini, *Polymer-coated optical fibres for application in a direct evanescent wave immunoassay*, Analytica Chimica Acta, 403(1-2): 67-76, 2000.

[75] S. T. Flock, S. L. Jacques, B. C. Wilson, W. M. Star, and M. J.C. van Gemert, *Optical properties of intralipid: A phantom medium for light propagation studies*, Lasers in Surgery and Medicine, 12: 516-519, 1992.

[76] Medical expo, *Elbow joint anatomical model (with blood vessels)*, retrieved from: http://www.medicalexpo.com/medical-manufacturer/joint-anatomical-model-1576.html, last accesed: 30-11-2012.

[77] L. R. Allen and D. W. Mills, *Signal Analysis: Time, Frequency, Scale, and Structure*, 9: 585-586, Wiley, New York, 2004.

[78] L. W. Sheppard, V. Vuksanovic, P. V. E. McClintock and A. Stefanovska, *Oscillatory dynamics of vasoconstriction and vasodilation identified by time–localized phase coherence*, Physics in Medeicin and Biolology, 56: 3583-3601, 2011.

[79] A. Stefanovska, *Complex but Not Complicated Cardiovascular and Brain Interactions*, IEEE Engineering in Medicine and Biology magazine, 25-29, 2007.

[80] A. Bernjak, P.B.M. Clarkson, P.V.E. McClintock, and A. Stefanovska, *Low–frequency blood flow oscillations in congestive heart failure and after β1–blockade treatment*, Microvasc Res, 76(2): 224-232, 2008.

[81] Di Renzo M., G. Mancia, G. Parati, A. Pedotti, and A. Zanchetti, *Computer Analysis of Cardiovascular Signals*, IOS, Amsterdam, The Netherlands, 1995.

[82] T. Soderstrom, A. Stefanovska, M. Veber, H. Svensson, *Involvement of sympathetic nerve activity in skin blood flow oscillations in humans*, Am J Physiol Heart Circ Physiol, 284: H1638-H1646, 2003.

[83] A. Stefanovska, and P. Kroselj, *Correlation integral and frequency analysis of cardiovascular functions*, Open Sys. Inform. Dyn, 4: 457-478, 1997.

[84] R. Norman, *Wavelet contraction, waevelet expansion, and the control of seismic resolution*, Geophysics, 18(4), 1953.

[85] A. Stefanovska, M. Bracic, and H. D. Kvernmo, *Wavelet analysis of oscillations in the peripheral blood circulation measured by laser Doppler technique*, 46(10): 1230-1239, 1999.

[86] F. Irwin, et al, *Fitzpatrick's Dermatology In General Medicine*, 5(1), New York, NY: McGraw-Hill, 1999.

[87] S. Simonet, E. Bonhomme, J. N. Fabiani and T. Verbeuren, *Temperature-dependent basal tone in isolated human saphenous veins: implication of TP-receptors Fundam*, The Journal of Clinical Pharmacology, 14: 461-7, 2000.

[88] J. Kastrup, J. Buhlow, and N. A. Lassen, *Vasomotion in human skin before and after local heating recorded with laser Doppler flowmetry. A method for induction of vasomotion*, Int. J. Microcirc. Clin. Exp, 8: 205-215, 1989.

[89] P. Yuan , H.Liu , C.Chen , H.Kou , *Temperature response in biological tissue by alternating heating and cooling modalities with sinusoidal temperature oscillation on the skin*, International Communications in Heat and Mass Transfer, 35: 1091-1096, 2008.

[90] A. Lindqvist, J. Jalonen, P. Parviainen, K. Antila, L. A. Laitinen, *Effect of posture on spontaneous and thermally stimulated cardiovascular oscillations*, Cardiovascular Research, 24: 373-380, 1990.

[91] M. Lossec, B. Multon, H. Ben Ahmed and C. Goupil, *Thermoelectric generator placed on the human body: system modeling and energy conversion improvements*, The European Physical Journal of Applied Physics, 52: 11103, 2010.

[92] Y. K. Jan and F. Liao, *Synchronization of sacral skin blood flow oscillations in response to local heating*, EEE Engenerring in Medicine and Biology Society, 1753- 1756, 2011.

[93] A. A. Sagaidachnyi, D. A. Usanov, A. V. Skripal, and A. V Fomin, *Correlation of skin temperature and blood flow oscillations*, SPIE, 8337: 83370A1-83370A8, 2011.

[94] MTTC-1410, *Thermoelectric Coller Temperature Controller*, User's Manual, retrieved from: http://www.lairdtech.com, Melcor, last acceced: 3-12-2012.

[95] V. Vuksanovic, L. W. Sheppard, and A. Stefanovska, *Nonlinear relationship between level of blood flow and skin temperature for different dynamics of temperature change*, Biophys Jornal, 94: L78-L80, 2008.

[96] M. J. Geyer, Y. K. Jan, D. M. Brienza, and M. L Boninger, *Using wavelet analysis to characterize the thermoregulatory mechanisms of sacral skin blood flow*, Journal of Rehabilitation Research and Development, 41: 797-806, 2004.

[97] S. Podtaev, M. Morozov and P. Frick , *Wavelet−based Correlations of Skin Temperature and Blood Flow Oscillations*, Cardiovascular Engineering, 8: 185-189, 2008.

[98] R. C. Gonzalez, R. E. Woods and S. L. Eddins,*Digital Image Processing using MatLab*,Gatesmark Publishing, USA, 2009. 2003.

[99] W. Burger and M. J. Burge, *Digital Image Processing: An Algorithmic Introduction using Java*, Springer, New York, 2008.